High-*Q* Fused Silica Micro-Shell Resonators for Navigation-Grade MEMS Gyroscopes

by

Tal Rove Nagourney

A dissertation submitted in partial fulfillment
of the requirements for the degree of
Doctor of Philosophy
(Electrical Engineering)
in the University of Michigan
2018

Doctoral Committee:

Professor Khalil Najafi, Chair
Professor Luis Bernal
Assistant Research Scientist Jae Yoong Cho
Professor Parag Deotare
Professor Becky Peterson

Tal Rove Nagourney

taln@umich.edu

ORCID iD: 0000-0003-3141-0670

Dedication

    This work is dedicated to my family and friends. To my parents, Reena Liberman and Peter Nagourney, who have always encouraged critical thinking and open discussion. To my brother Micah Nagourney, with whom I always have enlightening discussions. To my grandfather, Murray Liberman, for his fascination with my research and the joy he took in hearing about it. To all my friends who have challenged and expanded my perspective. To Charlie Jordan and Jamie Leaf.

Acknowledgements

I am incredibly grateful to have studied under the guidance of Professor Khalil Najafi. He provided the perfect environment in which to learn and grow. He thoughtfully supported my research while allowing me to make my own mistakes and lead my own investigations. His emphasis on determination and the importance of effective communication has been indispensable and had a positive and meaningful impactful on my educational path.

It has been a privilege to have Dr. Jae Yoong Cho as my mentor and committee member. I greatly appreciate the years of effort he put into training me in all regards, including everything from fabrication to gyroscope theory to paper authorship. Thank you for reviewing all of my work, from my first paper to my dissertation.

Many thanks to my thesis committee, Dr. Jae Yoong Cho, Professor Becky Peterson, Professor Parag Deotare, and Professor Luis Bernal, for their feedback and guidance. Special thanks to Becky Peterson for her support when I first joined the Najafi Group.

Thank you to Robert Gordenker for being the backbone of the Najafi lab. Your resourcefulness and attention to detail saved me on countless occasions. You've taught me so much about proper research practices that I will carry forward. Thank you to Trasa Burkhardt for handling all of the organization and details that keep the gears turning. I've enjoyed so many conversations with Stacie Printon about life and its range of experiences. Thank you.

A huge thank you to my parents for supporting me throughout my education, especially my father, Peter Nagourney, for reviewing almost all of my written work. Thank you to my

Table of Contents

List of Tables

List of Figures

List of Symbols and Initialisms

α Coefficient of thermal expansion

$\Delta(1/\tau)$ Damping asymmetry, or damping mismatch: equal to the difference in damping of the two wine-glass resonant modes, i.e., $|1/\tau_1 - 1/\tau_2|$

Δf Difference in frequency between the two wine-glass modes, WG_1 and WG_2

δ Surface layer thickness

ε_r Permittivity of the capacitive gap volume

ε_0 Permittivity of the free space

γ Surface tension

λ Vibratory decay rate during exponential decay

μ Factor of order unity that depends on resonator shape, proportional to surface loss

π Pi, equal to ~3.142

$\phi_{surface}$ Surface loss angle, equal to $1/Q_{surface}$ at resonance

Ω Rotation rate about the z-axis of the sensor frame, z'

v Poisson's ratio

ρ Resistivity (Chapter 5, conductive films), material density (Chapter 6, TED)

σ_{rr} Surface stress in the radial direction

τ Ring-down decay time constant, equal to the time it takes for a resonator's vibrational amplitude to decay by a factor of e (~2.718)

τ_0 Initial measured value of the ring-down decay time constant

τ_1/τ_2 τ symmetry

τ_{ss} Time for the sense mode of a gyroscope in open loop rate mode to reach steady state

τ_{th} Thermal transport time constant

ω Natural angular frequency

θ_f Angle between the principle stiffness axis and the *x*-axis of the sensor frame

θ_{gyro} Angle of the resonator oscillation orientation relative to the sensor frame

θ_{input} Angle the sensor frame is rotated relative to the inertial frame

θ_τ Angle between the principle damping axis and the *x*-axis of the sensor frame

A Surface area of a capacitive plate

$A_{Coriolis}$ Coriolis acceleration: tangential acceleration acting on the resonator mass moving with radial velocity when the sensor frame is rotated, only exists in the sensor frame

A_g Angular gain: the ratio of the angle of oscillation orientation and the sensor frame

$A_{g_{eff}}$ Effective angular gain: the angular gain multiplied by resonant mode number, *n*

ARW   Angle random walk: angular error that builds up over time due to white noise in the angular rate measurement, given in $°/\sqrt{hr}$

B   Bias: offset in gyroscope measurement due to sensor imperfections and changes in environmental conditions, given in °/hr

BI   Bias instability: unpredictable variation in gyroscope bias, given in °/hr

b   Thickness of a beam or comb drive finger

BB   Birdbath: refers to the birdbath resonator structure (BB-R is used to denote the radius of the BB resonator in mm, e.g., BB-2.5)

BRG   Birdbath resonator gyroscope: MEMS gyroscope built with the birdbath resonator

$C(d)$ Capacitance as a function of parallel plate gap width

CMP   Chemical mechanical planarization, used to polish birdbath resonator rims

C_{SP} Specific heat capacity

CVG   Coriolis vibratory gyroscope

c_{x_0} Drive amplitude of the resonator in the force-to-rebalance rate mode

D Thermal diffusivity

d   Capacitive gap width for a parallel plate capacitor

d_0	Initial capacitive gap width for a parallel plate capacitor
D_{eff}	Effective bending rigidity of cantilever taking initial surface tension into account
DRG	Disk resonator gyroscope
d_s	Surface loss parameter
E	Young's modulus
E_1	Real-valued Young's modulus of the surface layer, also given as E_s
E_2^S	Dissipative Young's modulus of the surface layer
EI	Bending rigidity
e	Euler's number, equal to ~2.718
F	Force generated on a parallel plate capacitor
f	Frequency, typically resonant frequency
$F_{Coriolis}$	Coriolis force: tangential force acting on the resonator mass moving with radial velocity when the sensor frame is rotated, only exists in the sensor frame
$f_{n=2}$	Frequency of the $n = 2$ wine-glass mode
FS	Fused silica: a high-quality-factor ceramic used to produce the birdbath resonator
$f_{tilting}$	Frequency of the tilting vibrational mode
$f_{vertical}$	Frequency of the vertical vibrational mode
f_{WG}	Frequency of the wine-glass vibrational mode
f_x	Force applied to the drive mode of a gyroscope in the force-to-rebalance rate mode
f_y	Force applied to the sense mode of a gyroscope in the force-to-rebalance rate mode
$\lVert f_y \rVert$	Demodulated rebalance force applied to the sense mode of a gyroscope in the force-to-rebalance rate mode
g	Capacitive gap width between fingers of a comb drive
H	Height of a birdbath resonator
HRG	Hemispherical resonator gyroscope
k	Thermal conductivity

k_B Boltzmann's constant

l Length of overlap of comb drive fingers

l_{MFP} Mean free path length between air molecules at a given pressure

m Mass of the moving portion of a gyroscope

m_c Coriolis mass: the amount of the effective gyroscope mass that experiences Coriolis acceleration during rotation, which is a function of the mode shape

m_{eff} Effective mass: the portion of a gyroscope resonator's mass that has kinetic energy

MEMS   Microelectromechanical system(s)

n Normal vibrational mode number: equal to the number of standing half sine waves along the rim of a shell resonator in the wine-glass modes

S/V   Surface-to-volume ratio: surface area divided by volume of resonator structure

Q Overall mechanical quality factor: equal to the energy stored divided by the energy dissipated during each vibrational cycle

Q_0 Initial measured value of the overall quality factor

Q_s Quality factor of the sense mode

Q_{anchor} Quality factor limited by anchor loss, energy dissipated through the attachment point of a resonator

$Q_{intrinsic}$ Quality factor limited by intrinsic damping, energy dissipated in the bulk material

$Q_{fluidic}$ Quality factor limited by fluidic, or air damping

$Q_{surface}$ Quality factor limited by surface loss

Q_{TED} Quality factor limited by thermoelastic dissipation

R_{anchor} Radius of the anchor of a birdbath resonator

R_{outer} Radius of the outer rim of a birdbath resonator

RRW   Rate random walk: error in measured rate that accumulates with time due to white noise in angular acceleration, given in $°/\sqrt{hr}$

SF   Scale factor: the ratio of gyroscope output to input, typically in mV/°/s

T Temperature

T_0	Average temperature
t	Time
TED	Thermoelastic dissipation: energy dissipated in a material due to irreversible flow of heat from hotter to colder regions that arise due to flexion
TFG	Tuning fork gyroscope
T_{min}	Minimum thickness of a birdbath resonator, typically occurs near anchor transition
TP	Thermoplastic, used to protect birdbath resonators during lapping and polishing
T_{rim}	Rim thickness of a birdbath resonator
V	Voltage
$\vec{v}$	Velocity vector of the resonator mass in the $x'y'$ plane of the sensor frame
$V(t)$	Velocity of resonator rim as a function of time
V_0	Initial resonator rim velocity
w	Beam width
WA	Whole angle: mode of gyroscope operation where angle is read out directly
WG	Wine-glass: refers to the wine-glass modes of vibration (WG_1, WG_2 for each mode)
x	x-axis of the inertial frame that has a fixed orientation
x'	x-axis of the non-inertial sensor frame that moves within the inertial frame
x_{comb}	Distance a comb drive moves from its neutral position in the transverse mode
x_{drive}	Drive mode amplitude of a gyroscope in the open loop rate mode
y	y-axis of the inertial frame that has a fixed orientation
y'	y-axis of the non-inertial sensor frame that moves within the inertial frame
y_{sense}	Sense mode amplitude of a gyroscope in the open loop rate mode
z	z-axis of the inertial frame that has a fixed orientation
z'	z-axis of the non-inertial sensor frame that moves within the inertial frame

Abstract

This research aims to develop the resonator for a navigation-grade

microelectromechanical system (MEMS) Coriolis vibratory gyroscope (CVG) that will bring

inertial navigation capabilities to a wider range of applications by reducing gyroscope size and

cost. To achieve the desired gyroscope performance, the gyroscope resonator must have low

energy dissipation and a highly symmetric structure. Several challenges arise at the micro-scale

due to the increased sensitivity to imperfections and increased susceptibility to energy loss

mechanisms.

This work investigates the lower limit on energy dissipation in a micro-shell resonator

known as the birdbath (BB) resonator. The BB resonator is designed to mitigate the energy loss

mechanisms that commonly limit MEMS resonators, including anchor loss and thermoelastic

dissipation, through a unique shape and fabrication process and through the use of fused silica as

the structural material. A blowtorch molding process is used to form high aspect ratio fused silica

shells with a range of wall profiles, providing a high level of control in three dimensions that is

not possible with conventional micromachining techniques.

Prototype BB resonators were developed prior to this dissertation work but they achieved

low quality factors (Q) and low ring-down time constants (τ) on the order of 100 thousand and 1

s, respectively. The goal of this work is to drastically increase performance above these initial

results. Each relevant energy loss mechanism is considered in order to identify the dominant loss

mechanism for a given device. Process improvements are implemented to mitigate each loss

mechanism, including improved thermal management during blowtorch molding, cleaner lapping and polishing, reduced upfront surface contamination, and methods to remove contaminants after fabrication. Following optimization, Qs up to 10 million and τs up to 500 s are measured, representing a marked improvement over the prototype resonators. It is found that BB resonators are now limited by surface loss, as indicated by the observed inverse relationship between Q and surface-to-volume ratio.

The surface-loss-limited regime results in a high sensitivity to added surface layers. The addition of a conductive layer to enable electrostatic transduction is found to have a large impact, decreasing Q by 50% with the addition of only 30 Å of metal. It is suggested that the origin of this loss may be interfacial slippage due to a large increase in stress that occurs at the interface during oscillation. Experimental investigation into the dependence of Q on conductive layer composition, thickness, deposition conditions, and post-deposition treatments is carried out. Following treatments to removed adsorbed contaminants from the surface, resonators with a 15/50 Å Ti/Pt layer are found to maintain 60% of their initial Qs. Indium tin oxide (ITO) is identified as a promising conductive layer candidate, with initial experiments producing shells that maintain 70% of their initial Q.

The values of Q and τ produced in this work are unprecedented for MEMS resonators. Even accounting for the losses that accompany conductive layer deposition, birdbath resonator gyroscopes are expected to achieve navigation-grade performance.

Chapter 1

Introduction to Inertial Navigation

1.1 Motivation

For thousands of years humans have sought reliable methods of navigation. First we used the stars. Then we learned to measure Earth's magnetic field. In 1743, John Serson developed the first gyroscope-type tool for nautical navigation. It was a spinning top with a mirror-like surface that could help sailors maintain their orientation to the horizon [1]. In 1817 Johann Bohnenberger invented the spherical spinning mass gyroscope [2]. Then in 1852 Leon Foucault invented the modern spinning disk gyroscope [3]. These early devices were a novel demonstration of angular momentum, but not accurate enough to rely on for navigation. The design was refined in the early 1900s, enabling automatic ship and airplane stabilization [1].

The United States Department of Defense developed the modern satellite-based global positioning system (GPS) from 1978–1993 [4], which now enables accurate location of an object anywhere on earth with centimeter-level accuracy, provided there is an uninterrupted path to several reliable GPS satellites [5]. Many modern technologies including defense systems, air, sea, and land vehicles, and consumer electronics have come to rely on GPS for navigation, as it is accurate, inexpensive, and available around the world; however, in situations where the signal path is broken or interfered with, either intentionally or otherwise, GPS navigation fails. Furthermore, GPS is only useful below the satellite orbit and above the Earth surface, so other

techniques must be used for space or subterranean travel. These shortcomings beckon a supplementary method of navigation that is immune to external interference.
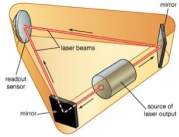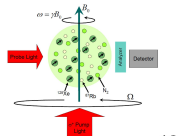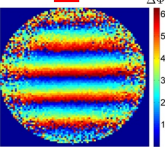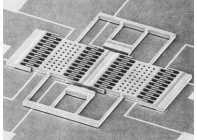
"Dead reckoning" is a method of navigating by estimating the direction and distance traveled that can be employed in GPS-denied environments to maintain accurate navigation. Dead reckoning can be achieved with an inertial measurement unit (IMU) consisting of x-, y-, and z-axis gyroscopes and accelerometers. These six degrees of freedom can be used to navigate without any external frame of reference as long as the initial position and orientation are known; however, the accuracy of this technique is limited by the drift of the sensors.

Microelectromechanical system (MEMS) IMUs are an attractive option, as they are small, lightweight, inexpensive, and consume little power, but these benefits are generally accompanied by increased noise and drift, limiting their usefulness for inertial navigation. The only IMUs that have been used for reliable, long-term navigation are large, heavy, and very expensive, limiting their usage to specialty applications. This research aims to bring dead reckoning to a wider range of applications by developing the resonator for a MEMS gyroscope with suitably low drift.

1.2 Types of Gyroscope

There are many different types of gyroscopes that measure rotation using different physical principles. Common designs include spinning mass, ring laser, fiber optic, nuclear magnetic resonance, atom interferometer, and Coriolis vibratory gyroscopes. High-performance versions of each design achieve performance suitable for dead reckoning navigation, but most are largely impractical due to their high complexity, size, and cost. Some of the best performance values reported for these designs are given in Table 1.1.

Table 1.1: Comparison of the best reported drift values, scale of cost, and approximate minimum size for common gyroscope designs. Sources for photos from top to bottom: [6], [7], [8], [9], [10], [11].

	Gyro Type	Bias Instability (°/hr)	ARW (°/√hr)	Cost Range	~ Size (mm)
	Spinning Mass	$\geq 3\times10^{-12}$ [12]	$\geq 9\times10^{-7}$ °/hr$^{3/2}$ [12]	Prohibitive	> 300
	Ring Laser and Fiber Optic	$\geq 1.5\times10^{-4}$ [13]	$\geq 5\times10^{-5}$ [14]	High	> 50
	Nuclear Magnetic Resonance	$\geq 10^{-2}$ [8]	$\geq 5\times10^{-4}$ [8]	High	> 50
	Atom Interferometry	$\geq 6.7\times10^{-5}$ [15]	$\geq 3\times10^{-6}$ [15]	High	> 500
	Macro Coriolis Vibratory	$\geq 1\times10^{-4}$ [10]	$\geq 2\times10^{-5}$ [10]	Medium–High	> 50
	MEMS Coriolis Vibratory	$\geq 10^{-2}$ [16]	$\geq 3\times10^{-3}$ [16]	Low	~1–10

1.2.1 Spinning Mass Gyroscope

The original type of spinning mass gyroscope is a disk that rotates with high angular velocity, suspended from a gimbal. It generates angular momentum that causes it to maintain its orientation in space as the outer gimbal fixture moves. The orientation of the spinning disk serves as an angle reference, for example to keep an airplane or ship level. Modern designs, such as that used in the Gravity Probe B (GP-B) gyroscope, read the orientation of a spinning superconducting sphere by electronically measuring the orientation of its the London magnetic moment. This method can be extremely precise, as the GP-B was designed to measure angle with

a drift rate of only $\sim 3 \times 10^{-8}$ degrees per year [12]. Despite their potentially high accuracy, this type of gyroscope is not suitable for many applications due to its large mass and potentially high cost.

1.2.2 Ring Laser and Fiber Optic Gyroscope

Ring laser gyroscopes (RLG) and fiber optic gyroscopes (FOG) both measure rotation rate using the Sagnac effect. A coherent light beam is split and sent in opposite directions around a loop, directed by mirrors for a RLG and by a fiber optic coil for a FOG. When the gyroscope is rotated, the path length of one beam becomes longer while that of the other beam becomes shorter, creating a phase difference between them. When they meet, they produce an interference pattern that contains the rotation rate information. These optical gyroscopes can be highly accurate but are typically very expensive. RLGs are also quite heavy, as they are typically constructed from a solid glass block and require 5–10 W of power at several hundred volts to power the laser.

1.2.3 Nuclear Magnetic Resonance Gyroscope

Nuclear magnetic resonance (NMR) gyroscopes determine rotation rate by measuring the change in Larmor precession frequency of a group of spin-polarized atoms in response to rotation [17]. Each atom effectively acts as a spinning mass gyroscope with a magnetic moment; this is essentially an atomic-scale application of the technique used in the GP-B. NMR gyroscopes have the potential to be scaled to small sizes; the physics package of a hermetically sealed NMR was recently demonstrated with a volume of 10 cc [17]. This is a difficult technology to shrink holistically though, as it requires a highly stable magnetic field and very accurate timing reference. Cost is still quite high and many challenges remain for commercialized compact NMR gyroscopes.

1.2.4 Atom Interferometer Gyroscope

There are several methods of using atom interferometry for rotation sensing. They take advantage of the fact that atoms, like light, have wave properties and that a beam of atoms can be split and recombined to produce interference patterns. Atom interferometers are potentially more sensitive than light interferometers, as the de Broglie wavelength is typically over four orders of magnitude smaller for atoms than for light. This generates a phase shift in response to rotation 10^{10} times larger for atom interferometers compared to light interferometers [18]. One challenge for atom interferometer gyroscopes is in distinguishing phase shifts caused by vibration of the platform from those caused by rotation. They also tend to be large and complex systems requiring precise alignment.

1.2.5 Coriolis Vibratory Gyroscope

Coriolis vibratory gyroscopes (CVG) measure rotation by detecting the effect of the Coriolis acceleration that acts on an oscillating mass when it undergoes rotation. The Coriolis force causes the oscillations to remain aligned to their initial orientation in space even as the sensor frame rotates. This causes the oscillation orientation to precess around the sensor frame, which can be measured through a variety of transduction mechanisms. This principle has been demonstrated successfully on both the macro and micro scale. The most successful macro-scale CVG is the hemispherical resonator gyroscope (HRG); it consists of a fused silica hemispherical shell whose flexural vibrations are read out and controlled electrostatically. It has low drift, high reliability, and can survive harsh conditions, but is too expensive for most applications and too large for some. Most MEMS gyroscopes are CVGs, but with a planar structure that oscillates in translational rather than flexural vibrational modes. Their performance continues to improve but is still orders of magnitude behind than that of the HRG, as shown in Table 1.1.

1.3 Navigation-Grade MEMS Gyroscope

MEMS IMUs are a promising avenue for reducing the size, weight, cost, and power required for dead reckoning. This research aims to develop a fused silica (FS) resonator, known as the birdbath resonator (BB), for a high-performance CVG known as the birdbath resonator gyroscope (BRG). Although many MEMS CVGs exist, they are mostly suitable for applications that can tolerate large amounts of drift such as mobile phones, video games, RC drones, and automobile stability control [19]. The drift requirements for dead reckoning are very high by comparison, as any angular rate error quickly accumulates and causes deviation from the intended path. The longer the integration time, the greater the deviation. Commercial MEMS CVGs have too much drift to accurately navigate for more than a few seconds. Gyroscopes with sufficiently low drift are too large or expensive for most applications. The BRG is designed to fill this gap, providing dead reckoning capability in a small, low-power package that can be affordably produced. Applications for the BRG include navigation for defense systems such as munitions, missiles, air, land, and sea vehicles, and people, and could ultimately be extended into the consumer domain.

Two key performance metrics when measuring angular rate with a CVG are angle random walk (ARW) and bias instability (BI). They are discussed further in Section 2.9. ARW refers to the buildup over time of angular error due to white noise in the angular rate measurement, given in $°/\sqrt{hr}$. It sets the lower bound on the angle a gyroscope can reliably measure over a given period of time. ARW is measured by integrating the rate output of a stationary gyroscope over time. Ideally this would be zero degrees, but in reality, white noise causes a non-zero rate and therefore a non-zero angle that increases with integration time. ARW is attributed to thermomechanical noise in the gyroscope resonator that is generated when energy

is dissipated. ARW is proportional to $1/\sqrt{Q}$, where Q is the mechanical quality factor, defined as the ratio of energy stored to energy dissipated during each resonant cycle [16]. Maximizing the Q will therefore reduce ARW.

Gyroscopes typically have some bias (B) in their output. If B is constant, it can be calibrated out. BI refers to the random variation in bias due to resonator imperfections, changes in environmental conditions, and $1/f$, or flicker noise. BI is given in °/hr [20]. It cannot be calibrated out and will therefore reduce measurement accuracy. It is commonly measured by averaging the rate output of a stationary gyroscope over varying lengths of time. As the averaging time increases, BI will typically decrease until it reaches a minimum, after which it will begin to increase again. This minimum is reported as the BI of the gyroscope. BI is a critical performance specification because it represents the noise floor for rate measurements. BI is proportional to the inverse of the ring-down decay time constant, τ, [16] and to the damping asymmetry of the degenerate vibratory modes [21]. τ is the time it takes for the velocity of a freely decaying resonator to reduce by a factor of e (~2.718) and damping equals the inverse of τ at the resonant frequency. Therefore, producing a resonator with the longest and most closely matched values of τ is critical.

Low ARW and BI are essential to producing a gyroscope for inertial navigation; however, achieving low damping asymmetry and high Q on the micro-scale is quite challenging, making it difficult to produce navigation-grade MEMS gyroscopes. As the size of a resonator scales down, it becomes more susceptible to certain energy loss mechanisms, especially fluidic damping and surface loss. Reaching the necessary levels of precision presents another barrier. Although microfabrication techniques are quite advanced, it is more difficult to achieve the same level of relative precision on the micro-scale compared to the macro-scale. Take for example the

spherical rotor of the Gravity Probe B satellite gyroscope. It was ground into a sphere from a solid cube of fused silica, then polished to a diameter of 3.7996 cm with sphericity better than 13 nm, or about 40 atomic layers [22]. Scaled up to the size of Earth, the tallest mountain and deepest ocean trench would be only ~2 m from sea level. To make a sphere with the same proportional imperfections on the micro-scale is not possible due to the finite size of atoms. Fortunately, this level of precision is not necessary for our desired performance goals. After all, the Gravity Probe B gyroscope is the most accurate gyroscope ever produced. The BRG is intended to achieve navigation-grade performance, typically defined as a BI of 0.01–0.1 °/hr [23] and an ARW of ≤ 0.002 °/$\sqrt{\text{hr}}$ [24]. These values are aggressive for a MEMS gyroscope due to the challenges in achieving low energy loss and high damping symmetry on the micro-scale.

The BB resonator has a 3D axisymmetric shape with a hollow central anchor stem. It is holistically designed to minimize energy dissipation from its ~10 kHz $n = 2$ wine-glass (WG) resonant modes and to prevent interference from environmental noise. The unique hemitoroidal shape of the BB resonator cannot be created with conventional microfabrication techniques, which are not well-suited for producing high aspect ratio fused silica structures. Instead, a novel blowtorch reflow molding technique, which was previously developed by Dr. Jae Yoong Cho, has been developed and optimized in this research to achieve unprecedented levels of micro-resonator performance [25]. It allows fused silica structures with a range of complex profile curvatures to be formed in a matter of seconds with a high degree of shape control. Due to the simultaneous definition of the entire structure, this process promotes a high degree of structural and damping symmetry that helps reduce BI and ARW.

1.4 Research Objectives

The focus of this research is to develop a high-performance FS resonator that will be suitable for operation as a navigation-grade MEMS CVG. The primary resonator characteristics that are used to estimate noise and drift performance once the resonator is packaged as a gyroscope are τ, Q, and damping asymmetry, $\Delta(1/\tau)$. τ and Q should be as high as possible, while $\Delta(1/\tau)$ should be as low as possible. The difference in frequency between the two degenerate WG modes, Δf, should be as low as possible, though this can be compensated with electrostatic tuning.

To drive and read out the FS BB resonator electrostatically, it must be coated with a conductive layer; however, the small size and high surface-to-volume (S/V) ratio of BB resonators makes them sensitive to their surface condition, and the addition of a conductive layer can adversely affect performance. It is therefore critical to optimize the conductive layer to minimize its negative effects. The effects of conductive layer material, thickness, and post-deposition treatments such as annealing are investigated.

To achieve these goals, experiments are carried out gain a comprehensive understanding of the dominant energy loss mechanisms that limit the τ and Q of BB resonators. This knowledge is applied to optimize the fabrication and testing process. The resulting resonators have very low energy dissipation and high symmetry about the longitudinal anchor axis, helping to lower bias instability. The results of this research are expected to enable the BRG to achieve navigation-grade performance, enabling dead reckoning in a small and affordable package.

1.5 Contributions

1.5.1 Energy Dissipation

Perform experimental investigation into the roles and mechanisms of energy dissipation that affect BB resonators. Gain an understanding of which form of dissipation is dominant for a given device depending on its geometric parameters, processing conditions, and defects. Use this knowledge to optimize fabrication, leading to unprecedented micro-shell resonator performance including the following BB resonators:

2.5-mm-radius, uncoated:
f = 9.16 kHz, τ = 204 s, Q = 5.87 million, Δf = 47.6 Hz, $\Delta(1/\tau)$ = 4.85×10^{-5} Hz

2.5-mm-radius, conductive layer:
f = 8.96 kHz, τ = 79 s, Q = 2.22 million, Δf = 22.0 Hz, $\Delta(1/\tau)$ = 3.64×10^{-4} Hz

5-mm-radius, uncoated:
f = 5.12 kHz, τ = 495 s, Q = 7.97 million, Δf = 5.7 Hz, $\Delta(1/\tau)$ = 2.20×10^{-6} Hz

5-mm-radius, uncoated:
f = 10.96 kHz, τ = 285 s, Q = 9.81 million, Δf = 10.3 Hz, $\Delta(1/\tau)$ = 1.62×10^{-4} Hz

5-mm-radius, conductive layer:
f = 5.10 kHz, τ = 224 s, Q = 3.60 million, Δf = 7.4 Hz, $\Delta(1/\tau)$ = 6.45×10^{-5} Hz

Once packaged as gyroscopes, all of these resonators are expected to achieve the navigation-grade BI and ARW goal.

1.5.2 Fabrication

Understand the dynamics of the blowtorch molding process that rapidly defines the final resonator structure. Design a mold that forms an optimized resonator through experiments and aided by finite element modeling. Relate the effect of molding, polishing, cleaning, annealing, and metallization process parameters to the performance of the resulting resonators.

1.5.3 Characterization

Identify proper methods of evaluating performance. Resonator performance can be altered by the packaging and testing process, so build an appropriate test setup and establish an effective testing procedure to ensure accurate measurements.

1.6 Organization of Thesis

This dissertation is divided into seven chapters. Chapter 1 summarizes the motivation and background for this research and states the research objectives. Chapter 2 provides background on Coriolis vibratory gyroscopes, including the physical principles of operation and the relevant noise sources. Chapter 3 discusses the architecture and control techniques of the BRG as well as the design, fabrication process, and fabrication challenges for the BB resonator. Chapter 4 presents the experimental results collected for BB resonators over the last four years. Chapter 5 discusses the experimental results for several different conductive layers. Chapter 6 covers all of the relevant energy loss mechanisms that affect BB resonators and discusses steps taken to mitigate them. Chapter 7 summarizes the work presented in this thesis and suggests directions for future work.

Chapter 2

Coriolis Vibratory Gyroscopes

Coriolis vibratory gyroscopes (CVG) measure rotation rate or angle by sensing the effect of rotation on an oscillating mass. The mass can take many forms, including a flat proof mass that moves coherently, a post that bends from side to side, or a disk, ring, or hemisphere that flexes about its center. Regardless of architecture, they all rely on the generation of Coriolis force in response to rotation of an oscillating mass.

2.1 The Foucault Pendulum

To understand the physical principles of a CVG, it is helpful to first consider the Foucault pendulum. Leon Foucault first used this large swinging pendulum in 1851 to illustrate the rotation of Earth. If we imagine placing a Foucault pendulum on the North pole and observing its oscillations from space, it would appear that Earth is spinning underneath the pendulum while it swings in a fixed orientation in the inertial reference frame of space (Figure 2.1(b)); however, observing from the non-inertial reference frame of Earth it would appear that Earth is stationary while the pendulum orientation is rotating, or precessing, at the same rate as the Earth rotates Figure 2.1(c). This is often demonstrated in science museums by standing twenty-four large dominos in a ring around the pendulum at the limit of its swing so that one is knocked over after each hour.
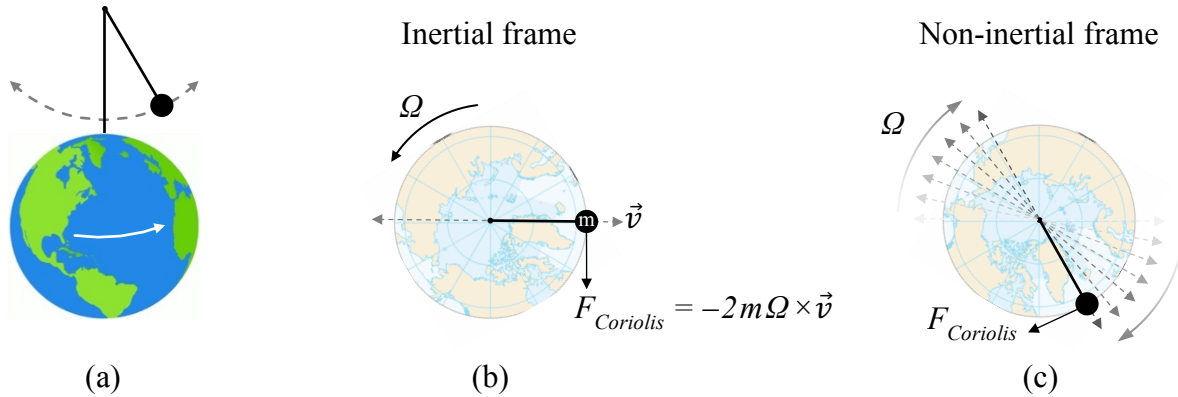
Figure 2.1: A Foucault pendulum placed on the North Pole of Earth (a). Viewed from above from the inertial frame of space, the pendulum appears to maintain its orientation as Earth rotates underneath it (b). Viewed from above but from the non-inertial frame of Earth, the angle of swing appears to precess at the Earth rotation rate while Earth remains stationary (c).

We can represent the pendulum with a point mass, m, that is constrained to oscillate in the $x'y'$ plane of the non-inertial frame, also referred to as the sensor frame, and experiences restoring force toward the origin by a set of springs, as depicted in Figure 2.2. Regardless of sensor frame rotation, the mass oscillation orientation will tend to stay aligned to its initial orientation in the xy inertial frame. Therefore, when the sensor frame is rotated, e.g., due to the rotation of Earth, the oscillation orientation appears to precess around the sensor frame as shown in Figure 2.1(c). This is explained by the application of Coriolis force perpendicular to the oscillation orientation that keeps it aligned to the inertial frame and accounts for the apparent precession around the sensor frame. The Coriolis force is referred to as a fictitious force because it does not appear in the inertial frame.

If the sensor and inertial frames are initially aligned, and the mass oscillates along both the x' and x axes, absent of any outside force or damping it will maintain its orientation indefinitely. We can call this mode 1, and state that all of the mass' energy is in mode 1. If the sensor frame is rotated, the mass will still oscillate along the inertial frame x axis, but in the sensor frame, the Coriolis force causes transfer of some of the vibrational energy to the y' axis, which we will call mode 2. The motion of the mass can now be described as a superposition of x'

and *y'* axis oscillations. If the rotation continues, eventually all of the energy will be contained in mode 2, and then will start to transfer back to mode 1. Since we know the mass oscillations are always oriented to the inertial frame *x* axis, we can use the precession angle within the sensor frame to calculate orientation to the inertial frame, θ_{input}. This is the basis for angular measurement with a CVG.
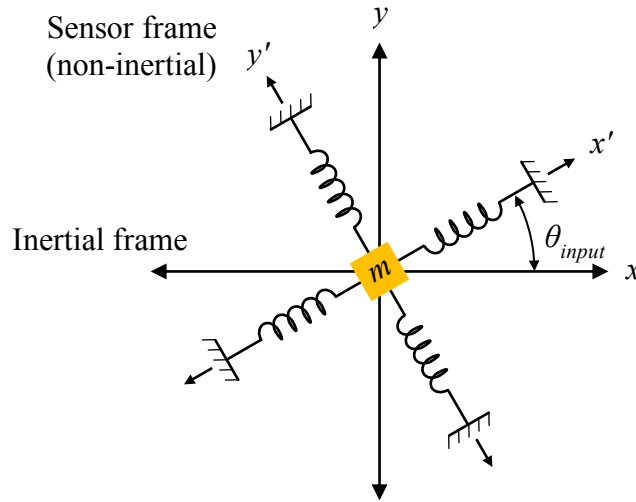
Figure 2.2: Representation of a Foucault pendulum as a two-dimensional harmonic oscillator. The pendulum mass, m, is suspended from springs along the sensor frame that provide restoring force towards the origin. The mass oscillations maintain their orientation to the inertial frame as the sensor frame rotates within the inertial frame.

The Coriolis acceleration is proportional to the linear velocity of the mass and the rotation rate of the sensor frame, given by

$$A_{Coriolis} = -2\Omega \times \vec{v} \qquad (2.1)$$

where $\vec{v}$ is the velocity vector of the mass in the reference frame, Ω is the rotation rate perpendicular to the reference frame, and $\times$ denotes the cross product. The Coriolis force can be calculated by multiplying the Coriolis acceleration by the mass of the pendulum:

$$F_{Coriolis} = -2m\Omega \times \vec{v} \qquad (2.2)$$

The same principles apply to a MEMS CVG. The body of the gyroscope is the sensor frame, and mode 1 and 2 are the drive and sense modes. Instead of a swinging pendulum, a vibratory

14

gyroscope consists of a translational or flexural mode resonator that oscillates in the *x'y'* plane of the sensor frame. A CVG can measure the rotation of Earth and any other rotation applied to its *z'* axis.

2.2 Resonant Vibration Modes

Vibratory gyroscopes typically operate in either a translational or wine-glass (WG) resonant mode. In the translational mode (Figure 2.7), the entire resonator mass moves coherently in both the drive and sense vibrational modes, as is the case for the Foucault pendulum. This has the advantage of maximizing Coriolis force generation; however, care must be taken to prevent interference from environmental noise, as an external shock or acceleration that excites sense-axis motion could appear similar to a genuine rotation signal. For this reason, multiple masses moving out of phase are typically used, as discussed in Section 2.4.1.

The WG modes are degenerate flexural modes of order *n* that can be excited in a circular structure. For the *n* = 2 mode, opposite sides of the resonator located at 0° and 180° move simultaneously toward, then away from each other, while the opposing sides located at 90° and 270° move simultaneously away, then toward each other. A second *n* = 2 WG mode exists 45° away from the first; the nodes of WG_1 are the anti-nodes of WG_2, and vice versa. These two modes can serve as the drive and sense modes for a CVG. The higher frequency *n* = 3 mode undergoes similar motion, but for three equally spaced regions rather than two. Its second mode is located 30° away. These mode shapes are illustrated in Figure 2.3. Higher order modes exist, but the *n* = 2 or 3 modes are typically used. This is discussed in Section 2.6.
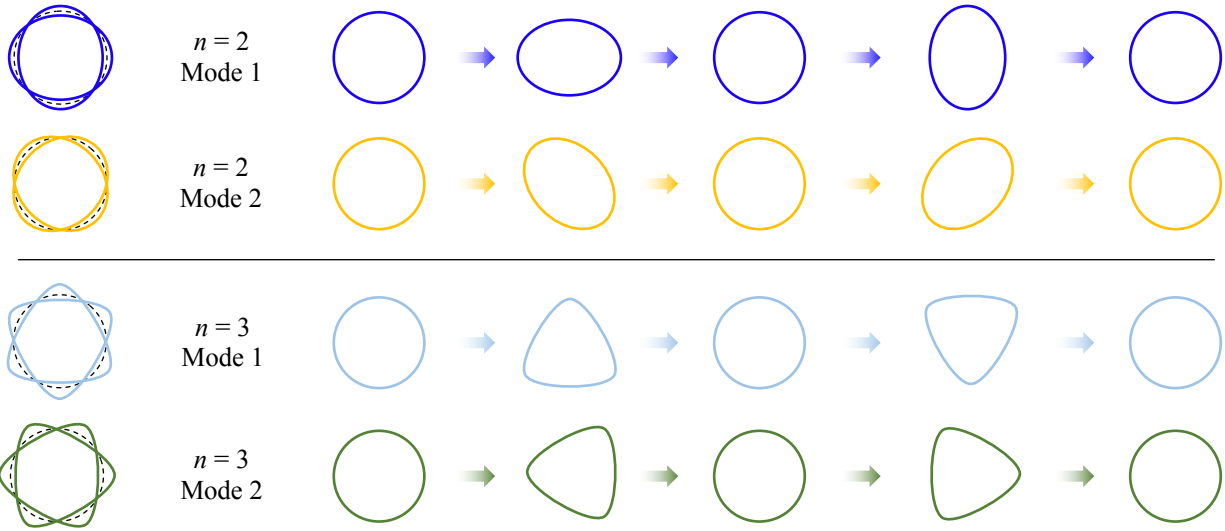
Figure 2.3: Illustration of the n = 2 (top) and n = 3 (bottom) mode shapes showing the sequence of deformations the perimeter undergoes during each oscillation period.

The WG modes enable differentiation between rotational and linear motion, which is required to ensure accurate readout. When a gyroscope is rotated, energy is transferred from the drive mode to the sense mode due to Coriolis force exerted tangentially on the portion of the mass with radial velocity (Figure 2.4). A resonator vibrating in a WG mode that is stationary or undergoing rotation will always deform with point reflection symmetry about the center of the anchor, but deformation due to linear acceleration causes the entire mass to shift in the direction opposite to the acceleration vector. Therefore, capacitance changes measured by opposing electrodes that arise from rotation will be in phase with each other, while those arising from acceleration will be out of phase, thus enabling acceleration signals to be filtered out through differential amplification.

Another advantage of the WG modes is their low anchor loss. Because the WG modes have point reflection symmetry about their center, the center of mass remains constant. Therefore, the center of the anchor does not move and does not transfer energy to the substrate.

16

This helps maintain a high Q, which helps to reduce measurement drift. The importance of high Q is discussed in Section 2.9; details on anchor loss are given in Section 6.4.
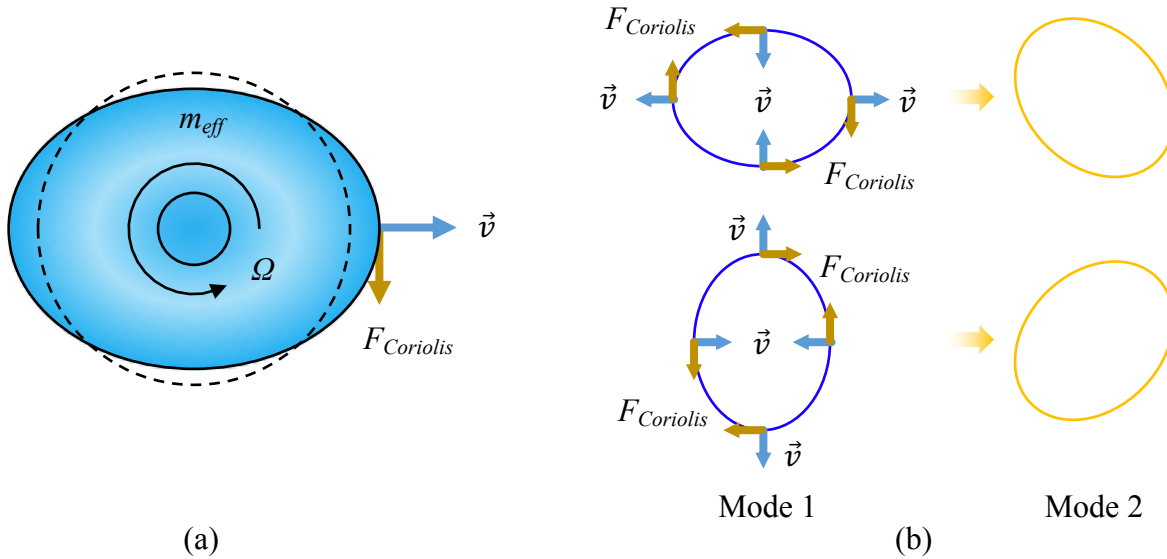
Figure 2.4: Depiction of the effect of Coriolis force on birdbath resonator in an $n = 2$ WG mode (a). During rotation, the portion of the shell's mass that has radial velocity is subjected to a Coriolis force that transfers energy between WG modes. The two flexion patterns of mode 1 correspond to two flexion patterns in mode 2, oriented 45° CW from mode 1 during CCW rotation.

Measurement drift can also be reduced by maximizing τ (see Section 2.9). Assuming Q remains relatively constant for a given resonant mode even as its frequency shifts, operating at a resonant frequency that is as low as possible will increase τ, considering

$$Q = \pi \tau f \tag{2.3}$$

where Q is the quality factor, τ is the vibratory decay time constant (the time for the vibrational amplitude to decay by $1/e$ from some initial value), and f is the resonant frequency. While maximizing τ helps reduce measurement drift, it is also necessary to stay above environmental noise frequencies to avoid their interference. The 2.5-mm-radius BB resonator (BB-2.5) is designed to place the $n = 2$ WG modes around 10 kHz, which is a good compromise between long τ and low noise. The resonator geometry is designed to keep parasitic modes as far away as possible, namely the tilting and vertical modes whose frequencies are lower than the WG mode.

Finite element modeling (FEM) and experiment show that $f_{tilting}/f_{wineglass} \approx 0.3$ and $f_{vertical}/f_{wineglass} \approx 0.7$, which should provide sufficient isolation. Higher order wine-glass modes also satisfy these criteria, but they have lower τs due to their higher frequencies and have been experimentally found to have lower Qs as well. This is believed to be due to surface loss and is discussed in Section 6.6.

2.3 Transduction Mechanisms

There are a number of transduction mechanisms used in MEMS including electrostatic, piezoelectric, piezoresistive, electrothermal, and electromagnetic. A brief overview of these techniques is given here, but we will focus on electrostatic which is the technique used with the birdbath resonator gyroscope.

Piezoelectric materials are crystals that generate a voltage in response to applied mechanical stress and generate stress in response to applied voltage. They can generate thousands of volts with enough applied force. They can also apply a large stress, but typically only resulting in nanometer-scale displacement. Stacked piezoelectric layers can get into the μm range. One common implementation of piezoelectric transduction is a bulk acoustic wave (BAW) gyroscope. This is a block of piezoelectric material that is excited into resonant motion by a sinusoidal voltage applied to opposing sides. Rotation induces a Coriolis acceleration on the oscillating mass, which results in strain perpendicular to that of the drive mode that is detected by sense electrodes.

Piezoresistors change their resistance in response to applied stress. Motion of a resonator can be measured using piezoresistive readout, but they cannot be used for actuation, so their application is limited for gyroscopes.

Electrothermal transduction is primarily used for actuation, with occasional uses for sensing. Actuation is accomplished by taking advantage of a material's thermal expansion, sometimes using the interaction between two materials with different thermal expansion coefficients. Generally, current is passed through the material, causing Joule heating and therefore expansion of the material proportional to its coefficient of thermal expansion, α. This technique can be used to produce large displacements but is slow, consumes milliwatts of power, and generates a lot of heat, making it largely prohibitive for gyroscopes.

Electromagnetic and magnetic actuation can generate large forces over long distances using low voltages compared to electrostatic, but they typically require high current to generate the magnetic field. They also tend to require complex fabrication processes, including fabrication or assembly of inductive coils and magnetic materials. This technique generally does not lend itself to MEMS gyroscopes.

Most MEMS gyroscopes use electrostatic driving and sensing with either parallel plate capacitors, interdigitated fingers (capacitive comb drive), or a combination of both. The gyroscope architecture typically has multiple fixed electrodes and one or more moveable electrodes that are biased to some DC voltage to generate electrostatic force. To drive the resonator, a sinusoidal voltage is applied to the fixed electrode; this creates an oscillating attractive force on the moveable electrode, which is attached to the resonator mass in the case of a gyroscope. Driving at the resonant frequency amplifies the resonator's motion by its mechanical quality factor, Q. To sense displacement, the change in capacitance as the moveable electrode approaches the fixed electrode is measured by the readout circuitry. For the BRG, we measure the current induced in the fixed electrode with a transimpedance amplifier (TIA).
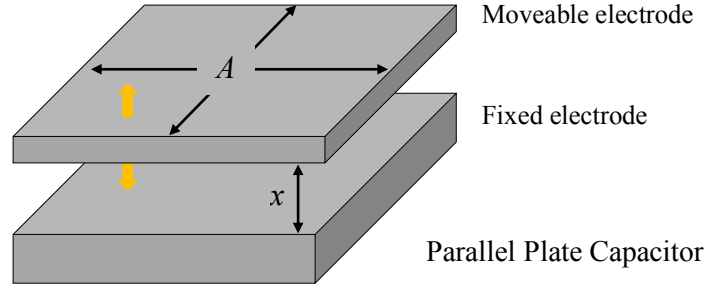
Figure 2.5: Diagram of a parallel plate capacitor. Application of a potential difference between the plates results in an attractive force that increases for a larger area (A) and smaller gap (d).

The capacitance for a parallel plate capacitor (Figure 2.5) is primarily due to the parallel electric field between the two plates. This is determined by the plate area (A), distance between the plates (d), the relative permittivity of the gap volume (ε_r), and the permittivity of free space (ε_0), as given by

$$C(d) = \epsilon_r \epsilon_0 \frac{A}{d} \qquad (2.4)$$

The force generated by applying a voltage, V, between the two plates is given by

$$F = -\frac{\epsilon_r \epsilon_0 A V^2}{2d^2} \qquad (2.5)$$

where the negative sign indicates that this is an attractive force between the plates. Parallel plate capacitors can apply a strong driving force, but care must be taken when designing their operating range. The presence of d^2 in the denominator means the force increases exponentially as the distance decreases, which results in the gap rapidly and uncontrollably closing if the plates are moved by more than $d_0/3$ under electrostatic force, where d_0 is the initial gap. This is called "pull-in." To maximize sensing resolution, the gap should be reduced to the minimum allowable size. If the same gap is used for both driving and sensing, the gap size and area must be optimized to achieve both the desired resonator displacement and measurement resolution. The BRG is driven and sensed by 16 vertical parallel plate capacitors that surround the wall near its outer rim. The shell itself has a conductive layer that acts as the movable electrode.

The electrostatic comb drive is commonly used in MEMS tuning fork gyroscopes. It consists of two opposing sets of interdigitated fingers and can operate in either a longitudinal or transverse mode. In the transverse mode, depicted in Figure 2.6(a), the fingers move towards and away from each other like parallel plate capacitors by some distance x_{comb}. Each finger of the moveable electrode sits between two fixed electrode fingers, forming one capacitor on the left and another one on the right. By applying a voltage to the left-side capacitors, the moveable electrode moves to the left, and the capacitances of the left and right side are

$$C_{left} = \frac{\epsilon\,(lb)}{g - x_{comb}}$$

(2.6)

$$C_{right} = \frac{\epsilon\,(lb)}{g + x_{comb}}$$

(2.7)

where $\varepsilon = \varepsilon_r\,\varepsilon_0$, l is the length of finger overlap, b is finger thickness, and g is the gap between fingers [26]. This technique has the same pull-in limitation as a typical parallel plate capacitor. When the moveable electrode moves side to side, the value of the left and right capacitors change inversely, and differential sensing is used to measure the displacement. The force-to-rebalance technique can be used to apply a voltage to the wider gap so the moveable electrode is pulled back to the neutral position, and the applied force can be equated to an acceleration.

In the longitudinal mode, the combs move so the fingers become more or less overlapped, as shown in Figure 2.6(b). In this case, the moveable comb is designed to stay centered within the fixed comb, but it still forms a left and right capacitor. Application of a bias voltage generates a force between the combs that causes them to become more overlapped. The total force along the y axis is

$$F_y^{total} = 2n \frac{\epsilon b V^2}{2g} = \frac{n \epsilon b V^2}{g}$$

(2.8)

where *n* is the number of moveable fingers [26]. The comb drive has the advantage of producing a constant force during actuation, making it stable over a large distance. It is important to consider that a force is also generated that pulls the moveable comb to the side, but this is theoretically equal on both sides and therefore cancels out. Due to imperfections in the fabrication process, however, there will be some transverse force that will eventually result in transverse pull-in if the applied voltage is too high.

(a) Transverse comb drive   (b) Longitudinal comb drive
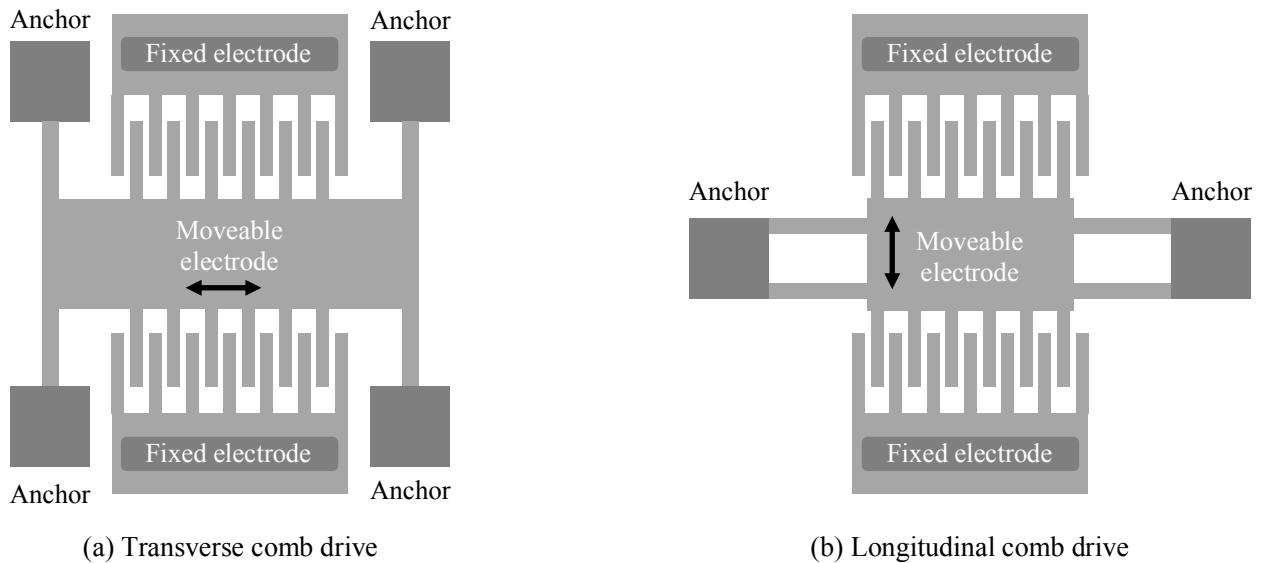
Figure 2.6: For a transverse comb drive (a) the fingers move side to side like parallel plate capacitors. For a longitudinal comb drive (b) the fingers toward and away lengthwise, varying their overlap and therefore capacitance.

Electrostatic actuation has several advantages for MEMS gyroscopes. It is very fast, especially compared to electrothermal, allowing application across a wide range of frequencies. It involves charging the capacitor plates but generally not passing current, so the power is very low and primarily consists of that used by the circuitry. When an AC signal is applied, a small amount of current is induced in the electrodes proportional to the rate of change of the voltage [26] that can cause minor resistive losses. Finally, it enables stiffness tuning. By selectively applying a bias to a particular region of a resonator, the stiffness is effectively reduced in that area. This phenomenon is known as electrostatic spring softening, and it can be used to match the

frequencies of two degenerate resonant modes whose frequencies are slightly mismatched due to fabrication imperfections. These advantages make electrostatic transduction an excellent choice for the BRG and other MEMS gyroscopes. The remaining discussion assumes the use of electrostatic drive and sense transduction.

2.4 Gyroscope Architectures

A number of different vibratory gyroscope architectures have been explored. Some rely translational motion of a proof mass, such as the tuning fork gyroscope, while others rely on flexion, such as the ring, disk, or hemispherical resonator gyroscopes. All of them utilize Coriolis force generation to transfer energy between two vibrational modes in order to measure rotation.

2.4.1 Tuning Fork Gyroscope

The tuning fork gyroscope (TFG) is the classic type of silicon MEMS gyroscope. An early monolithic silicon design was reported by Draper Labs in 1991 [27]. TFGs can be fabricated with bulk micromachining and scaled from the mm to μm size range, making them suitable for mass production. A single-mass design is susceptible to interference from acceleration signals, as translation along the sense axis due to linear acceleration of the gyroscope is difficult to distinguish from that due to Coriolis acceleration. It also tends to have high anchor loss and therefore low Q. It is better to have two or four masses driven out of phase so that anchor loss is reduced and differential amplification can be used to filter false signals. The basic TFG architecture is a flat rectangular proof mass suspended from two or four cantilevers with electrostatic drive and sense, as shown in Figure 2.8. The Draper Labs TFGs in Figure 2.8 are driven into resonance along the x' axis with longitudinal comb drives, while the z' axis displacement resulting from rotation about the y' axis is sensed by parallel plate capacitors

under the proof masses. A TFG can use piezoelectric [28] or electromagnetic [29] transduction as well, though electrostatic is most common.

(a) (b)
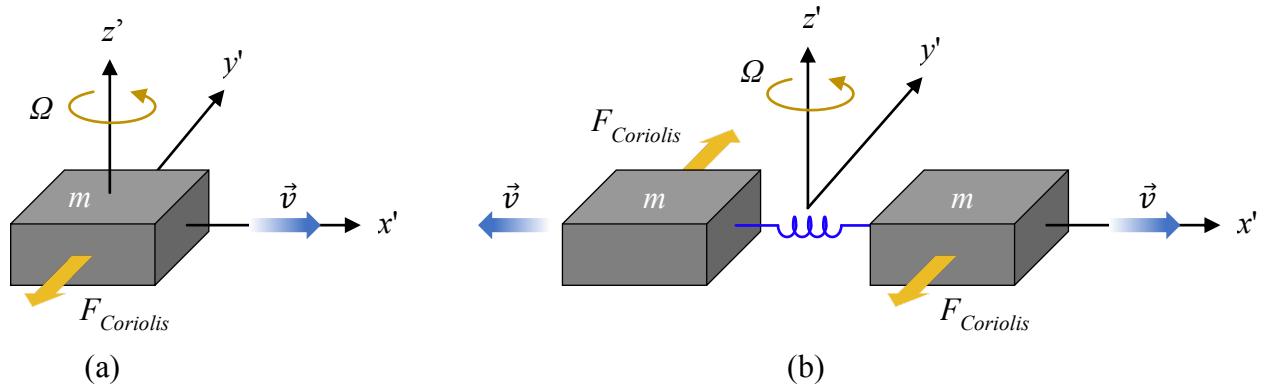
Figure 2.7: Tuning fork gyroscopes use a rigid proof mass that oscillates in the translational mode. Using two masses that oscillate in anti-phase (b) is preferable to a single mass (a), as it allows for differential cancellation of linear acceleration signals and greatly reduces anchor loss.
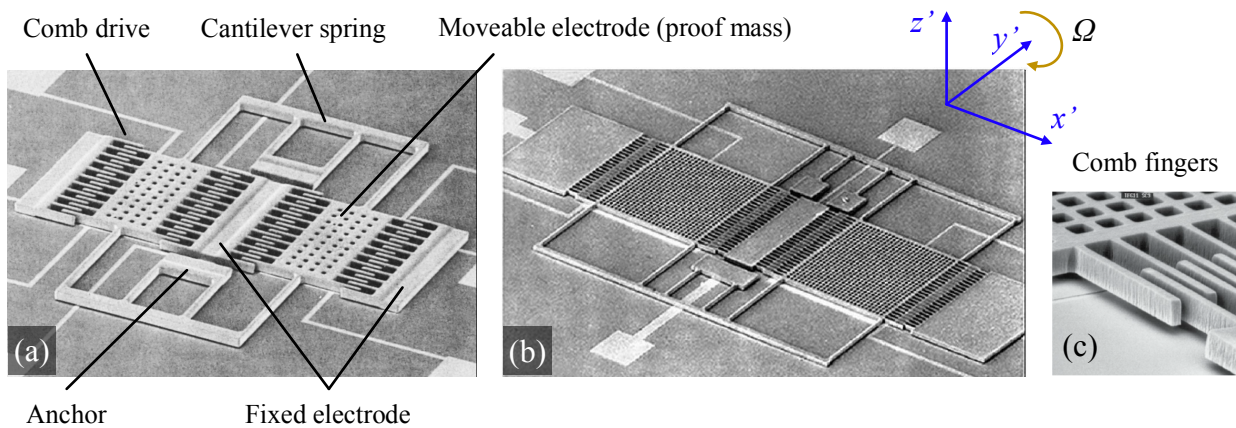
Figure 2.8: SEM micrographs of early MEMS tuning fork gyroscopes from Draper Labs. (a) An electroformed nickel gyroscope measuring 0.7 mm × 0.7 mm with relevant components labeled [11]. (b) A similar but larger TFG with the sensitive axis of rotation indicated [30]. (c) Comb drive fingers of the first silicon TFG [31].

2.4.2 Vibratory Ring Gyroscope

Vibratory ring gyroscopes use a circular ring of material as the resonator, suspended by tines to a point at the center of the ring [32]–[34]. They operate in the WG modes. They can be fabricated monolithically with concentric electrodes for drive and readout, with excellent control over the capacitive gap. Various structural materials have been used. The first MEMS gyroscope to operate in the wine-glass modes at a low frequency was the nickel ring gyroscope that was

first reported in 1994 [32]. That design was followed by similar polysilicon [33] and then single-crystal silicon [34] versions, but all ring gyroscopes suffer from having a small Coriolis mass and low sense capacitance [34] due to their low height.

(a) Nickel   (b) Polysilicon   (c) Single Crystal Silicon
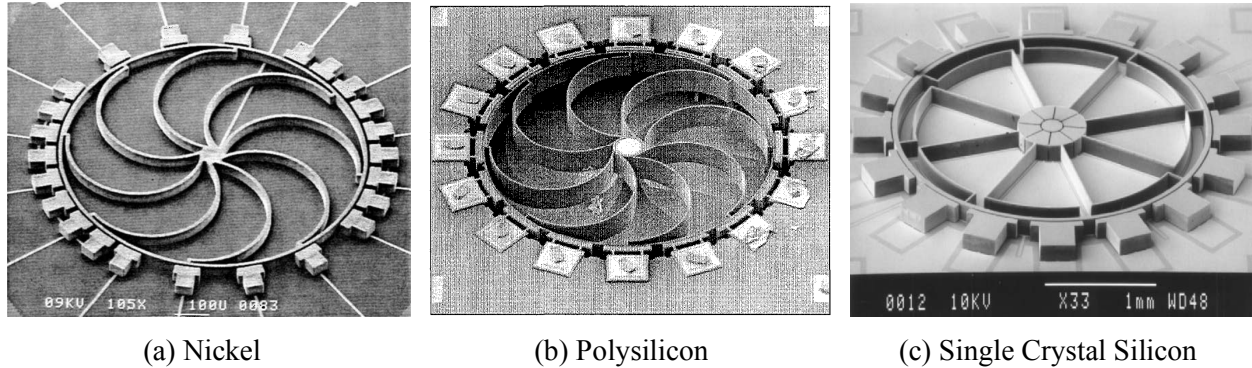
Figure 2.9: SEM micrographs of various University of Michigan ring gyroscope design. (1994) [32], (b) is fabricated by refilling DRIE trenches in silicon with LPCVD polysilic single crystal silicon that is machined with DRIE and bonded to a glass wafer (2002) [3

2.4.3 Disk Resonator Gyroscope

Disk resonator gyroscopes (DRG) are very similar to ring gyroscopes, except that they utilize a disk instead of a hollow ring. They have concentric electrodes for drive and sense are anchored to a hub in the center [16], [35] or to a concentric outer anchor [36]. Due to the increased rigidity of a disk, its WG mode frequencies will be much higher than that of a vibratory ring resonator. In many cases, the disk is designed with perforations to both lower its frequency and aid in chemically releasing the structure after fabrication. Some designs have shifted to more of a hybrid ring/disk design that consists of many concentric rings connected through alternating spokes to a central anchor point [16], [35]. This not only reduces stiffness, but adds many more locations for drive and sense electrodes, potentially improving readout capacitance. Still, their geometry is prone to low-frequency parasitic mode excitation because of their largely fixed aspect ratio.

25
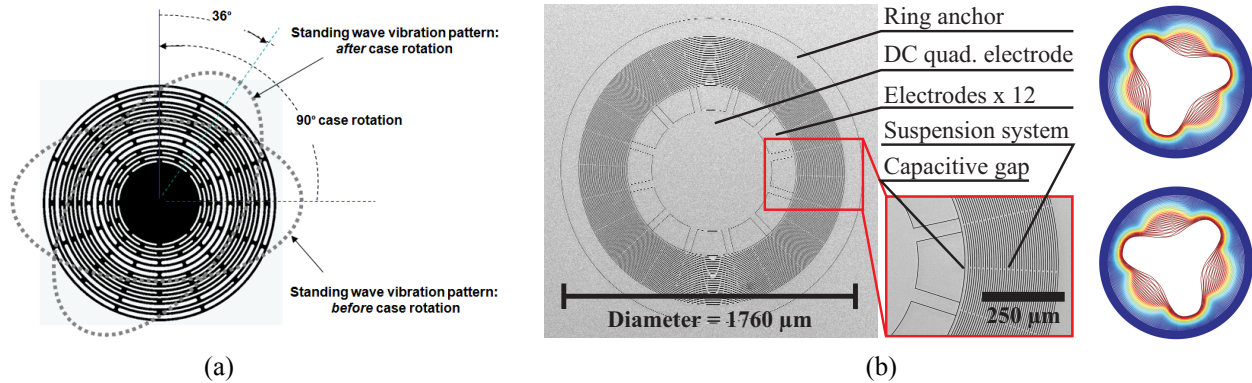
Figure 2.10: (a) The original DRG, designed by Boeing, which operates in the n = 2 WG modes [16]. *(b) DRG with an outer ring anchor designed for n = 3 WG mode operation from UC Irvine* [36].

2.4.4 Hemispherical Resonator Gyroscope

The hemispherical resonator gyroscope (HRG) has shown great promise in both the macro and micro scale. In essence, the hemispherical resonator is a vibratory ring resonator with a three-dimensional (3D) anchor. Instead of planar tines, a 3D shell gradually curves to a central anchor point or stem. This offers several advantages over 2D designs. It promotes uniform stiffness in all directions, while maintaining a low WG mode frequency that helps lengthen τ and therefore reduce bias instability (discussed further Section 2.9). The long distance between the rim and anchor helps to decouple the vibrational energy in the rim from the anchor, reducing anchor loss and further lengthening τ. A hemisphere also offers greater stiffness in the parasitic vertical and tilting resonant modes, increasing their frequencies and pushing them away from the WG mode frequencies. This reduces sensitivity to low-frequency environmental noise. Hemispherical resonators are usually transduced electrostatically or piezoelectrically.
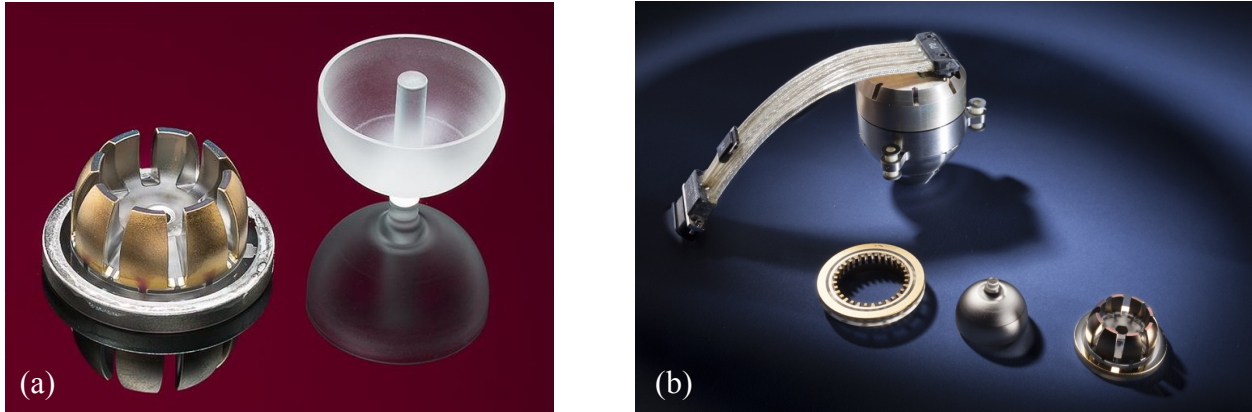
Figure 2.11: Two generations of macro-scale HRG. (a) The pickoff electrodes (left) for a 30-mm-diameter hemispherical resonator (right). [10]*. (b) CCW from top: package, forcer electrodes, metallized 56-mm-diameter resonator, and pickoff electrodes of an HRG* [37]*. Except for the package, each of these parts are machined from a solid piece of fused silica.*

The macro-scale hemispherical resonator gyroscope (HRG) has achieved great success. It consists of a fused silica hemispherical resonator with a solid stem, all abrasively machined from a single piece of fused silica. Its motion is driven and sensed electrostatically, and it is packaged in vacuum to ensure a high Q (discussed further in Section 6.2). Their performance is still unmatched amongst CVGs, with 2.5×10^{-4} °/$\sqrt{\text{hr}}$ angle random walk, 5×10^{-3} °/hr bias, and 1×10^{-3} °/hr bias instability over multiple days and a range of temperatures using a 30-mm-diameter resonator [38]. They boast over 30 million operating hours in space pointing applications with 100% mission success [38]. Their success is a major motivation behind the work in this thesis. Despite the HRG's excellent performance, its applications are limited due to its relatively large size (~25–56 mm diameter resonator), weight (0.7–1.4 kg packaged), power (~5 W), and its high cost. Recently, there has been considerable interest in scaling this type of design to a MEMS version. Some examples are shown in Figure 2.12. The resulting decrease in cost, size, weight, and power (CSWaP) could bring high performance gyroscopes to a much wider range of applications; however, it has proved difficult to fabricate 3D shell resonators on the micro scale. Microfabrication techniques enable excellent levels of control on two

dimensions, but struggle with high aspect ratios. Maintaining good symmetry and achieving low energy loss are key challenges that are addressed in this work.
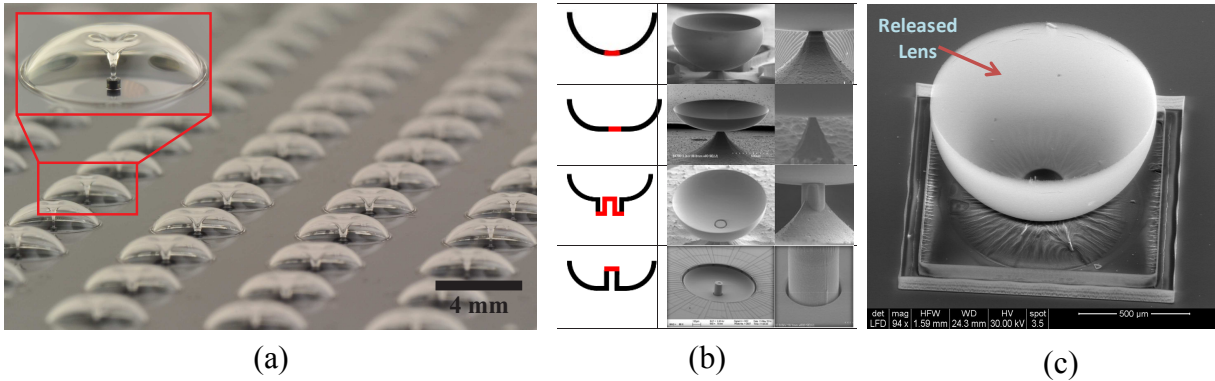
Figure 2.12: Examples of recent micro-shell resonators designed for MEMS gyroscopes. (a) UC Irvine's "inverted-wineglass" fused silica resonators, formed by expansion of trapped gas in a patterned cavity [39]. (b) Georgia Tech's micro shell resonator designs sought to reduce anchor loss [40]. (c) University of Utah's micro glass-shell resonator, fabricated with conformal deposition of glass onto a ball, then removal of the coating on the top half [41].

2.5 Control Techniques

The purpose of a gyroscope is to measure rotation; this can be accomplished in two ways. A rate mode gyroscope measures the rotation rate, which can be integrated to calculate the rotated angle. A rate-integrating, or whole-angle (WA) mode gyroscope directly measures the rotated angle. Any gyroscope can be operated in the rate-mode, but only some lend themselves to WA mode operation. For those that can do both, it is potentially beneficial to switch from rate to WA mode as rotation rate increases [42].

2.5.1 Whole Angle Mode

The Foucault pendulum is an example of a WA mode gyroscope. In this mode, the vibrations are allowed to precess freely around the gyroscope resonator, passing energy back and forth between its two resonant modes. The control loop maintains the vibrational amplitude, regardless of orientation. The change in precession angle is simply divided by the resonator's angular gain to calculate θ_{input}. This mode has a high dynamic range and is very effective for high

rotation rates. For a gyroscope to operate in the WA mode, its resonator should have uniform stiffness at all precession angles, otherwise additional processing is needed to compensate for the variation in response as the gyroscope rotates. Resonators with circular or cylindrical symmetry naturally lend themselves to this mode of operation, though a WA mode TFG has also been demonstrated [43].

2.5.2 Rate Mode – Open Loop

In the open loop rate mode, the drive mode is driven to some fixed vibrational amplitude. Under rotation, energy is transferred from the drive to the sense mode, increasing its amplitude. Assuming matched frequencies and damping for both modes, the ratio of drive (x_{drive}) and sense (y_{sense}) mode amplitudes is proportional to the rotation rate, and is given by

$$\frac{y_{sense}}{x_{drive}} = 2Q\frac{\Omega}{\omega} \tag{2.9}$$

where Q is the resonator quality factor and ω is its natural frequency [44]. The time (τ_{ss}) required for the sense mode to reach its steady state value is proportional to Q, as given by

$$\tau_{ss} = \frac{2Q}{\omega} \tag{2.10}$$

This relationship means there is a tradeoff between Q and gyroscope bandwidth. On the one hand, a high Q amplifies the motion in the sense mode, increasing the resolution of the gyroscope. On the other, a high Q reduces the gyroscope bandwidth by increasing the settling time. This tradeoff is unavoidable in the open loop rate mode operation.

2.5.3 Rate Mode – Force-to-Rebalance

As with the open loop rate mode, the drive mode is driven to some fixed amplitude in the force-to-rebalance mode. Under rotation, however, instead of allowing energy that transfers to the sense mode to build up until it reaches a steady state value, the sense mode electrodes are

used to null the sense mode vibrational amplitude by driving out-of-phase with the resonant motion. Instead of comparing their amplitudes, the forces applied to the drive (f_x) and sense (f_y) modes are compared. The relationship to rotation rate is otherwise the same [44]:

$$\frac{f_y}{f_x} = 2Q\frac{\Omega}{\omega} \tag{2.11}$$

The force-to-rebalance control technique enables the gyroscope to operate across a much higher bandwidth by eliminating the delay in reaching steady state. This allows for operation at frequencies approaching the resonant frequency of the resonator, though there is still a penalty for increasing the operating bandwidth in the form of a lower signal-to-noise ratio. This mode is generally best for slow rotation rates, as all the resonator interactions occur at a fixed location. Bias is an angle-dependent drift, so operating at a fixed location enables better bias compensation and therefore higher measurement accuracy [42].

2.6 Angular Gain

The more effectively energy is transferred between the drive and sense modes, the more sensitive a gyroscope is to rotation and therefore the finer its measurement resolution is. This is determined in part by the resonator structure and resonant mode shape, which affect the amount of the resonator mass that contributes to angular measurements. The effective mass, m_{eff}, refers to the portion of a resonator's mass that has kinetic energy, where the contribution to m_{eff} from a given point is proportional to its kinetic energy. The Coriolis mass, m_c, is the amount of m_{eff} that experiences Coriolis acceleration during rotation, which is also a function of the mode shape. Under z' axis rotation, only portions of the mass with $x'y'$ motion will contribute to m_c. The angular gain, A_g, refers to the portion of m_{eff} that contributes to the generation of the Coriolis force:

$$A_g = \frac{m_c}{n \, m_{eff}} \tag{2.12}$$

where n is the number of half sine waves in the normal mode oscillation pattern; the $n = 2$ mode is composed of two half waves, the $n = 3$ mode is composed of three half waves, etc. For the BB-2.5 resonator, m_{eff} is 1.27 mg in the $n = 2$ WG modes and 0.82 mg in the $n = 3$ modes, whereas the total resonator mass is ~4.5 mg. These values are calculated using FEM.

For a WA mode gyroscope, A_g is the ratio between the angle of the resonator vibrations relative to the sensor frame, θ_{gyro}, and the angle the gyroscope has been rotated, θ_{input}:

$$A_g = \frac{\theta_{gyro}}{\theta_{input}} \tag{2.13}$$

For an ideal TFG, Foucault pendulum, and any resonator operating in a translational mode, $n = 1$ and $m_c = m_{eff}$, so in theory, $A_g = 1$, which is the maximum. As a TFG undergoes rotation, the oscillation angle precesses between the two perpendicular vibrational modes at the same rate as the sensor frame rotates. In reality, due to non-idealities in the suspension, $A_g < 1$. For example, UC Irvine's quad mass TFG achieves $A_g = 0.86$ [45]. For resonators operating in the flexural WG modes, m_c will be some fraction of m_{eff} and n will be an integer greater than or equal to 2, making A_g less than 0.5 and meaning θ_{gyro} will lag considerably behind θ_{input}.

For a rate mode gyroscope, it is important to consider the locations of the maximum vibrational amplitude and the readout and control electrodes. For a translational resonator like that used in a TFG, the maximum displacement will be along the axis of translation, while for a WG mode resonator, the maximum displacement will be at the anti-nodes. For a TFG, the drive and sense modes are oriented to 0° and 90°, so the readout and control electrodes are aligned along the same axes. The TFG has an A_g of ~1, so when the sensor is rotated by 90°, most of the energy shifts from the drive mode at 0° to the sense mode at 90°. For a gyroscope operating in

the $n = 2$ WG modes, the anti-nodes of the drive mode are located 45° from the anti-nodes of the sense mode; the electrodes will be aligned to the anti-nodes of each mode to maximize resolution. For the $n = 3$ modes, the anti-nodes of the two modes are separated by 30°, as are the electrodes. The calculated A_g of a BB-2.5 resonator in the $n = 2$ WG modes is 0.25 to 0.3 for a 1.6 to 2-mm-tall shell, respectively. For the case where A_g is 0.3 for the $n = 2$ modes, A_g is 0.19 for the $n = 3$ modes. This means that when the gyroscope is rotated by 90°, the anti-nodes of the $n = 2$ mode would precess by 27.0° while the anti-nodes of the $n = 3$ mode would precess by 17.1°.

Although the actual precession angle is smaller for the $n = 3$ than the $n = 2$ mode, the $n = 3$ sense electrodes are located proportionally closer than the $n = 2$ electrodes. The values of angular gain should therefore be normalized to the mode number, n. We can define the effective angular gain, $A_{g_{eff}}$, as

$$A_{g_{eff}} = A_g \cdot n \tag{2.14}$$

This gives $A_{g_{eff}}$ of 0.6 for the $n = 2$ modes and 0.57 for the $n = 3$ modes. Therefore, for rate mode operation, the $n = 2$ and $n = 3$ modes are actually similar. The benefit of the $n = 2$ mode is that its lower frequency enables a larger drive amplitude, which improves resolution, scale factor, and angle random walk. The $n = 2$ mode is also preferable for WA mode operation, where the angle is directly read out from the precession angle. For these reasons, the BRG is operated in the $n = 2$ WG modes.

2.7 Scale Factor

The scale factor (SF) refers to the ratio of gyroscope output to input. The input for a rate mode gyroscope is a rotation rate, typically in °/s, while the input for a WA mode gyroscope is a

rotation angle, typically in °. The output for a rate mode gyroscope is the voltage required to generate the rebalance force, typically in mV, while the output for a WA mode gyroscope is the precession angle, typically in °. The units of SF are therefore mV/°/s for a rate mode gyroscope, while the SF of a WA mode gyroscope is given by A_g. SF is typically calculated as the slope of the straight line fitted by the method of least squares [46] after measuring the gyroscope output across a range of input rotation rates.

2.8 Resolution

Resolution refers to the minimum change in input that produces a reliably measurable change in output, i.e., the smallest signal a gyroscope can measure. For a gyroscope, the input will be either a rotation rate or angle that produces a change in output equal to a specified proportion of the output predicted by the SF, typically at least 50% [46]. Resolution is determined by the noise floor, as signals below the noise floor cannot be reliably measured.

2.9 Sources of Drift

The output signal of every gyroscope contains some undesired information, known as drift, that is not dependent on the input rotation. MEMS gyroscopes so far have had too much drift to enable reliable dead reckoning navigation. To reduce this drift to an acceptable level it is necessary to examine its sources. For a CVG, there are both systematic and random drift components. Systematic components include bias and environmentally sensitive drift rate. Bias, also known as zero rate output, is the averaged stationary gyroscope output for a specified time and operating conditions given in °/hr. The environmentally sensitive drift rate is drift due to the components of a gyroscope system that are sensitive to physical parameters including acceleration, vibration, and temperature [19]. Random drift components include angle random walk (ARW), rate random walk (RRW), and bias instability (BI) [19].

Environmentally sensitive drift should be addressed in the gyroscope architecture design. For example, the use of a resonator that deforms with point reflection symmetry allows for differential cancellation of acceleration and vibration signals. Active control can also be used to electrostatically center the resonator during a prolonged acceleration event [47]. Temperature sensitivity can be reduced through the selection of materials with low coefficients of thermal expansion and frequency. Using a design with a single central anchor also minimizes sensitivity to the effects of temperature-induced package stress. Temperature-induced drift can be almost completely eliminated with package ovenization, where resistive heaters are used to maintain a constant elevated temperature during operation. This enhanced temperature stability can enable operation across a wide range of temperatures, but at the cost of considerably higher power consumption.

A common technique for characterizing random drift components is to apply the Allan variance method to a long sequence of data collected from a stationary gyroscope. The output is averaged over different lengths of time, τ_{Allan}, and interpreted as a corresponding angular rate, $\sigma(\tau_{Allan})$, in °/hr. Different noise sources tend to be dominant during different sampling times, as shown in the typical Allan variance plot in Figure 2.13.

RRW is the error in measured rate that accumulates with time due to white noise in angular acceleration, given in $°/\sqrt{hr}$ or as a noise density with respect to bandwidth as $°/hr/\sqrt{Hz}$. Its origin in uncertain, but it shows up as a long-term low-frequency noise in the portion of the Allan variance plot with a $+\frac{1}{2}$ slope [20].
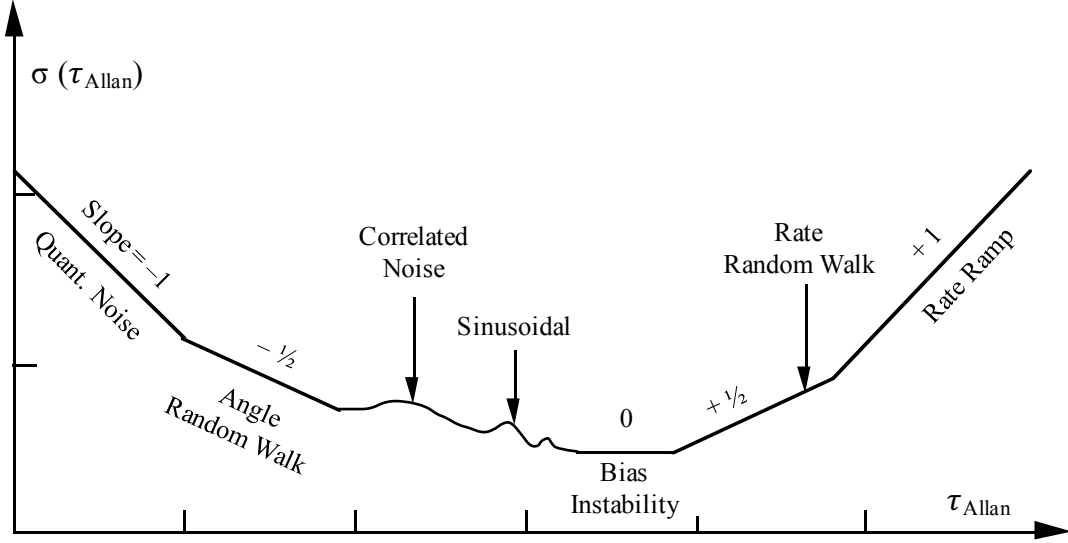
Figure 2.13: Typical log Allan variance plot of a gyroscope. The Allan variance ($\sigma(\tau_{Allan})$) is assumed to consist of several independent noise sources that are each typically dominant during different sampling times (τ_{Allan}). Plot from IEEE Standard 952 [20].

ARW is the time-dependent error in measured angle due to thermo-mechanical Brownian noise in the resonator [48]. It is given in $°/\sqrt{hr}$ or as a noise density with respect to bandwidth as $°/hr/\sqrt{Hz}$, and shows up on the Allan variance plot where the slope is $-\frac{1}{2}$. ARW due to the Brownian noise of a mechanical resonator is calculated as

$$\text{ARW} \left(°/s/\sqrt{Hz}\right) = \frac{1}{n\,A_g\,c_{x_0}} \sqrt{\frac{k_B T}{m_{eff}\,Q_s\,2\pi f}} \tag{2.15}$$

where n is the mode number, A_g is angular gain, c_{x_0} is drive amplitude, k_B is Boltzmann's constant in J/K, T is temperature in K, m_{eff} is effective mass, Q_s is quality factor of the sense mode, and f is resonant frequency [16], [49]. Inserting the values for a 10 kHz BB-2.5 resonator in the $n = 2$ WG modes, A_g of 0.3, m_{eff} of 1.27 mg, and assuming c_{x_0} of 1 µm, and T of 300 K, a Q of 0.45 million is required to reach navigation-grade ARW of $2\times10^{-3}\ °/\sqrt{hr}$. From a thermomechanical Brownian noise perspective, this should be easily achievable, as BB resonators regularly achieve Qs above 1 million.

ARW is measured by integrating the rate output of a stationary gyroscope over time to calculate angle. The output would be zero for an ideal device, but the Brownian noise in the rate measurement accumulates with integration time, resulting in a time-dependent angle drift. It can be calculated using either the power spectral density (PSD), Fast Fourier Transform (FFT), or bandwidth (BW) and standard deviation of the signal (σ) [50]:

$$\text{ARW}\left(°/\sqrt{\text{hr}}\right) = \frac{1}{60}\sqrt{\text{PSD}\left[\left(\frac{°}{\text{hr}}\right)^2/\text{Hz}\right]} \tag{2.16}$$

$$\text{ARW}\left(°/\sqrt{\text{hr}}\right) = \frac{1}{60}\text{FFT}\left[\left(\frac{°}{\text{hr}}\right)/\sqrt{\text{Hz}}\right] \tag{2.17}$$

$$\text{ARW}\left(°/\sqrt{\text{hr}}\right) = \frac{1}{60}\sigma\left(\frac{°}{\text{hr}}\right)\cdot\frac{1}{\sqrt{\text{BW(Hz)}}} \tag{2.18}$$

Brownian noise is random, so it is not possible to filter ARW out of the gyroscope readout. This sets a lower limit on the angle that can be reliably measured by a gyroscope, so it is desirable to minimize ARW. Since ARW in gyroscopes is proportional to $1/\sqrt{Q}$, maximizing Q will help improve resolution. Researchers investigating gravitational wave detection have faced a similar challenge with their interferometer mirrors. They concluded that fused silica and sapphire are the best candidates due in part to the their low internal loss and high mechanical quality factors that result in reduced thermal noise [51]. The BB resonator material selection and geometric design were made with this in mind, as discussed in Chapter 3.

BI is the unpredictable variation of B caused by imperfections and non-idealities in the gyroscope resonator and variations in environmental conditions. It is given in °/hr and is calculated by reading the lowest value on the Allan variance plot. BI is an important specification for gyroscopes, as it sets the lower limit on the measurable rotation rates; lower rates will be indistinguishable from noise. Several different grades of gyroscope exist for a range

of consumer and defense applications, generally categorized by their BI as consumer (30–1000 °/hr), industrial (1–30 °/hr), tactical (0.1–30 °/hr), navigation (0.01–0.1 °/hr), stellar-aided strategic (0.0003–0.01 °/hr), and strategic grade (0.00002–0.0003 °/hr [23], [52].

All of these noise sources must be considered when designing and operating a gyroscope, but ARW and BI are the primary considerations of this research, as they play a direct and important role in rate measurement. ARW is known to be related to $1/\sqrt{Q}$, and BI to damping asymmetry, $\Delta(1/\tau)$, and the ring-down time constants, τ_1 and τ_2 [16], [21], [53], [54]. For a closed loop force-to-rebalance CVG, B is calculated as

$$B = \frac{1}{nA_g} \Delta\left(\frac{1}{\tau}\right) \sin(2\theta_\tau) \tag{2.19}$$

$$\Delta\left(\frac{1}{\tau}\right) = \left|\frac{1}{\tau_1} - \frac{1}{\tau_2}\right| \tag{2.20}$$

where θ_τ is the azimuth of the τ_1 damping axis (the angle of the principle damping axis relative to the drive axis) [55]. A complete derivation is given in [55]. Longer and more closely matched values of τ will generally reduce B and BI; for example, when temperature or pressure changes, τ_1 and τ_2 may vary, causing fluctuations in bias. The longer τ is, the less variations in τ will affect B and BI.

For a perfect resonator, the WG modes are degenerate and damping of both modes is identical. In this case, the vibration pattern will precess freely around the shell without preference for orientation along one mode or the other. For an imperfect resonator, there is a difference in f and τ for each mode. This is described by the stiffness and damping axes, which are not typically aligned to each other [21]. This is depicted for the $n = 2$ WG modes in Figure 2.14. The difference between damping in the two resonant modes is a major source of B and BI in WG mode gyroscopes, as the vibrations will tend to drift toward the orientation with the least

damping, whereas ideally the mode orientation only changes in response to rotation [21]. Other sources of BI include noise in the readout and control circuitry and uncompensated temperature variations, but this work focuses on drift arising from the resonator.
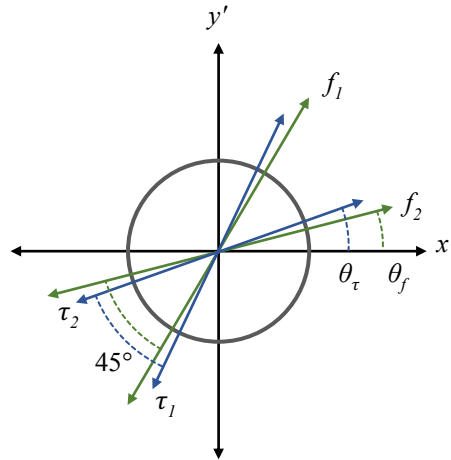
Figure 2.14: A non-ideal WG-mode resonator will have distinct stiffness and damping axes that are not typically aligned, as shown here for the n = 2 WG modes. The difference in damping between the two modes is a primary source of gyroscope drift.

A constant value of B can be calibrated out, but BI is unpredictable. Minimizing BI is therefore critical for producing an accurate gyroscope, as the resulting drift will be indistinguishable from the actual rate signal. Examining Equation 2.19, B is determined by n, A_g, $\Delta(1/\tau)$, and θ_τ. The angular gain is generally fixed by the resonator shape; the BB-2.5 resonator has a calculated A_g of 0.25–0.3 in the $n = 2$ WG mode. For the BRG, θ_τ is determined when the resonator is integrated with the electrode package. There is not currently a technique in place for identifying the principle damping axis orientation before assembly to ensure alignment, but the current design with 16 electrodes ensures θ_τ will never be more than 5.625°. $\Delta(1/\tau)$ is a critical aspect of B and BI, as it is a function of resonator symmetry that is controllable to some extent. Since it is not possible to fabricate a perfectly uniform resonator with $\Delta(1/\tau)$ equal to zero, we must take steps to minimize $\Delta(1/\tau)$. It is helpful to maximize τ_1 and τ_2, as a 10% difference between them is far less significant for $\tau = 1000$ s ($\Delta(1/\tau) = 1.11\times10^{-4}$ Hz) than $\tau = 10$ s

($\Delta(1/\tau) = 0.01$ Hz). A major focus of resonator development is to achieve the longest τ and lowest $\Delta(1/\tau)$ possible, while maximizing Q to help reduce ARW.

Chapter 3

Birdbath Resonator Design and Fabrication

3.1 Introduction
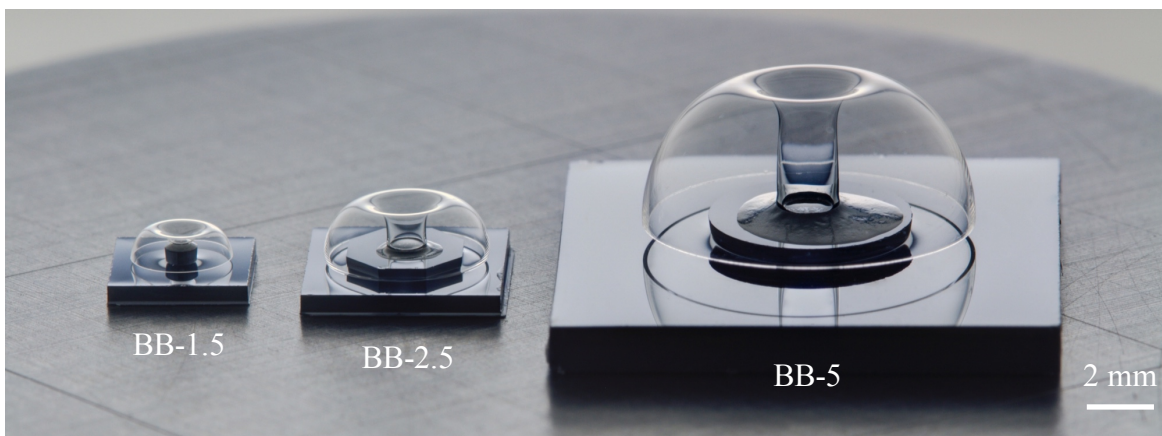
Figure 3.1: Three sizes of birdbath resonators have been tested, with radii of 1.5, 2.5, and 5 mm. They are shown here mounted to silicon substrates with glass frit. Larger resonators tend to achieve better performance.

The birdbath resonator gyroscope (BRG) consists of a fused silica (FS) birdbath (BB) resonator with a conductive surface, a concentric ring of silicon electrodes, and readout and control electronics. The final device will be vacuum packaged to reduce air damping. There are three main size generations of BB resonators, with outer radii of 1.5, 2.5, and 5 mm, as shown in Figure 3.1. These are referred to as the BB-1.5, BB-2.5, and BB-5, respectively. The BB-1.5 was initially investigated but had poor performance. The focus of this work is on the BB-2.5 and BB-5 resonators. To date, only BB-2.5 resonators have been packaged and operated as gyroscopes. Figure 3.2 shows a BRG (a), a BB-2.5 resonator (b), and a cross sectional depiction of a BB

resonator with relevant dimensional parameters labeled (c). Details of the dimensions are given in Table 3.1.
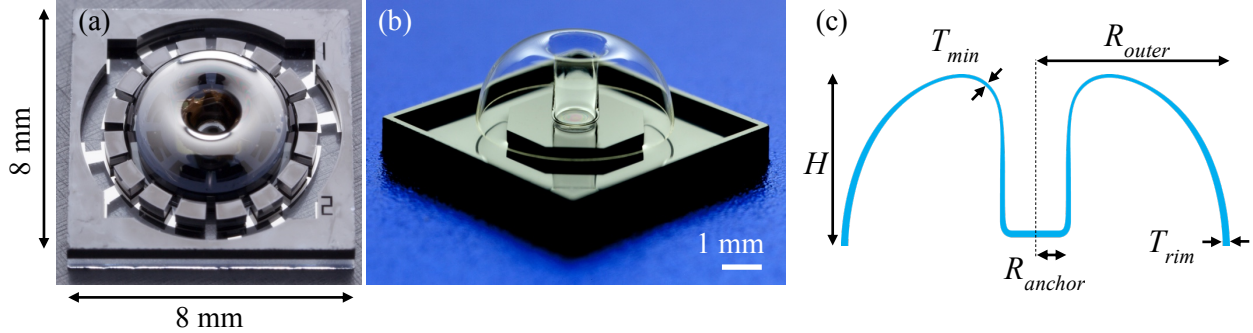
Figure 3.2: (a) Birdbath resonator gyroscope consisting of a classic BB resonator with a sputtered platinum layer and a concentric ring of 16 silicon electrodes for drive and sense. (b) BB resonator resting on a silicon substrate. (c) Dimension parameters of a birdbath resonator, shown on a cross sectional depiction.

Table 3.1: Relevant dimensions of the birdbath resonators discussed in this work, estimated with FEM. Definitions of the dimensional parameters are shown in Figure 3.2(c). (SA is surface area, S/V is the surface area-to-volume ratio.)

	$f_{n=2}$ (kHz)	R_{outer} (mm)	R_{anchor} (mm)	H (mm)	T_{rim} (µm)	T_{min} (µm)	SA (mm^2)	Volume (mm^3)	S/V (mm^{-1})	Mass (mg)
BB-1.5	10	1.5	0.3	0.8	30	7	26.0	0.2	105.5	0.5
BB-2.5	10	2.5	0.5	2.1	80	21	85.1	2.0	41.8	4.5
BB-5	5	5.0	0.75	4.6	150	30	362.9	17.2	20.6	38.8
BB-5	10	5.0	0.75	4.6	300	60	371.9	34.9	10.7	76.8

The BB resonator is designed to bring the performance of macro-scale fused silica hemispherical resonators to the micro scale. Fused silica is a highly desirable material, but it is difficult to work with using conventional microfabrication techniques, especially if high aspect ratios are desired. The blowtorch molding process enables high throughput and rapid prototyping of 3D shell resonators of a variety of shapes and sizes that are otherwise not possible (Section 3.3.5). It enables stiffness and thickness tuning in three dimensions to improve modal separation and energy isolation. Modal separation is difficult to control in vibratory ring resonators, but simulations show that the birdbath resonator achieves ~30% more separation than a 300-µm-tall ring resonator with the same 2.5 mm radius thanks to its 3D design [49]. This also allows for BB

resonators with thick rims that have a high Coriolis mass, while keeping the resonant frequency down at around 10 kHz to maintain a long τ. The design flexibility afforded by 3D reflow molding is a unique strength of the blowtorch molding process.

3.2 Birdbath Resonator Gyroscope Architecture

The BRG draws on some of the proven concepts used in larger gyroscopes such as the HRG. Since there are effectively no moving parts, once assembled and packaged there is no foreseeable limit to the lifetime of the gyroscope. Furthermore, it should be suitable for harsh environments, as its low resonator mass and the high strength of fused silica mean it can survive large shocks. There are many defense systems that would greatly benefit from a navigation-grade gyroscope in a small form factor, but there are civilian applications as well. Autonomous vehicles and drones rely on GPS for navigation but need inertial sensors to ride through periods when the signal is unavailable. The BRG could bring sensing performance, previously only possible in large and costly gyroscopes, to an affordable mm-scale system that can be widely employed.

This thesis is focused on the design and optimization of the BB resonator, but an overview of how it is implemented and operated as a gyroscope is given here. The key parts of the BRG are a BB resonator with a conductive coating and the silicon electrodes, as illustrated in Figure 3.4. The sixteen concentric electrodes are fabricated using a silicon-on-glass process, such that each electrode is electrically isolated and individually addressable by metal traces on the glass. The shell is attached to the glass substrate with a material that both anchors it and provides electrical connection to the conductive layer on the shell for biasing. Dr. Jae Yoong Cho developed a process to create conformal 3D electrodes with uniform ~7 μm gaps. The gaps are defined by a layer of sacrificial electroplated photoresist (EP) on the BB resonator (Figure

3.3(a)). The surrounding silicon electrodes are then grown to meet the sacrificial photoresist by

electroplating them with nickel (Figure 3.3(b–c)). The photoresist is dissolved to release the shell

and complete the process [...] lished in [56]. This

process enables the use o[...] all gaps. It also does

not contain any materials [...] n will ultimately be

sealed in a vacuum packa[...]

(a) (b) Coat EP on the   (c) Electroplate metal (d) Dissolve EP   (e)
     shell   from side electrodes

Figure 1. Fabrication process steps.
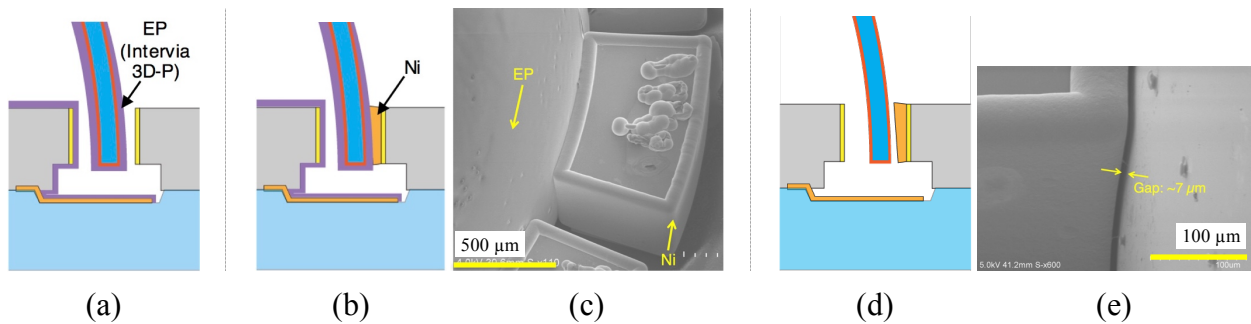
Figure 3.3: Creation of conformal 7 μm capacitive gaps for a BRG. (a) sacrificial electroplated photoresist (EP) deposited on BB resonator. (b) Nickel electroplating on silicon electrode conforms to sacrificial photoresist. (c) SEM micrograph of (b). (d) Remove electroplated photoresist, leaving conformal gap. (e) SEM micrograph of (d). Figures from [56]*.*

The BRG is depicted at rest and in the drive and sense modes in Figure 3.5. In the drive

mode, the shell resonates in the first $n = 2$ WG mode, oriented at 0°. Under rotation, energy is

transferred to the second WG mode, oriented 45° away from the first mode.
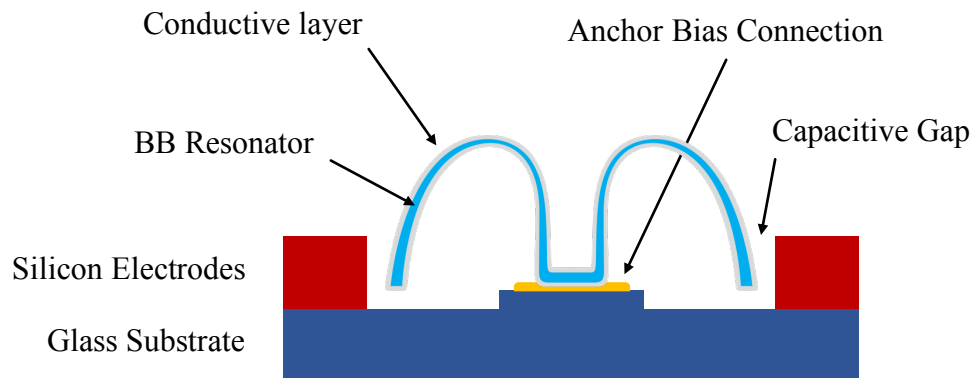
Figure 3.4: Cross sectional depiction of sides so it can be biased at its anchor co drive and sense the motion of the resona
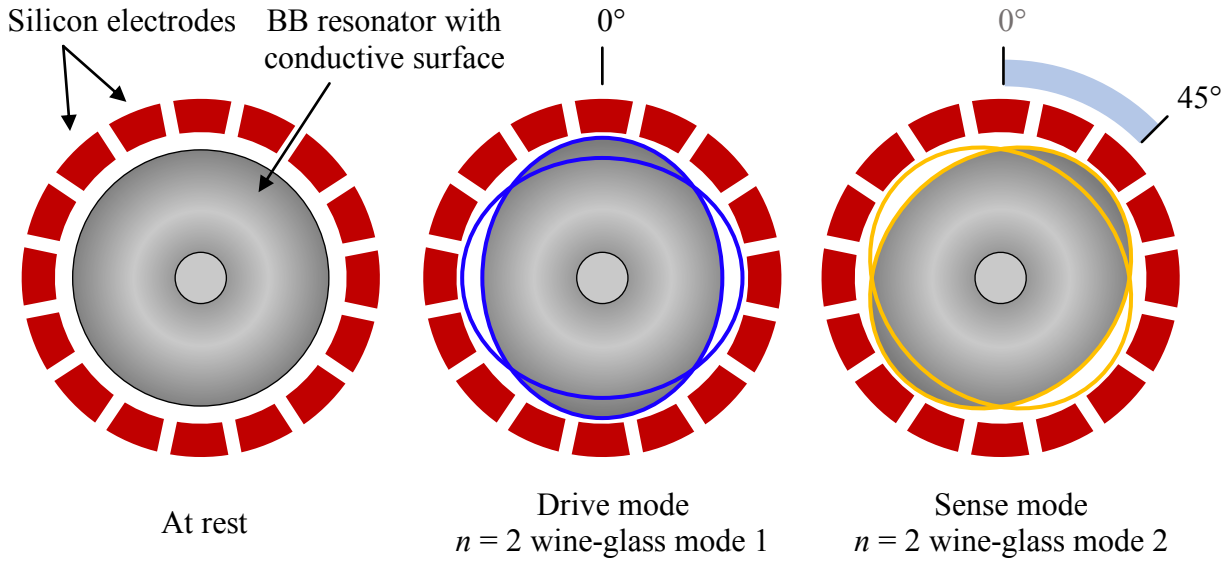
Figure 3.5: Schematic overhead view of the BRG. 16 concentric silicon electrodes drive and sense the resonator motion. In the drive mode, the shell resonates in the pattern shown in blue in the middle figure. In the sense mode, the shell resonates in the pattern shown in orange in the right figure; this resonant pattern is identical to the drive mode, but rotated by 45°.

A major advantage of electrostatic control is the ability to tune frequencies. For example, if the drive mode frequency is higher than the sense mode, we can lower its frequency by applying a DC voltage to a pair of opposing electrodes aligned with the drive mode's anti-nodes. This causes local electrostatic spring softening, effectively reducing the stiffness and lowering the resonant frequency of that mode. The same principle applies to the sense mode. The WG mode frequency split, Δf, is typically < 20 Hz, but with electrostatic tuning this can be reduced to a few mHz; this improves mode coupling and therefore gyroscope resolution. A detailed description of this process is presented in Chapter 6 of Dr. Michael Putty's thesis [44]. It is beneficial to minimize the capacitive gap so lower tuning and drive voltages are required, and to increase readout resolution.

For operation in the force-to-rebalance rate mode, the gyroscope is controlled with a field-programmable gate array (FPGA), as depicted in Figure 3.6. A phase lock loop (PLL) is used to maintain the drive mode frequency. The sense mode amplitude is measured and used to

calculate the rotation rate and to null the sense mode motion. The measured relationship between the drive and sense modes is fed into a quadrature loop that is used to generate DC voltages to null the quadrature of the resonator.
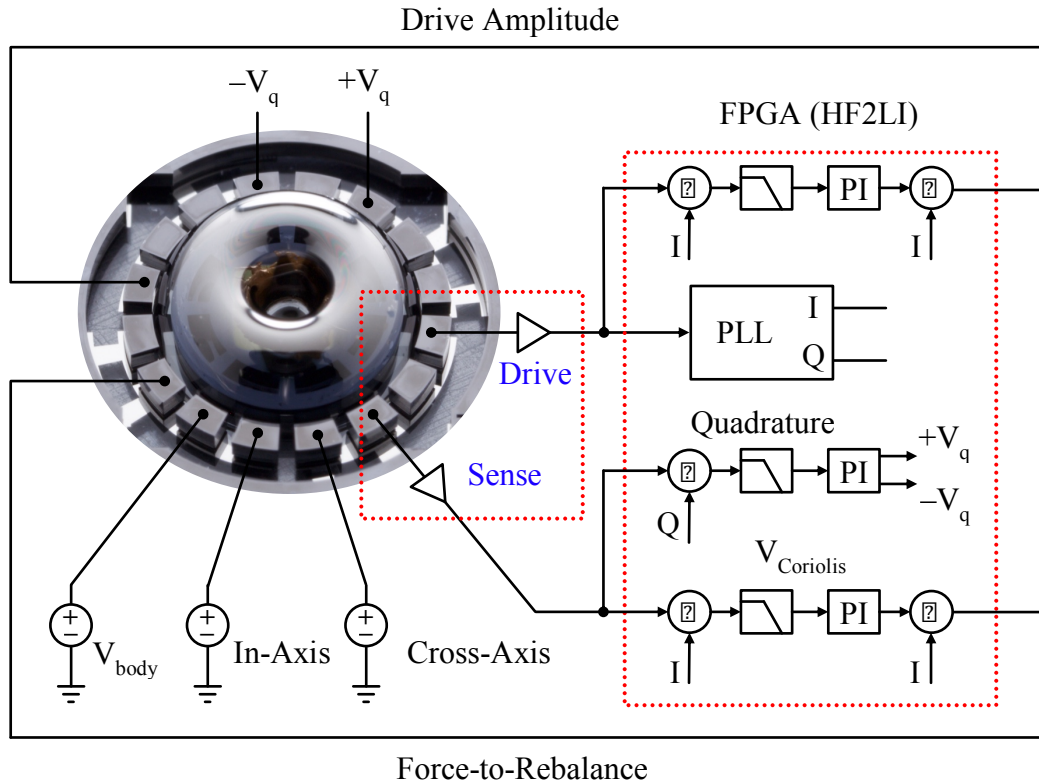
Figure 3.6: Schematic of the control architecture for operating the BRG in the force-to-rebalance rate mode. Control loops are implemented on an FPGA to lock to the resonant frequency, null the quadrature, and to cancel the sense mode motion. External power supplies are used to bias the shell and match the WG mode frequencies. Figure courtesy of Mr. Christopher Boyd.

Whole angle mode operation uses two PLLs to lock to the drive and sense mode frequencies, and to create quadrature reference signals. Demodulators are used to calculate the quadrature amplitudes so they can be nulled, as well as to calculate the in-phase signal amplitudes, which are proportional to the orientation of the wine-glass modes, θ_{gyro}. Calculating the mode precession angle and dividing by angular gain give a direct readout of the rotated angle, θ_{input}.
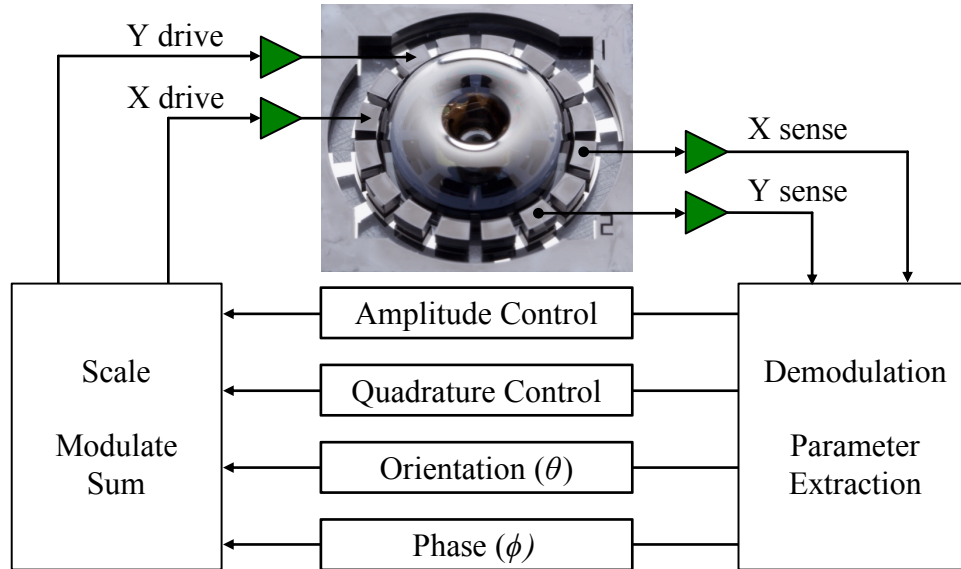
Figure 3.7: Schematic of control architecture for operating the BRG in the whole angle mode. A total of four electrodes are used to drive and sense the two WG modes. External power supplies are used to bias the shell and match the WG mode frequencies. Figure courtesy of Mr. Christopher Boyd.

3.3 Birdbath Resonator Fabrication

The BB resonator is fabricated by heating a fused silica substrate to its softening point and vacuum forming it into a graphite mold. An abrasive process is then used to separate the molded shell from the bulk material. This may be followed by metal deposition for electrostatic transduction. The basic process flow is shown in Figure 3.8, and will be shown and discussed in detail throughout Section 3.3. This process has been in development for several years and is now patented [57].

(a) Place FS substrate   (b) Blowtorch molding   (c) Lap away bulk FS   (d) Isolated shell
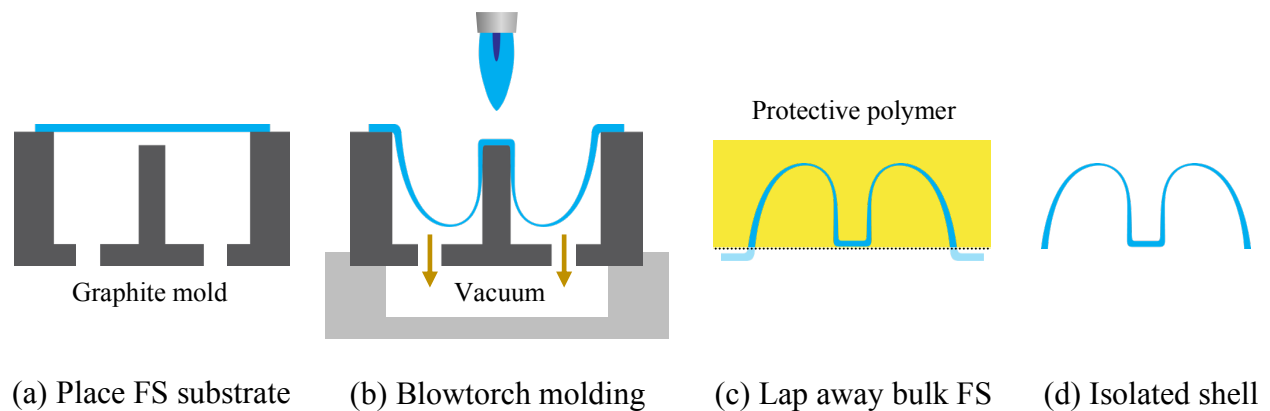
Figure 3.8: Overview of the blowtorch molding process depicting the key steps for fabrication a BB resonator.

46

3.3.1 Resonator Material Selection

Fused silica is chosen as the structural material of BB resonators for its advantageous material properties that produce an inherently high mechanical quality factor. In fact, it has the highest intrinsic Q at room temperature of any known glass, largely thanks to its extraordinarily low internal friction [58], a property that led to its selection as the test mass for interferometric gravitational wave detectors. One study on macro-scale FS resonators for such detectors yielded a Q of over 200 million [59]. FS has a low coefficient of thermal expansion (α) (0.56 ppm/K at 0–200 °C [60]) and low thermal conductivity (k) (1.30 W/m·K [60]) that contribute to low thermoelastic dissipation (TED) in the relevant ~10 kHz frequency range. This gives a considerable advantage over silicon resonators ($\alpha = 2.6$ and $k = 130$ W/m·K [61]), which are typically TED-limited at this frequency at room temperature [61], [62]. This is discussed further in Section 6.3.

Although it has many advantageous material properties for a high-Q resonator, FS is difficult to work with using conventional microfabrication techniques that have been developed primarily for silicon. They rely on etching bulk material and depositing thin films, processes that do not lend themselves to mm-scale structures with large height-to-radius ratios regardless of the material. To overcome this limitation, a thermal molding technique was developed by Dr. Jae Yoong Cho to reflow a FS substrate into a graphite mold [25]. This is discussed further in Section 3.3.5.

3.3.2 Substrate Preparation

Birdbath resonators are formed from bulk fused silica. The process begins with fused silica wafers with thicknesses ranging from 40 μm for the BB-1.5 to 100 μm for the BB-2.5 to 250–550 μm for the BB-5. To prepare them for molding, the wafers are diced to the desired

square dimensions using a resin-bond diamond dicing blade. The individual squares are then cleaned in solvents.

Generally, it is not possible to purchase commercially thinned wafers below 200 μm, as they become quite fragile and difficult to handle. To thin wafers from 200 to 100 μm, they are wet etched in 49% hydrofluoric acid (HF) with nitrogen bubble agitation, which evenly removes material from both sides at a rate of ~1 μm/min. To thin down to 40 μm, the wafers must first be mounted to a carrier wafer, as they are too thin to handle individually. They are bonded to a standard 500-μm-thick 4" silicon wafer using a thermoplastic, then etched in 49% HF from one side until they reach the desired thickness. The FS and carrier wafer are diced together. The squares are heated so the FS substrates can be slid off of the silicon, and finally they are cleaned in a solvent bath.

(a)	(b)	(c)	(d)
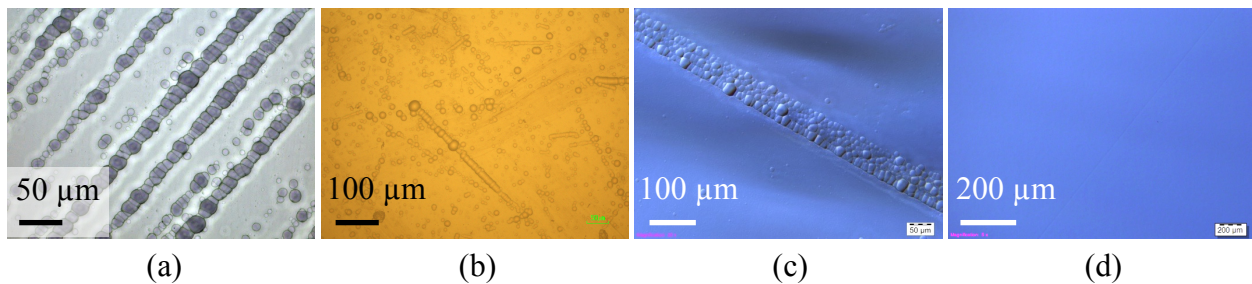
Figure 3.9: (a)–(c) are optical micrographs of typical defects seen in fused silica wafers after etching away 100 μm of bulk material from one side. (d) shows the smooth surface after etch defects have been removed with CMP. (c) and (d) are imaged with a polarizing filter to make defects appear more clearly.

Removing such a large amount of material in HF can cause the surface quality of the fused silica to become quite rough, depending on any defects that remain after the lapping process. Even though these wafers are polished to stringent scratch and dig specifications, even the slightest defect will be amplified during HF thinning. Examples of defects that emerge after etching are shown in Figure 3.9(a–c). If they are severe, they can be largely removed with

several minutes of chemical-mechanical planarization (CMP), as shown in Figure 3.9(d). Minor defects will smooth out when the FS reflows during molding.

3.3.3 Mold Material Selection

Graphite is chosen for the mold material for its high tolerance to extreme temperature fluctuations and its machinability. FS does not soften until ~1600 °C [60], and the molding process occurs in a matter of seconds. The mold must be able to handle repeated cycling from room temperature to >1600 °C and back down without deforming, cracking, or contaminating the fused silica. Furthermore, it must be machinable to a high degree of accuracy, as the molding process defines the final resonator geometry which is critical for accurate gyroscope operation. Few materials possess these properties; fortunately, graphite does and is a readily available and affordable option.

The behavior of fused silica during reflow is determined in part by the its temperature, which is dependent on the material properties of the mold. Figure 3.10 shows the simulated effect of mold thermal conductivity, k_{mold}, on BB resonator shape and thickness when the mold is treated as a heat sink. In all cases, the location of the thinnest region tends to correspond with the transition away from the anchor stem, as highlighted with red ovals. If thermal conductivity is too high, the thick region of the mold near the shell rim (black circles) dissipates so much heat that the shell locally hardens and cannot conform to the outer wall (Figure 3.10 (c)). Lower thermal conductivity increases molding conformality. Too little thermal conductivity may cause the shell to mold uncontrollably, quickly conforming to the entire mold geometry. The graphite chosen for making resonator molds has a thermal conductivity of 93 W/(m·K), which has proven to be a good balance.

(a)   (b)   (c)

| 13 | Thickness | 99 | | 13 | Thickness | 99 | | 8 | Thickness | 100 |
| | (μm) | | | | (μm) | | | | (μm) | |

$k_{mold} = 40$ W/(m·K) $k_{mold} = 70$ W/(m·K) $k_{mold} = 140$ W/(m·K)
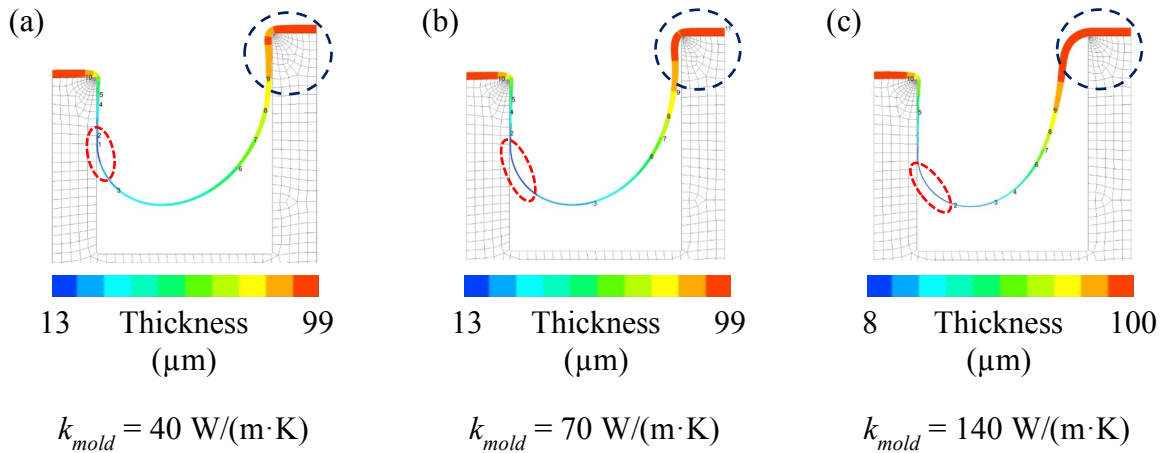
Figure 3.10: FEM of the effect of graphite mold thermal conductivity on shell shape and thickness for a BB-2.5 resonator with starting substrate thickness of 100 μm. Too much heat dissipation prevents the shell from conforming to the outer wall of the mold, as highlighted by the black circles.

3.3.4 Mold Design and Fabrication

A major advantage of the blowtorch molding process is that the graphite molds can be machined using a CNC mill. The higher the accuracy the better, but the results presented in this thesis are for molds machined in a conventional machine shop without any exotic equipment. This enables rapid and affordable prototyping of different resonator shapes and dimensions, especially compared to a multi-step lithography process.
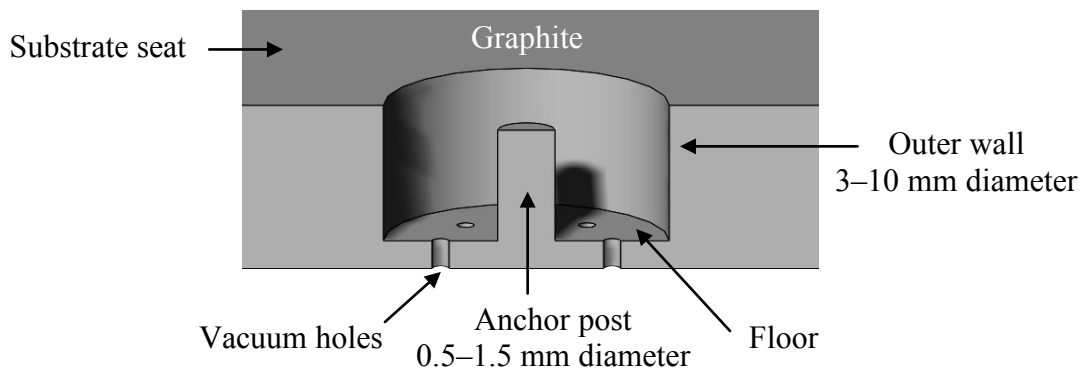
Figure 3.11: Cross sectional depiction of a basic BB resonator mold with important regions labeled.

The success of the blowtorch molding process is largely determined by the design of the mold structure; the size, angle, and spacing of the mold features directly translate to the final

resonator geometry. The basic features of a BB mold are shown in Figure 3.11. It is important to consider how the immense amount of heat imparted by the blowtorch will travel through the mold and into the underlying metal chuck. An effective design concentrates heat in regions where the shell must undergo the most extreme deformation, such as the anchor, and increases heat dissipation in regions where the FS should deform less. Designing for appropriate heat dissipation will also greatly increase the lifetime of a mold from less than five to over fifty reflow cycles.
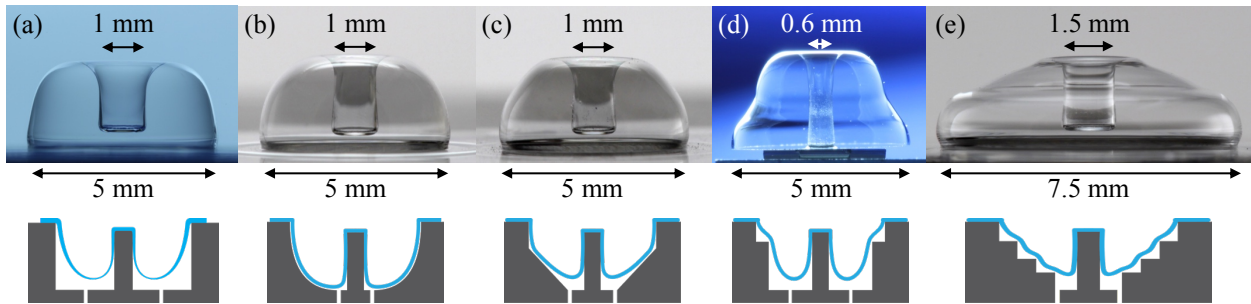
Figure 3.12: Several mold designs have been used, leading to a variety of shell profile curvatures. The mold designs depicted below produced the shells photographed above. The resonator designs shown are (a) Birdbath (classic), (b) Guided birdbath, (c) Cone, (d) Bell, and (e) Staircase.

Using a mold with vertical sidewalls has the advantage of minimizing physical contact with the FS during reflow, as depicted in Figure 3.8(b). This ensures the rough graphite texture is not transferred to the smooth FS surface and allows the shell to reflow freely into space, where surface tension helps smooth out any imperfections imparted at the point of contact with the mold's outer wall. The profile of the shell, however, is more or less limited to that shown in Figure 3.12(a) for a mold with straight and vertical sidewalls. By varying the mold sidewall profile, we can achieve excellent profile curvature control. Many different mold designs have been evaluated to explore the ability to control resonator shape [63]. All of them have a centered anchor post, but the anchor dimensions and sidewall profiles have been changed to alter the

corresponding features on the resonator. Several designs are shown in Figure 3.12. Figure 3.12(a) shows the classic BB mold design with straight sidewalls.

All micro-shell resonators have a high S/V ratio and are therefore sensitive to surface losses. A primary concern for using molds with complex profile curvature is increased surface losses if texture from the graphite mold transfers to the atomically smooth shell surface. Experiments with the guided, cone, bell, and staircase mold designs (Figure 3.12) have shown that we can control the profile curvature of the shells to a high degree by transferring the mold geometry, but surprisingly there is no evidence of the fused silica actually touching the graphite or taking on its texture. The shell surfaces are smooth in appearance, as evidenced by the SEM micrographs shown in Figure 3.13. Even when the reflowing FS encounters the sharp edge of a bell mold, rather than crease around the corner it gently curves. Atomic force microscopy scans confirm that the average surface roughness remains at 2.4 Å [63] in the region near the step, negligibly higher than the 1.8 Å measured for the BB design [64].

| (a) Guided | (a) Cone | (a) Bell | (a) Staircase |
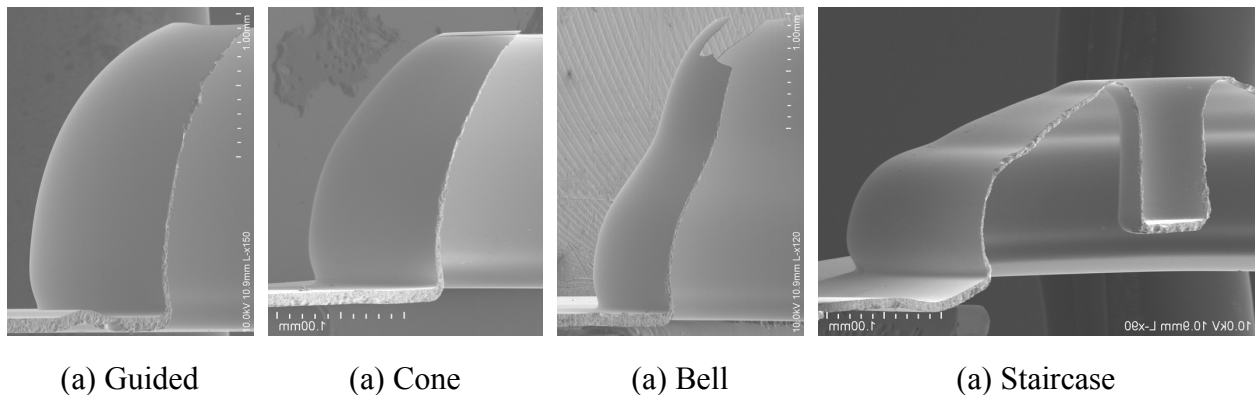
Figure 3.13: SEM micrographs of cross sections of shells with designed curvatures. The molds used to form these shells are shown in Figure 3.12. Except for the staircase design that used a thicker initial substrate, the anchors broke off the other shells during abrasive cross-sectioning.

To gain insight into this phenomenon, we turn to the well-established glass molding industry; however, there are some key differences between our method and theirs that must be kept in mind:

1. We do not want our shells to touch the mold

2. We use a thin substrate instead of a thick parison (molten mass of glass)

3. We use fused silica instead of soda lime glass

We achieve a very smooth surface and profile curvature by allowing the FS to sag between the outer edge and anchor; this would not be possible if it were pressed into a mold. There has been considerable investigation into the heat transfer between glass and mold and what may prevent them from contacting during the blowing process [7, 8]. The resulting research is instructive for our case as well.

For the case where the glass is hotter than the mold, as it is with our process, it was reported that glass temperature falls rapidly on initial contact with the mold and tends to remain constant even after several seconds of contact [66]. By the time it reaches a mold feature, our FS has stretched to less than 100 μm thick, so even the slightest contact with the mold likely dissipates enough heat to locally freeze the shell in place. Fused silica is also very viscous at the softening temperature of ~1600 °C; therefore, we suspect the shell very lightly touches the mold without receiving its texture, but enough to cool it below the softening point.

Conduction through air may also play a key role in profile control. In glass molding processes, there is a very thin gas layer between the glass and the mold, the temperature of which is considered to be the average between that of the mold and glass surfaces [66]. Since the graphite is cooler than the FS, the air layer between them may be below the softening temperature of the FS. As the FS approaches the graphite and the air layer approaches zero thickness, its thermal resistance decreases. Thermal conduction through the air layer may be sufficient to cause the shell to stiffen before it touches the mold.

For wineglass mode resonators, a high aspect ratio 3D structure may reduce anchor loss by isolating the anchor from the portion of the structure where most of the vibrational energy is stored. Figure 3.12(d) shows the bell resonator design, where a step is added to the mold sidewall profile. The bell resonator has an accentuated rim, created with the intention of storing an increased portion of the vibrational energy further from the anchor to reduce anchor loss. Ali Darvishian performed FEM with COMSOL Multiphysics to compare the TED-limited Q, Q_{TED}, and the anchor-loss-limited Q, Q_{anchor}, of the bell and birdbath resonators. His simulations indicate that the bell resonator achieves $1.42 \cdot Q_{anchor}$ of the birdbath resonator, but $0.44 \cdot Q_{TED}$. This aligns with our suspicion that the bell resonator achieves lower anchor loss due to a greater portion of the energy being stored in the widest portion of the rim, furthest from the anchor. The higher thermoelastic damping is due to stress caused by the complex profile curvature as shown in Figure 3.14. Despite promising simulations, experimental performance of the bell resonator was not as high as the classic BB-2.5. Simulated Q_{TED} and Q_{anchor} were much higher than experimental Q, so they are not likely the cause for this. Presumably the bell resonator's higher surface-to-volume (S/V) ratio increased surface loss. The various energy loss mechanisms are discussed in detail in Chapter 6.

Birdbath resonator   Bell resonator
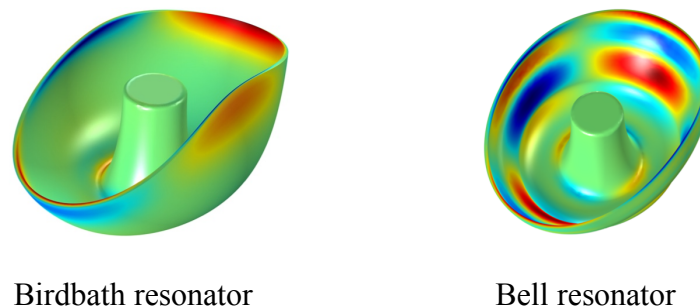
Figure 3.14: Comparison of hot and cold spots in birdbath and bell resonators that occur as a result of deformation. The curvature of the bell resonator is more complex and therefore results in greater thermoelastic dissipation.

The bell design was the first attempt to control shell profile with a modified mold sidewall. The staircase design (Figure 3.12 (e)) explored the limits of this principle with respect to sharp features, but was not tested as a functional resonator. The cone (Figure 3.12 (c)) and guided birdbath (GBB) (Figure 3.12 (b)) designs demonstrate the ability to shape the entire resonator structure by designing the mold sidewalls to be the negative of the desired resonator shape. There are many potential benefits of this technique, including better control over the location of parasitic mode frequencies and improving alignment of electrodes to the shell wall. Additionally, if an improved resonator shape is conceived using FEM, achieving a high level of shape control through mold design is necessary for testing the model experimentally.

Motivated by the ability to control shell profile, several variations on the classic BB design with different sidewall and anchor profiles were conceived. Dr. Behrouz Shiari performed finite element analysis (FEA) of their expected performance. The shapes and expected Q_{anchor}, Q_{TED}, and $f_{wineglass}$ of three designs—normalized to a classic BB-2.5—are presented in Figure 3.15. The Cylindrical (b) and Egg (c) shells are expected to have lower Q_{anchor} and Q_{TED} than the BB, so they have not been explored; however, the hemispherical shell is expected to have a 15% higher Q_{anchor} and 36% higher Q_{TED} than a classic BB while keeping the same frequency. The GBB mold of Figure 3.12 (b) was developed in hopes of confirming this simulation. Several designs of GBB resonators were fabricated, but the performance never reached that of the classic BB design, as shown in Figure 3.16. One explanation for this is that when the shell follows the curvature of the mold, we lose the benefit of surface tension naturally improving circularity and uniformity when the shell is suspended in space. If there are any defects in the mold they will be more directly imparted on the shell, considerably increasing anchor loss. It is possible that with further process development the GBB performance could rival that of the classic BB, but the

remainder of the discussion in this thesis pertains to the classic BB resonator shape shown in

Figure 3.12(a) unless noted otherwise.

	Hemispherical Shell	Cylindrical Shell	Egg Shell
$\dfrac{Q_{anchor}}{Q_{anchor_0}}$	1.15	0.16	0.02
$\dfrac{Q_{TED}}{Q_{TED_0}}$	1.36	0.23	0.73
$\dfrac{f_{WG}}{f_{WG_0}}$	0.99	0.91	1.1
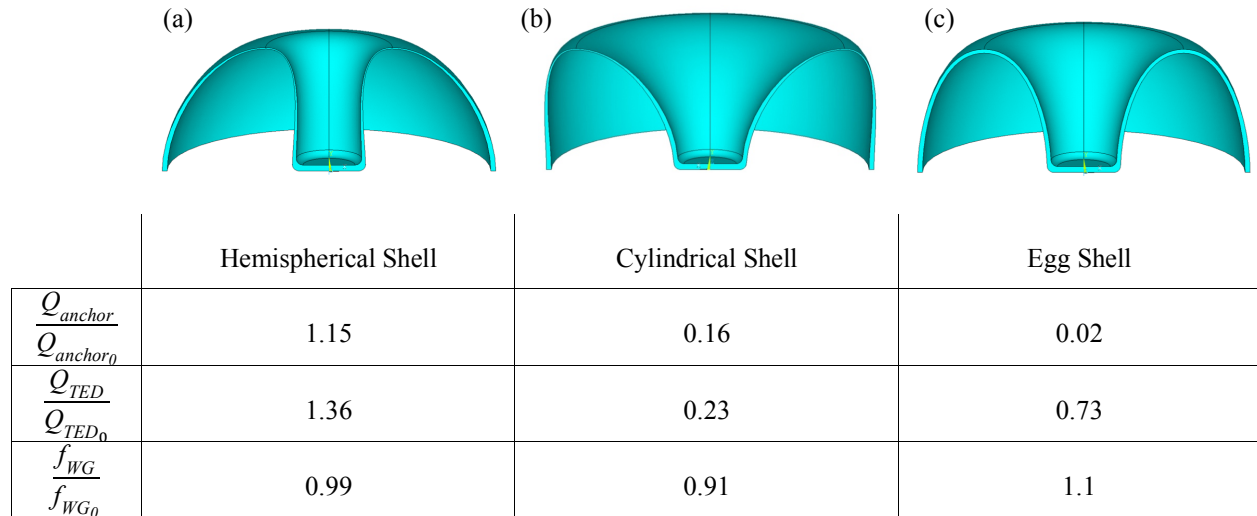
Figure 3.15: Finite element analysis of Q_{anchor}, Q_{TED}, and f_{WG} of different BB resonator shapes compared with a classic BB (Q_{anchor_0}, Q_{TED_0}, and f_{WG_0}).
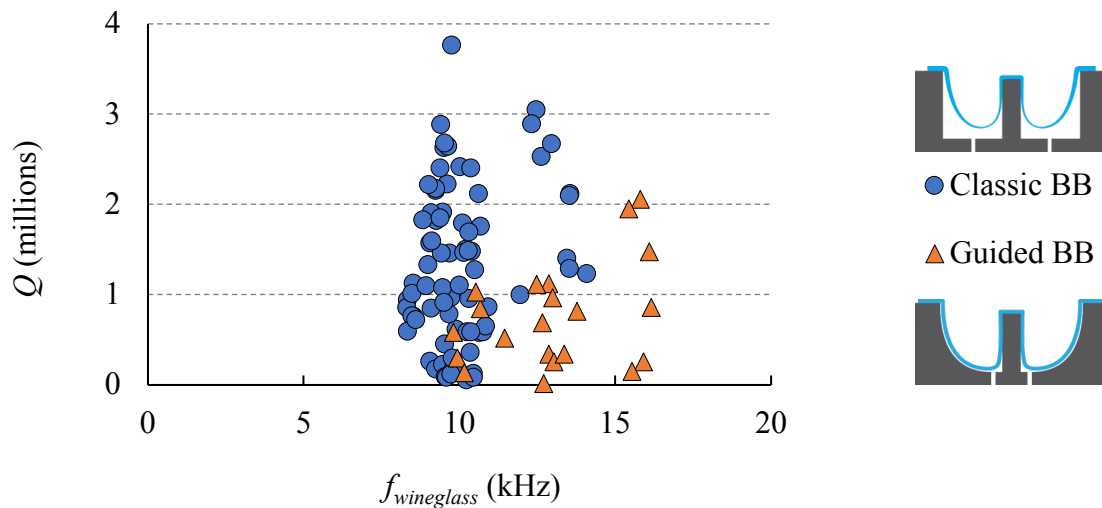
Figure 3.16: Comparison between Q of classic and guided BB resonators fabricated under similar conditions. Guided BB resonators tend to have higher frequency and lower Q.

3.3.5 Blowtorch Molding Process

Blowtorch molding has many advantages including automatic anchor alignment, rapid

prototyping, low cost, and the ability to form unique 3D structures that cannot be created with

any other technique. The process consists of a propane/oxygen blowtorch rapidly softening a FS

substrate so it can be vacuum formed into a graphite mold under the substrate, defining the resonator structure in only ~10 seconds. The torch is part of a semi-automated station, controlled by a LabVIEW program. It provides a high level of control and customizability, and can be used on a variety of materials with very high melting temperatures up to 2500 °C for the case of a propane-oxygen flame [67].

To begin the process, a fused silica substrate is placed onto a graphite mold. The blowtorch, located directly above the mold, is fed with electronically regulated propane and oxygen flows. The torch tip is fixed to a motorized z-axis platform whose motion profile during a reflow cycle is controlled through the LabVIEW interface. A FLIR SC7000 thermal camera is aimed at the graphite mold so the torch height can be controlled in a closed loop with the substrate temperature. For example, the torch approaches the FS substrate at a fixed speed until it reaches a set height, then remains there until the substrate reaches a set temperature and flows to the desired depth before retracting. Once the torch reaches the FS, it takes around 10 seconds to complete the reflow. The mold sits on a metal chuck that keeps it centered, dissipates heat, and applies an electronically regulated pressure to the mold cavity under the FS through holes in the bottom of the mold. When a new mold design or substrate thickness is first used, there is a brief period of tuning where the various molding parameters must be adjusted. Once the process is dialed it, it can run for several hours with minimal tuning. Including the time to place a flat substrate, reflow, and remove the molded substrate, shells can be molded at a rate of ~30–40 per hour. The molding process is depicted in Figure 3.17. A BB-2.5 resonator is shown immediately after molding in Figure 3.18.
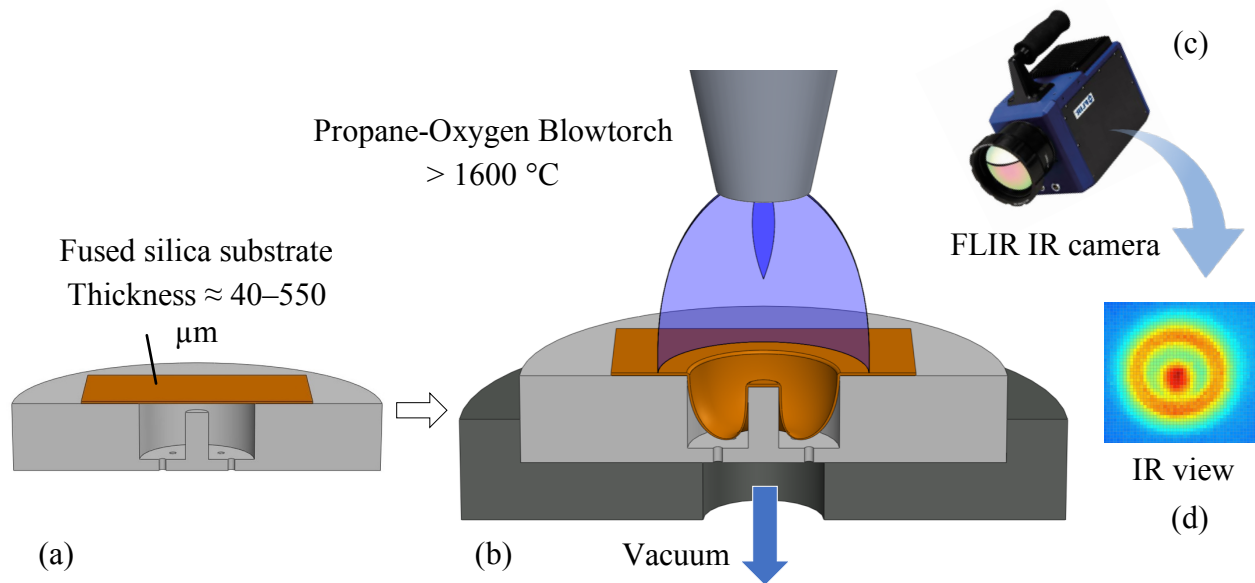
Figure 3.17: A fused silica substrate is placed on a machined graphite mold (a). A propane oxygen propane is lowered to heat and soften the fused silica until it reflows under vacuum (b). The torch motion sequence is guided by a FLIR SC7000 IR camera (c) to ensure repeatable molding conditions. The thermal image is skewed due to the angle of the camera (d), but as expected, the rim and the anchor post are the hottest regions.
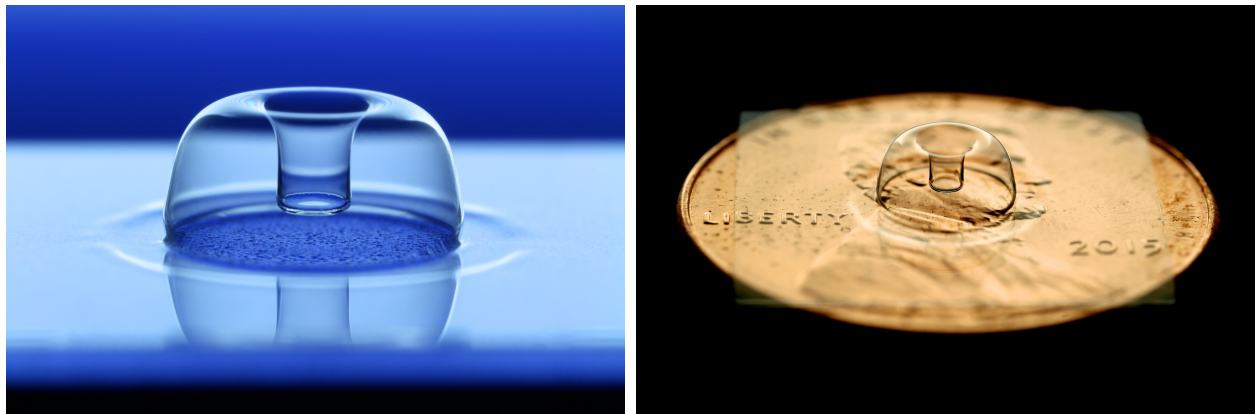
Figure 3.18: (Left) Molded BB-2.5 resonator, still attached to the square of bulk FS substrate. (Right) The same BB-2.5 resonator placed on a U.S. penny for size reference.

Molding the BB resonator over a monolithic graphite mold automatically aligns the shell's anchor stem to its outer rim in a single step, helping the BB resonator achieve low anchor loss. During molding, the FS only touches the graphite around the top of the outer wall that forms the shell rim and at the top of the anchor post, leaving the rest of the shell to hang in the air and form a naturally uniform shape. The torch smooths the surface of the suspended FS to a

low average roughness of 1.8 Å, as measured by an atomic force microscope (Figure 3.19). Birdbath resonators have a very high S/V ratio, making them sensitive to surface losses; a smooth surface is beneficial, as it helps reduce surface area [68]. This is discussed further in Section 6.6.
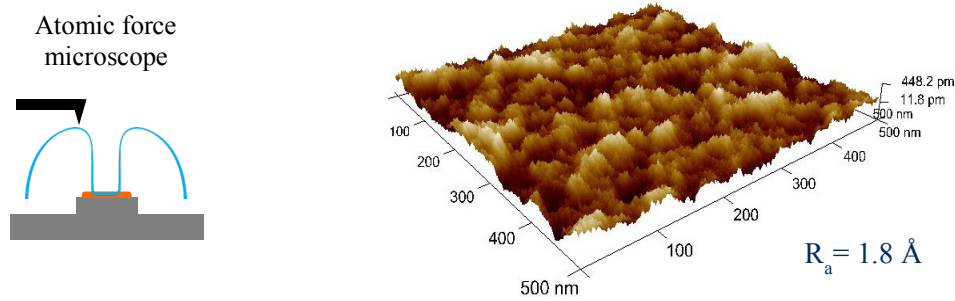
Figure 3.19: Atomic force microscope measurement of the surface roughness of a blowtorch-molded BB shell.

The original station, program, and process were built by Dr. Jae Yoong Cho; modifications were made to the blowtorch station and the reflow process over the course of this work to improve its functionality and repeatability, and ultimately the resonator performance.

Several modifications were made to the station to improve its functionality. An electronic *x-y* stage that can precisely position the graphite mold underneath the blowtorch flame was installed. The Tygon tubing was replaced with seamless stainless steel tubing with Teflon flex lines where necessary. The entire station was systematically shimmed and leveled to ensure square alignment of the torch fixture to the graphite mold. The torch fixture was modified to enable precise angular adjustments of the torch tip so it could be accurately aligned to the graphite mold. Many different torch tips were tried to understand how different flame shapes affect the molding process; the number and size of the holes in a torch tip determine the velocity and shape of the flame pattern, which are found to play an important role in the reflow process. Finally, a second station was built that will burn hydrogen and oxygen with a quartz torch head.

The new station was designed with all of the lessons learned from the original station and will be used in future research on this project.

Considerable time and effort were invested in developing the reflow process itself. There are many parameters that can be adjusted to control the behavior of the FS during reflow that are critical to creating high-performance BB resonators. Ultimately, the rate and depth of reflow must be controlled, which are not straight forward. The most important conditions for exerting this control are the temperature of the FS and the molding pressure and time. The pressure is set by an electronic pressure controller, and the molding time at the set temperature is chosen in the LabVIEW program; however, the temperature can be controlled by many different parameters, and ultimately, the reflow rate and depth are therefore affected by a number of different overlapping settings. These include the propane-oxygen gas flows, the shape of the flame, the distance between the torch and graphite mold, and the velocity of the torch motion. Changing one parameter may affect both the rate and depth of molding, while changing two or more parameters enables independent control over rate and depth. Eventually, an understanding of the role of each parameter was gained, and the settings were optimized to create a baseline recipe that is slightly modified for new mold designs or substrate thicknesses.

The temperature profile around the mold and the transfer of heat between the blowtorch, FS, and graphite are also critical parameters affecting the final shape of the shell [69]. Regions of the shell with greater thermal isolation, such as the anchor or the freely suspended FS, will heat up more than regions touching the bulk graphite. These regions will stretch more and flow more freely, presenting an opportunity to improve control over the final resonator geometry. FEM has been used to analyze the effect of mold temperature, T_{mold}, on the shell shape and thickness profile by assuming a constant mold temperature (Figure 3.20) [70]. Although the temperatures

do not precisely reflect experimental molding conditions, there is a clear trend for cooler and hotter molds. This study indicates that as the mold becomes hotter, the shape approaches that of the "Egg shell" BB resonator in Figure 3.15(c) that has an estimated 98% lower Q_{anchor} and 27% lower Q_{TED} than a classic BB, which is closer to Figure 3.20 (a–b). It is therefore important to manage thermal dissipation during molding by careful design of the mold and blowtorch motion sequence to ensure the shell does not overheat.

(a)	(b)	(c)	(d)
13 Thickness 99 (μm)	13 Thickness 99 (μm)	19 Thickness 99 (μm)	31 Thickness 98 (μm)
T_{mold} = 300 K	T_{mold} = 500 K	T_{mold} = 1000 K	T_{mold} = 1600 K
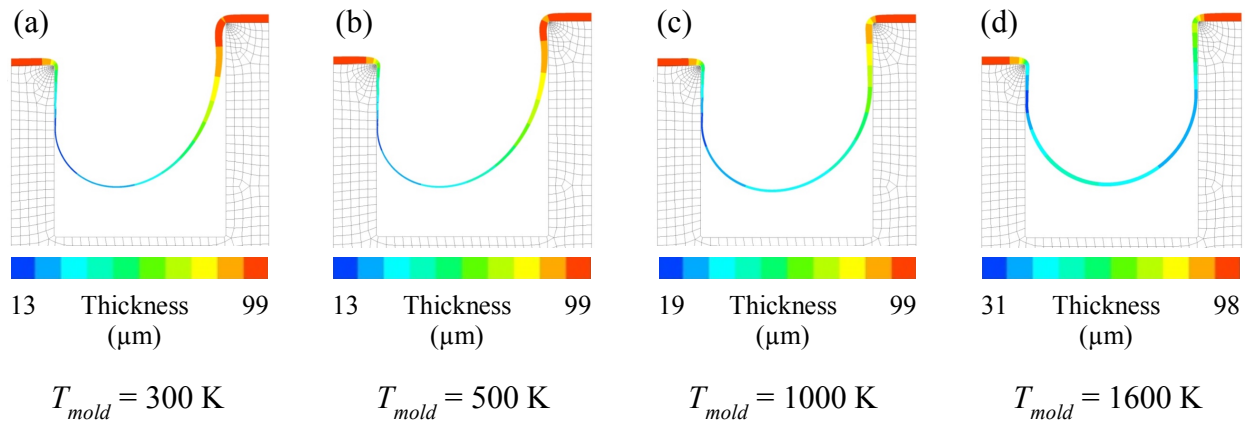
Figure 3.20: FEM of the effect of graphite mold temperature on shell shape and thickness for a BB-2.5 shell with starting substrate thickness of 100 μm. A cooler mold is expected to produce a more optimized shell profile based on the FEM results presented in Figure 3.15.

3.3.6 Shell Isolation

After molding, the shells must be isolated from the remaining flat bulk substrate from which they were molded. Depending on the shell radius, batches of nine (BB-5) or twenty-four (BB-2.5) shells are set into through holes in a silicon lapping jig wafer that is machined with a diamond core drill bit on a numerical control (NC) mill. The lapping jig is thicker than the shells are tall so the shells are protected inside the jig while the unwanted bulk substrates lie flat on the surface. The shells are surrounded on both sides with a thermoplastic polymer to hold them in place and protect them while the flat substrates are removed from the surface of the lapping jig with a mechanical lapping process. After lapping, the shell rims are exposed on the surface of the

wafer and are subsequently polished with chemical-mechanical planarization (CMP). This process is depicted in Figure 3.21. Figure 3.22(a) shows a photo of a batch of twenty-four BB-2.5 resonators in a lapping jig just after CMP, as well as micrographs of a shell rim after lapping (b) and CMP (c).
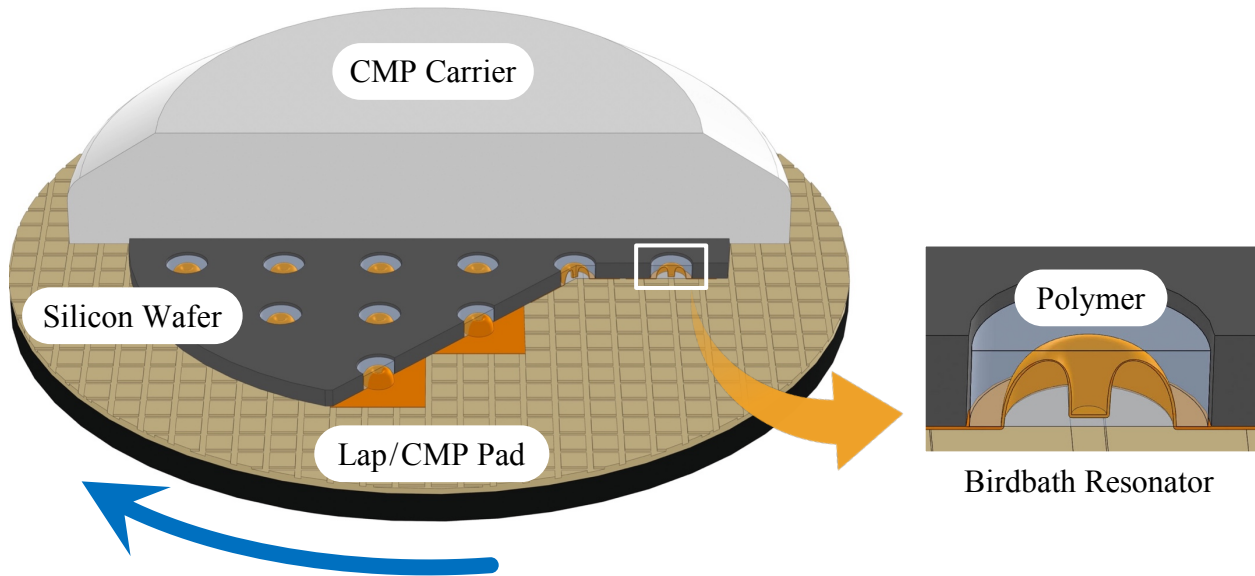
Figure 3.21: Shells are isolated from the flat bulk fused silica substrate from which they were molded by lapping the flat portion off of the surface of a silicon wafer. The exposed shell rim is then polished with CMP.
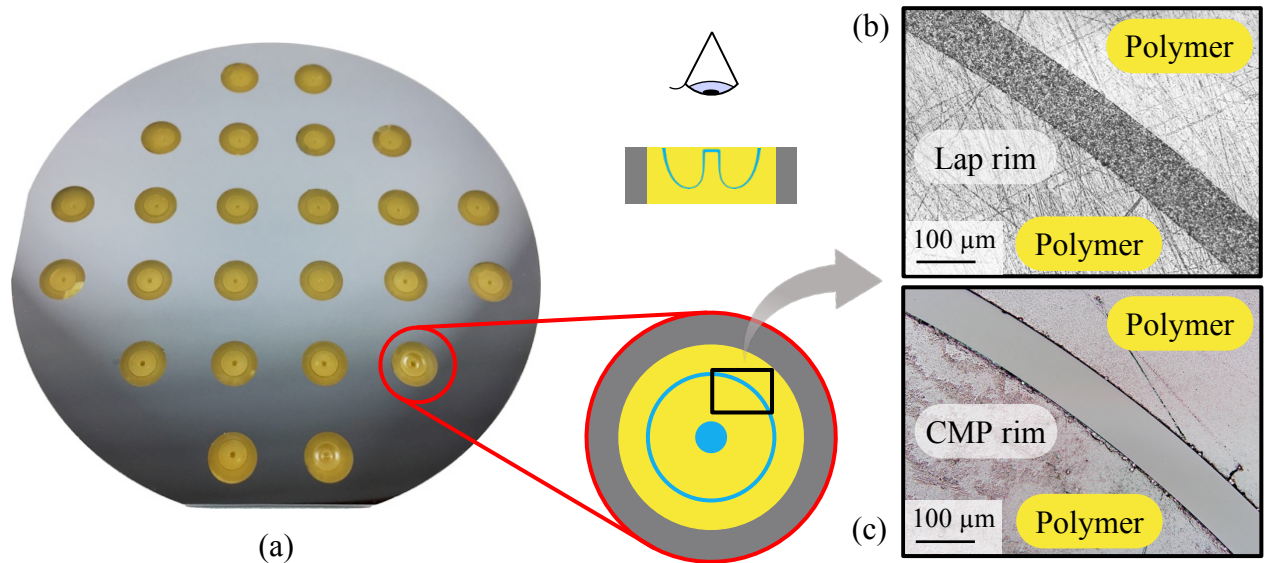
Figure 3.22: (a) A batch of twenty-four BB-2.5 shells in a silicon lapping jig after CMP. The shell rim is rough after lapping (b), but is then polished smooth with CMP (c).

To retrieve the isolated shells, the thermoplastic is dissolved in the appropriate solvent and the shells are further cleaned in solvents and DI water. This completes the fabrication process of birdbath resonators. At this point, they can either be mounted to a carrier substrate for testing or packaged with electrodes for gyroscope operation. Application of a conductive layer on the shell is required for gyroscope operation, but is optional for resonator performance evaluation. The testing procedure is discussed in Section 4.1. Conductive layer optimization is discussed in Chapter 5.

Thermoplastic (A)   Thermoplastic (B)

Thermoplastic (C)   Thermoplastic (D)
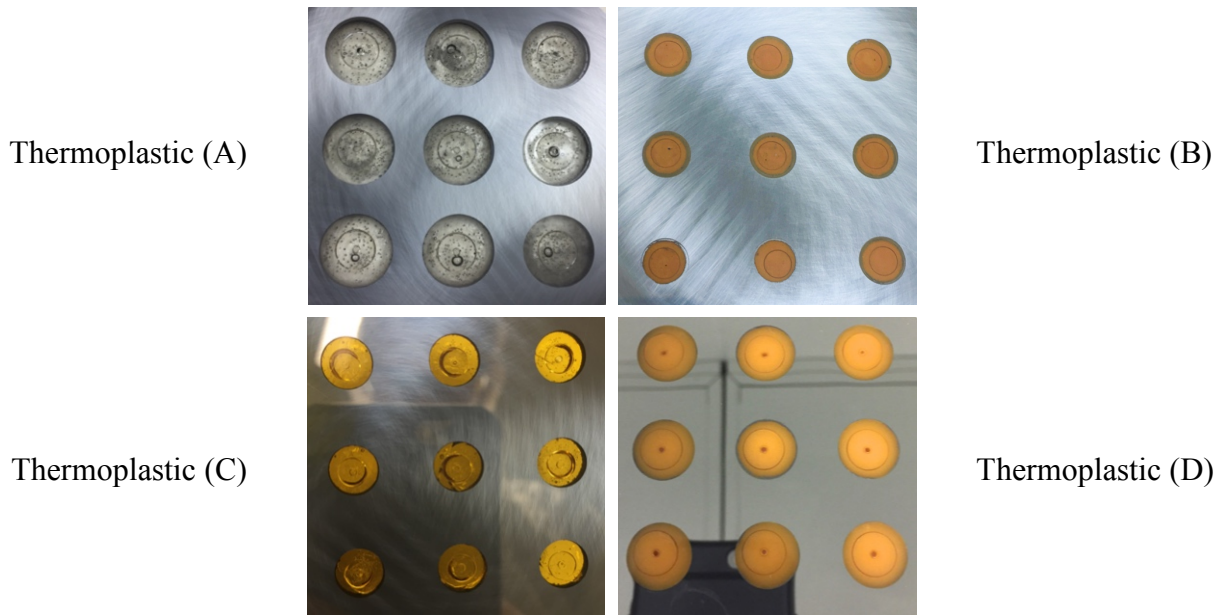
Figure 3.23: Photos of silicon lapping jigs with shells embedded in the various thermoplastics that have been tried during the lapping and CMP processes. TP (A) and (D) are shown with BB-5 shells, while (B) and (C) are shown with BB-2.5 shells.

Successfully isolating the shell from the bulk substrate is a critical step in fabricating BB resonators. The quality of the rim is determined at this stage, and the symmetry of the shell can be degraded in some situations. The lapping and CMP recipes must be optimized to remove material at a reasonable rate to manage damage and ensure the finished resonators have a completely polished rim surface. The properties of the thermoplastic (TP) used to hold the shell in place are key to the success of this step. It must protect the shells from damage, keep them

from shifting, and then be completely removed after polishing. Due to BB resonators' sensitivity to their surface condition, the ability to remove the TP is critical. Other considerations include melting temperature and how badly the thermoplastic clogs the diamond lapping pad, which reduces the lapping rate. Considerable effort has been made over the course of this work to optimize the shell isolation process. Several different thermoplastics have been tried; they are referred to as TP (A), (B), (C), and (D) (Figure 3.23). Figure 3.24 shows the typical outcome of shell rims when using each TP.

Figure 3.24: Optical micrographs of typical rim conditions observed after lapping and CMP of BB resonator rims that are supported by the various thermoplastics shown in Figure 3.23.

TP (A) is a hard, clear polymer with a flow point of 71 °C and viscosity of 6,000 cP. It is soluble in acetone and can be completely removed with proper solvent cleaning. It also has the benefit of minimally clogging diamond tools compared to waxes, so the lapping rate remains consistent. Though this material worked well enough during process development, it did not always hold the shells rigidly against the lapping pad. Profilometry scans revealed that shells would shift during CMP, causing parts of the shell to recede below the surface and therefore not be polished (Figure 3.25). Later experiments suggest that the shells may have been moving during lapping as well, causing them to be lapped at an angle; simulations indicate this would increase Δf, $\Delta(1/\tau)$, and anchor loss. Even the regions that were polished often had some undesirable chipping around the rim edges.

TP (B) is a brown material with a much higher flow point of 150 °C and higher viscosity of 9,000 cP that is soluble in isopropyl alcohol (IPA). It consists of a polymer mixed with an

insoluble powder. Although more difficult to work with due to its higher flow point and higher viscosity, CB 590 yielded better polishing results, keeping the resonators in place and allowing the rims to be completely polished. Unfortunately, the top layer is dissolved in CMP slurry, releasing some of the powder particles and removing support in this region. These particles increased the chipping along the unsupported edges of the rim as seen in Figure 3.24(B). Furthermore, the powder proved very difficult to remove from the surface of the shells after polishing and the polymer tended to leave a residue.
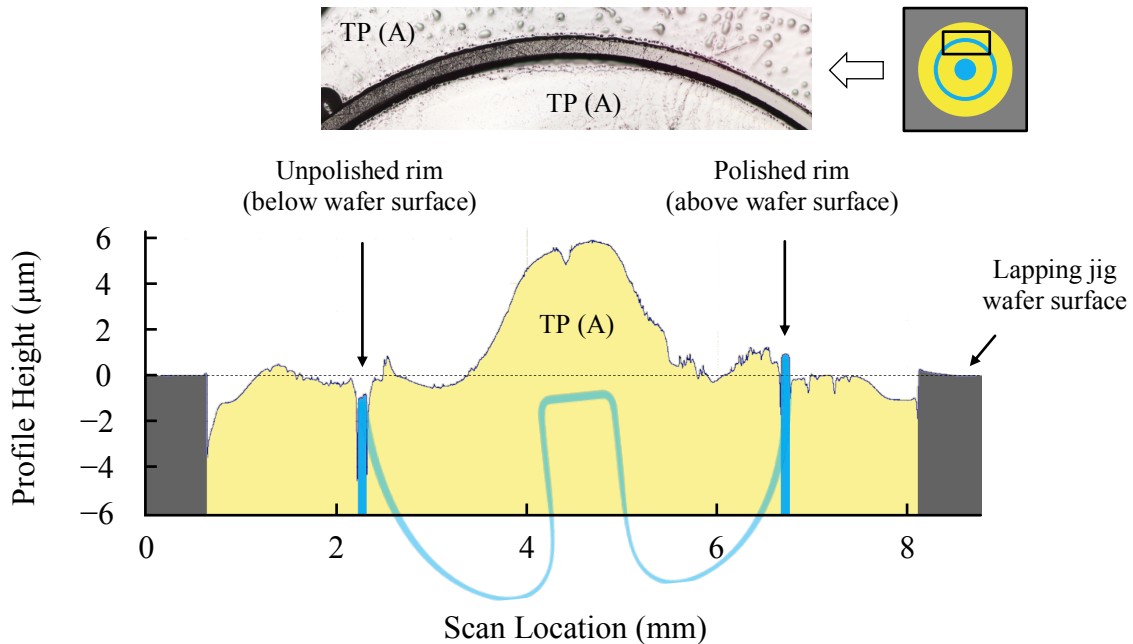
Figure 3.25: Profilometry scan and an optical micrograph showing a shell that has tilted relative to the silicon lapping jig because the surrounding Thermoplastic (A) did not hold it rigidly in place. This caused some of the rim to shift below the wafer surface, preventing it from being polished. Colors added for clarity. BB resonator overlay not shown to scale on y-axis.

TP (C) has a similar composition to TP (B), but without any powder. TP (C) produces excellent polishing results, keeping the resonator pressed up against the lapping and CMP pads (Figure 3.24(C)). Although the top ~50 µm is dissolved by the CMP slurry (Figure 3.26), TB (C) still effectively supports the sidewalls and prevents chipping of the rim. Material removal is slow, as it clogs the lapping pad much more than TP (A). TP (C) is also brittle and frequently

cracks during lapping. In many cases the rim would crack as well, likely due to the high rigidity of the TP. There also were some challenges removing TP (C). It could largely be removed in IPA, but tended to leave behind a stubborn residue. Various heated solvents and acids in conjunction with oxygen plasma cleaning did not completely clean the shell.
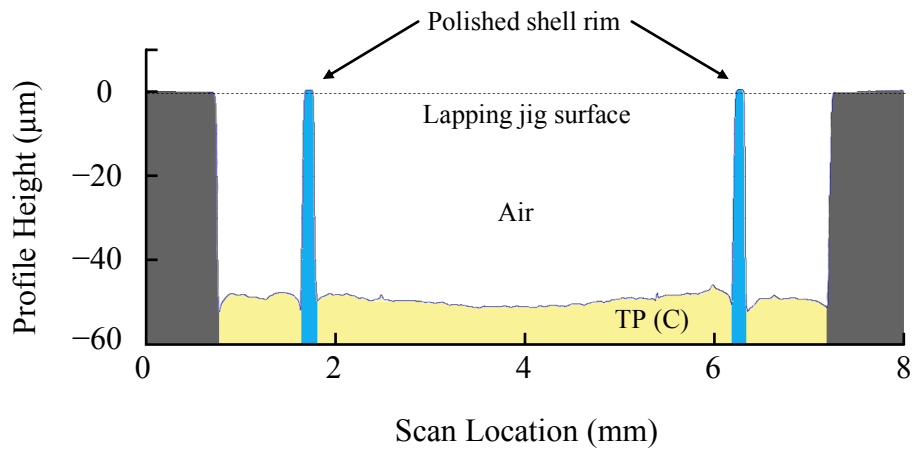
Figure 3.26: Profilometry scan of a BB shell rim that has been encapsulated in TP (C) and polished with CMP. The CMP slurry dissolves some of the TP, leaving ~50 μm of unsupported rim. Colors added for clarity.

TP (D) is a tan material with a melting point of 70 °C that is soluble in heated xylenes. Although it clogs the lapping pad more than TP (C), TP (D) produces equally good rim polishing results (Figure 3.24(d)), is not dissolved by CMP slurry, and has enough flexibility to prevent the rims from cracking. It also has the benefit of being quickly and almost completely removed during solvent cleaning. For these reasons, TP (D) was determined to be the best option.

A number of solvent and acid cleaning sequences were tried, but even for TP (D), a small amount of TP residue remains after cleaning the shells. To address this, a protective metal barrier deposition is added before the shells ever touch any TP. The shells are sandwiched between a pair of 4" silicon wafers with through holes, then 50/1000/50 Å of Cr/Au/Cr are sputtered on each side. This process is shown in Figure 3.27 for BB-5 resonators. The shells are then isolated as described above. After cleaning away TP (D), the metal is removed with the appropriate

etchants. The addition of the metal barrier has a clear positive impact on performance

repeatability and maximum Q and τ, as shown in Figure 3.28.
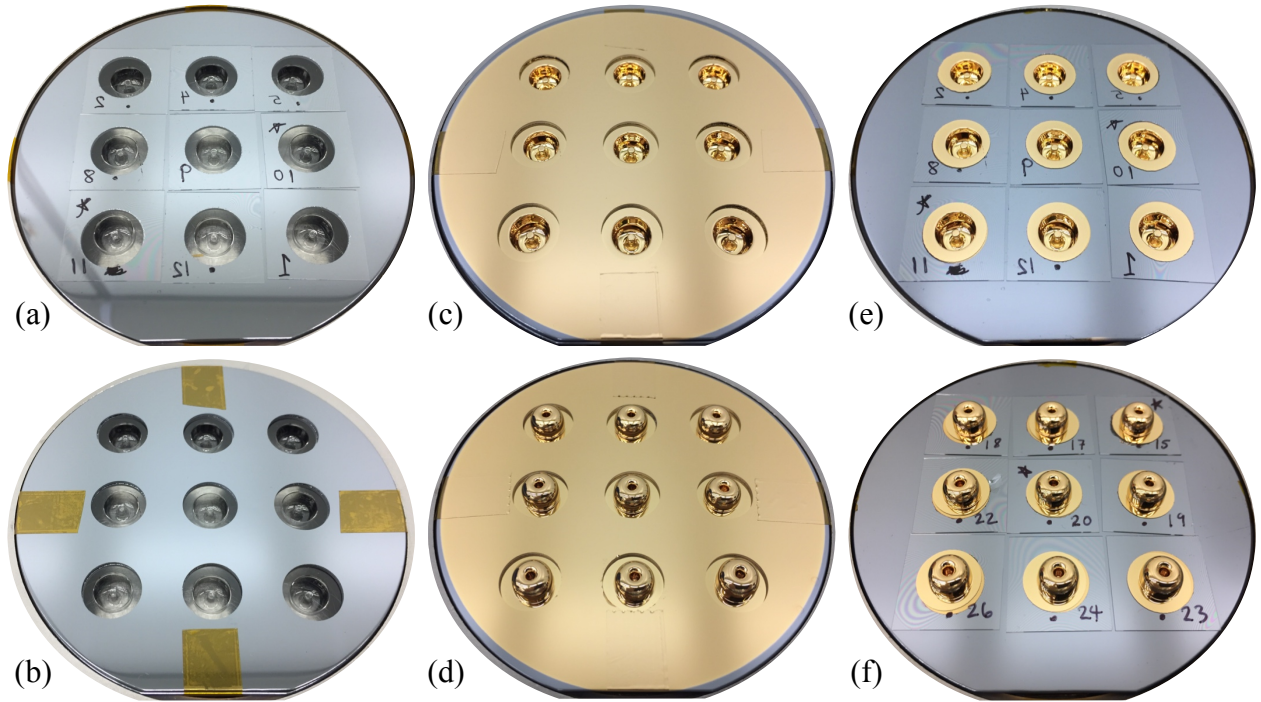
Figure 3.27: Deposition of a protective metal barrier layer before lapping and CMP. (a) BB-5 shells are set into through holes in a 4'' silicon wafer. (b) a second wafer is added, and the two are taped together. 50/1000/50 Å of Cr/Au/Cr are sputtered on the inside (c) and then outside (d) of the shells. The wafers are separated to retrieve the coated shells (e–f).
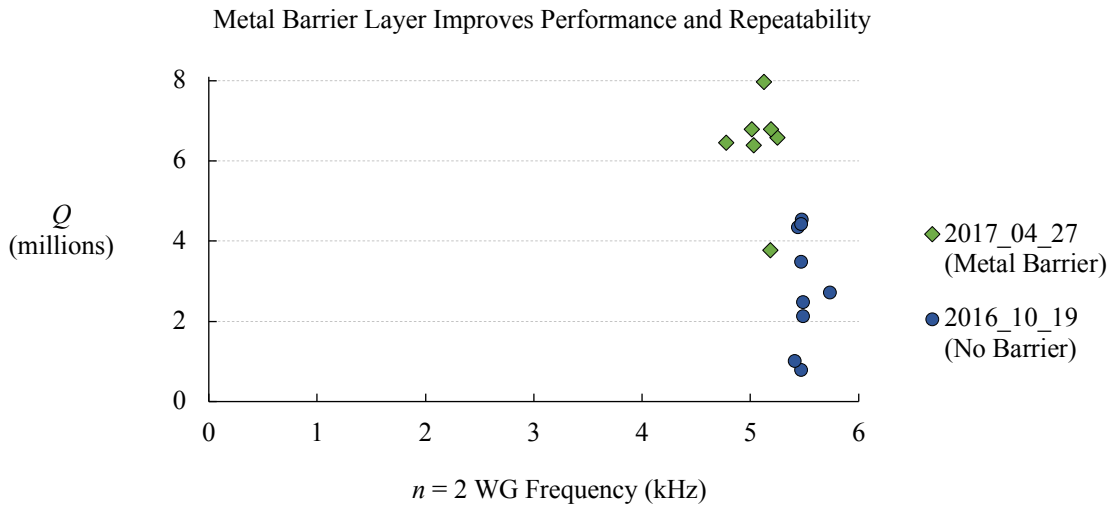
Figure 3.28: Depositing a metal barrier layer on the shells before encapsulation in thermoplastic improves the Q and Q repeatability within a given batch.

In addition to preventing TP from contacting the shell surfaces, the metal barrier layer also protects against the colloidal silica particles in the CMP slurry. Examining the shells in an SEM after CMP reveals copious quantities of silica particles that are caked onto the upper 20 μm of shell wall just below the rim (Figure 3.29). TP (D) is the most effective at supporting the sides of the shell, as shown in Figure 3.24, but the slurry still works its way between the shell and TP. Ultrasonic cleaning immediately after CMP does not remove the particles, but having a metal barrier layer prevents them from ever reaching the shell surface. This is critical, as these particles can be a major source of energy loss. This is discussed in Section 6.6.2.
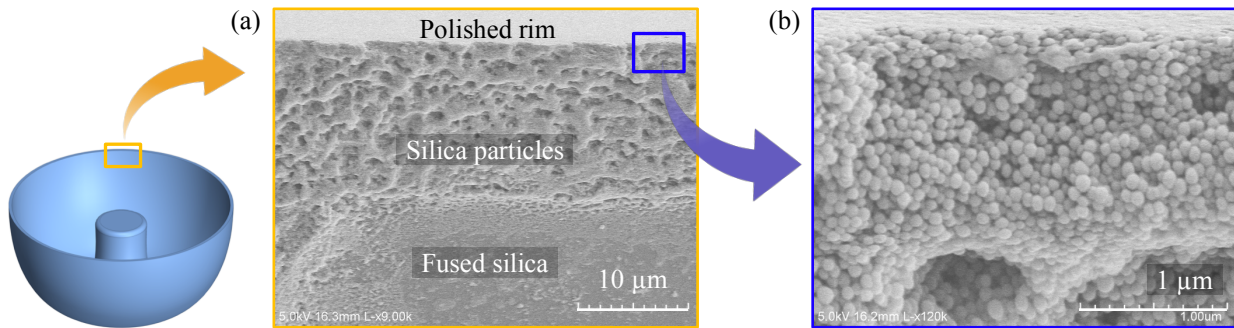
Figure 3.29: SEM micrographs of the inner wall of a BB-5 shell near the rim reveal caked on silica nanoparticles deposited during CMP onto the top 20 μm of the shell wall below the polished rim surface.

3.3.7 Assembly to Carrier Substrate

If the shell is to be used as a gyroscope, it is coated with a conductive surface layer and assembled to an electrode package at this point. To characterize only the resonator properties, cleaned BB resonators are each attached with glass frit to a carrier substrate for handling and testing. The silicon carrier substrates have a raised pedestal in the center, produced with deep reactive ion etching (DRIE), as shown in Figure 3.30(a). Resonators of several sizes attached to carrier substrates with glass frit are shown in Figure 3.1. Glass frit is commonly applied with screen printing in MEMS applications to produce wafer-level hermetic seals. Glass frit is a paste that is applied at room temperature, then fired to produce a translucent glass. Here, the frit is

fired at 450 °C, the shell is attached, then the assembly is cooled at 5 °C/min. This slow cooling step minimizes the residual thermal stress at the attachment point due to the mismatch in α between the frit (9 ppm/°C at 260 °C [71]), silicon (3.3 ppm/°C at 100 °C [72]), and fused silica (0.57 ppm/°C average from 0–200 °C [60]). Frit is chosen for resonator attachment for its rigidity, which helps minimize anchor loss. This is discussed in Section 6.4.
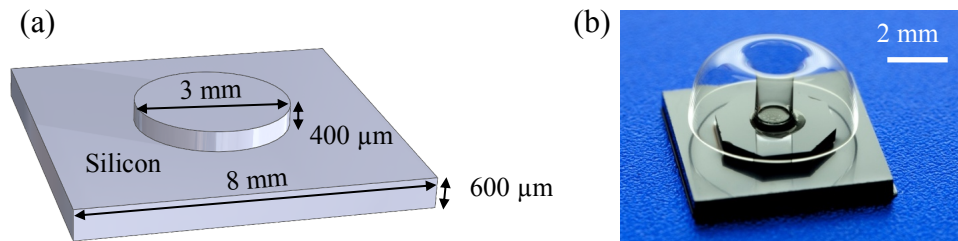
Figure 3.30: Before testing shell resonators, each one is attached to a silicon carrier substrate similar to that shown in (a) so they can be safely handled. (b) A BB-2.5 resonator attached to a silicon substrate with glass frit. The silicon carrier substrate dimensions are scaled to match the size of the FS resonator.

3.3.8 Conductive Layer Deposition

A conductive layer may now be added, typically with sputtering. The carrier substrates are adhered to a silicon carrier wafer that can be loaded into the sputtering tool. The rotation rate of the wafer is chosen to have an integer number of rotations during each conductive layer deposition. The typical films used are Cr/Au or Ti/Pt, with thicknesses of 10/50Å. The Cr and Ti serve as adhesion layers. The Au and Pt are the primary conductive layers, chosen for their resistance to corrosion; however, deposition of a metal layer, even only 60-Å-thick, reduces τ by ~50%. Optimization of the conductive layer is discussed in detail in Chapter 5.

Chapter 4

Measurement Results and Techniques

This chapter presents measured BB resonator performance over the last four years and the measurement techniques used to collect the data. Many of the results are given in terms of Q rather than τ, as Q is the true measure of energy dissipation. A high Q reduces thermo-mechanical noise and is important for achieving low gyroscope ARW. Some results are presented in terms of τ, which is the inverse of damping, and depends on both frequency and Q. Long and symmetric τs are important for achieving low gyroscope bias instability. Results from metallized resonators fabricated in the first year of this work as well as uncoated resonators fabricated in the following three years are shown. Measurement results for resonators with optimized conductive coatings that were developed more recently are presented in Chapter 5.

4.1 Resonator Testing

Once rigidly attached to silicon substrates, resonators are tested in vacuum using either electrostatic (ES) transduction or piezoelectric drive and laser Doppler vibrometry (LDV) readout. The frequencies of their $n = 2$ WG modes are identified and τ for each mode is measured by analyzing the free vibratory decay of the resonant rim motion. The velocity and amplitude of the rim decay exponentially during ring-down and can be described by

$$V(t) = V_0 e^{-\lambda t} \tag{4.1}$$

where *V(t)* is the rim velocity as a function of time, *t*, V_0 is the initial rim velocity, *e* is Euler's number, and λ is the decay rate. The same equation applies for rim displacement amplitude. The ring-down time constant, τ, is given as

$$\tau = 1/\lambda \tag{4.2}$$

so *V(t)* can also be written as

$$V(t) = V_0 \, e^{-t/\tau} \tag{4.3}$$

For each measurement, τ is extracted from the ring-down plot and *Q* is calculated with $Q = \pi \tau f$.

4.1.1 Electrostatic Testing

Resonators with a conductive surface layer are tested in a vacuum probe station at a pressure of around 10 µTorr. The experimental setup is depicted in Figure 4.1. The shell is biased to ~200 V with a long needle probe that can reach the bottom of the inside of the anchor. Custom probe tips with conformal electrodes designed to align to the shell walls are then positioned ~100 µm from the surface. To locate the WG modes, a swept sine wave is applied to the drive electrode with a network analyzer. The current induced in the sense electrode is amplified with a transimpedance amplifier (TIA) and fed back into the network analyzer. For each WG mode frequency, the shell is driven into resonance, then the drive signal is removed and the vibratory decay is recorded with LabVIEW so τ can be calculated.

This method has the advantage of emulating the actual setup of a packaged gyroscope. It also minimizes (but does not eliminate) excitation of parasitic modes; however, due to the relatively large electrostatic gap and the long wires, the signal is rather noisy. This technique also inherently requires a conductive coating on the shell that decreases τ, making it difficult to study the effects of other fabrication steps.
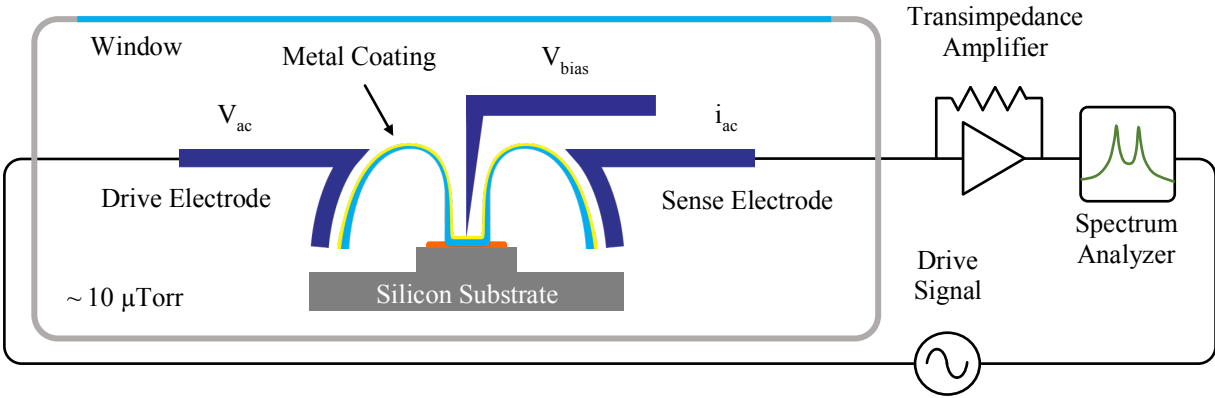
Figure 4.1: Setup for electrostatic testing of BB resonators with a metal surface layer. Testing is performed in a vacuum of around 10 μTorr. Custom electrodes drive and sense the shell motion. Signal generation and analysis is performed with a spectrum analyzer.

4.1.2 Optical Testing

Resonators with or without a conductive layer can be tested optically, as depicted in Figure 4.2(a). The silicon carrier substrate is attached to a piezoelectric actuator, then loaded into a custom vacuum chamber that is pumped down to <10 μTorr. The piezoelectric actuator produces vibrations along the longitudinal axis of the BB stem that excite the WG modes. An LDV is used to measure the radial velocity of the resonator rim in the direction of the LDV objective. We have seen that testing the same metal-coated resonator with both electrostatic and optical methods yields the same results, confirming the viability of both techniques.

Optical testing has the advantage of being able to evaluate bare fused silica shells so their maximum τ before further processing can be measured. The LDV can also rapidly and accurately identify the frequencies of many resonant modes, including tilting, vertical, and WG modes, as shown in Figure 4.2(b). This is both an advantage and a disadvantage, as energy cannot be delivered exclusively to the WG modes due to the nature of the piezoelectric actuation. For this reason, it is important to apply a band pass filter to the measured signal. Failure to filter the signal causes inaccurate measurements due to the inclusion of parasitic mode energy when measuring τ of a WG mode. One or both modes may appear better or worse than they actually

72

are depending on the alignment and τ of the parasitic modes. The interference is typically from the degenerate tilting modes that have frequencies around $0.25 \cdot f_{WG}$ but similar values of τ. Thanks to the large frequency separation between the WG and parasitic modes, filtering is quite effective, so LDV has been the preferred measurement technique due to its speed, accuracy, and ability to measure uncoated shells.
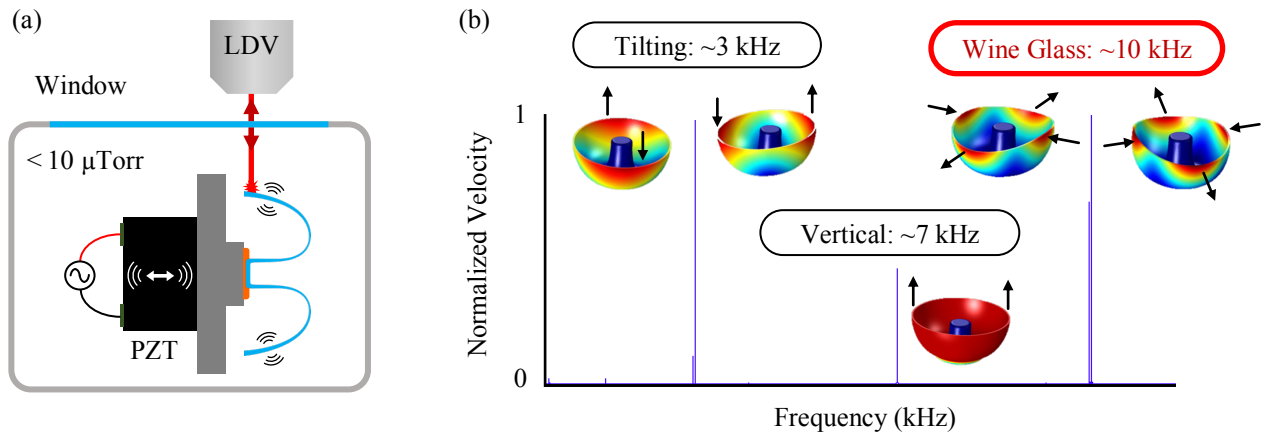
Figure 4.2: (a) Setup for testing BB resonators with laser Doppler vibrometry. A piezoelectric transducer attached to the Si carrier substrate drives the BB resonator into resonance. This method of transduction can excite several resonant modes, as illustrated by the FFT of a chirp signal applied to a BB-2.5 resonator (b).

4.2 Resonator Performance Results: Non-Optimized Conductive Layer on Fused Silica

The background work and initial process development for the BB resonator and BRG were performed by Dr. Jae Yoong Cho. An incredible amount of effort was required to bring the project to the point where BB resonators exhibited a measurable Q. At that point, Q values were typically less than 100k and τ was typically less than 3 s for BB-2.5 resonators. The best device had a Q of ~250k and τ of ~8 s. The goal of this thesis work has been to understand and mitigate the dominant energy loss mechanisms that were limiting resonator performance. The progress of Q improvement over the first year for metallized BB-1.5 and BB-2.5 resonators is shown in Figure 4.3. Only three batches of BB-1.5 resonators are shown here. Each data series represents devices produced in one blowtorch molding run.

Metallized BB Resonator Q Improvement Over Time
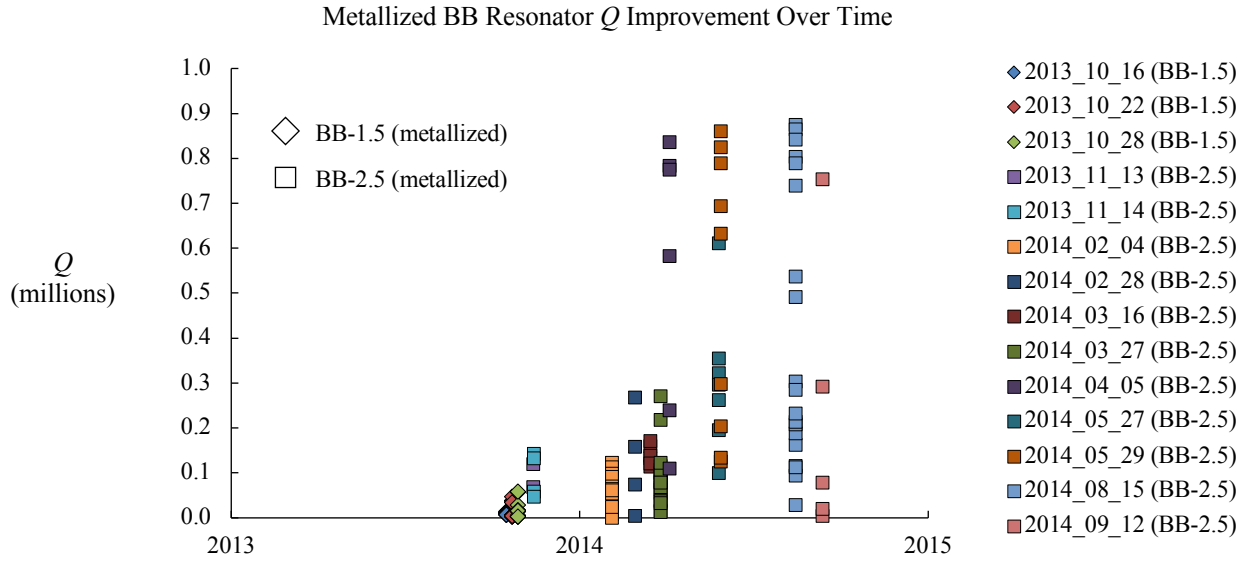
Figure 4.3: The Q achieved for BB-2.5 resonators rapidly improved in the first year, primarily due to the discovery of high energy dissipation caused by thick metal layers. Each point represents averaged values for both n = 2 WG modes.

Initial devices were coated with 30/300 Å Ti/Au or 30/1000 Å Cr/Au. The first major improvement came in early 2014 with the realization that applying a thinner metal layer increases Q. This increased the performance ceiling, but improvements in graphite mold design, blowtorch molding parameters, and shell isolation were needed before the Qs began to approach 1 million. Even as Q and τ were increasing, the fabrication repeatability was still rather poor. Figure 4.4 shows the frequency and Q distributions for each batch; they reveal rather loose grouping. This is due to variation in both the molding and shell isolation processes. Early mold designs did not effectively control thermal distribution and dissipation; this led to rapid erosion of the graphite and therefore variation in shell profile. The original thermoplastic used during lapping and CMP was also not reliable, and allowed shells to shift during lapping and CMP. These issues contributed to the poor repeatability seen in early batches of BB resonators.
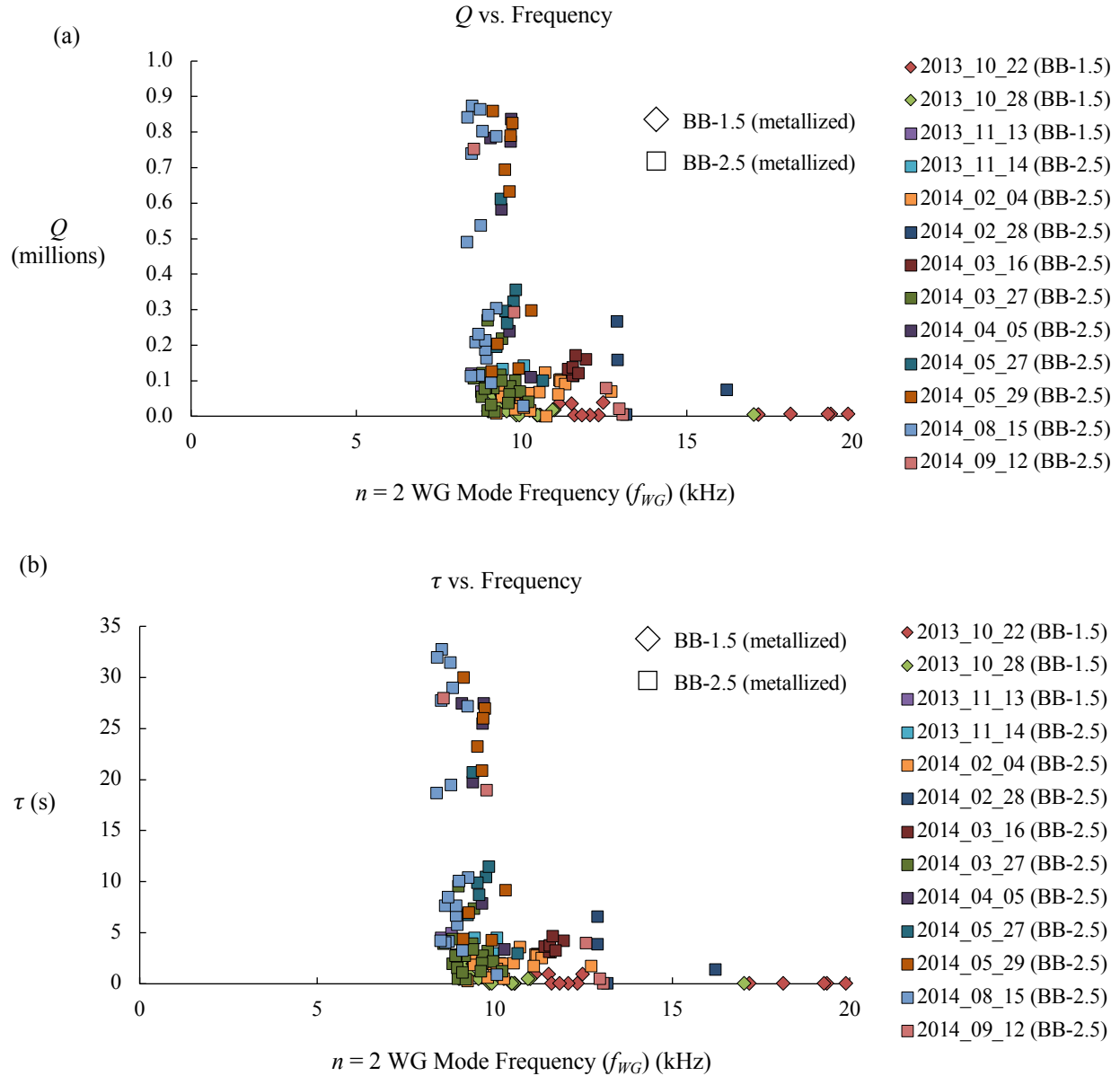
Figure 4.4: Early fabrication techniques had poor repeatability. The results within a given batch are not clearly grouped and tend to include a wide range of Qs (a), τs (b), and frequencies. Each point represents averaged values for both n = 2 WG modes. The 2013_10_16 BB-1.5 batch has high frequencies of ~25–50 kHz, it is excluded from this plot.

Fabrication challenges also led to large frequency splits (*Δf*) between the *n* = 2 WG

modes. A summary of *Q* vs. *Δf* for various metallized resonators is shown in Figure 4.5. There is

not a clear relationship between *Δf* and *Q*, but it is evident that BB-1.5 resonators tend to have

particularly high *Δf*. This can be understood by considering the greater effect of fabrication

imperfections on a smaller structure. If the CNC mill that machines the graphite molds holds a

tolerance of 10 μm, that 10 μm error will have a greater effect as the resonator size scales down and the shell imperfection becomes larger proportional to the major resonator dimensions. The same issue may exist with lapping. If the lapping tool removes material at a slight angle, the impact of this imperfection will become larger as resonator size scales down. These defects will cause some percentage of frequency difference between the $n = 2$ WG modes, so in addition to larger Δf for smaller resonators, Δf will be higher for resonators with higher f_{WG}.
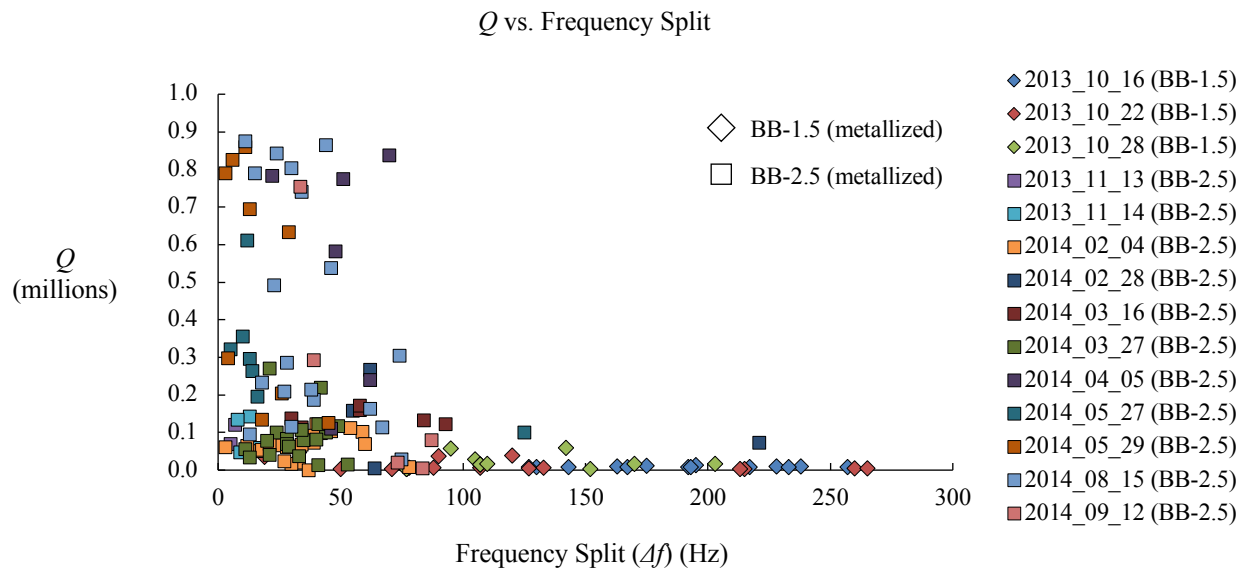
Figure 4.5: Although there is not a clear trend for increasing Q as Δf decreases, devices with Δf above 75 Hz tend to have low Q. Each point represents the averaged Q of both n = 2 WG modes.

Damping mismatch, $\Delta(1/\tau)$, is an important factor for producing a gyroscope with low bias and bias instability, as discussed in Section 2.9. Figure 4.6 shows the relationship between Q and $\Delta(1/\tau)$ for metallized BB-2.5 resonators. BB-1.5 resonators are not included because their τ measurements were not accurate enough to reliably calculate $\Delta(1/\tau)$. There appears to be an upper and lower bound on τ as $\Delta(1/\tau)$ decreases. Resonators with a low damping mismatch do not have low τ and resonators with high τ do not have high damping mismatch. The same trend appears when comparing $\Delta(1/\tau)$ to Q. The reason for this is not necessarily straightforward. It depends not only on τ symmetry, τ_1/τ_2, but on how long the τs are. If we assume a fixed

76

proportionality between τ_1 and τ_2, say due to a certain fabrication imperfection that causes asymmetry, $\Delta(1/\tau)$ will be lower for longer values of τ. This is illustrated in Figure 4.7 for the case where $\tau_1/\tau_2 = 0.9$.
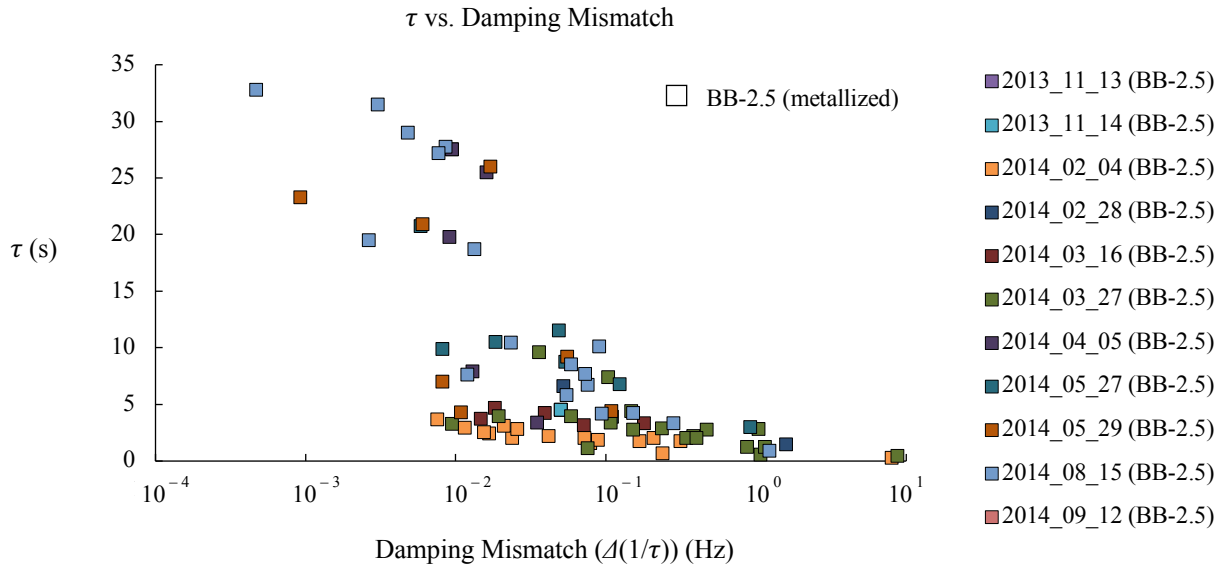
Figure 4.6: There is a clear trend of increasing τ as $\Delta(1/\tau)$ decreases. There appears to be an upper and lower bound on the relationship between Q and $\Delta(1/\tau)$. Each point represents averaged τ for both n = 2 WG modes.
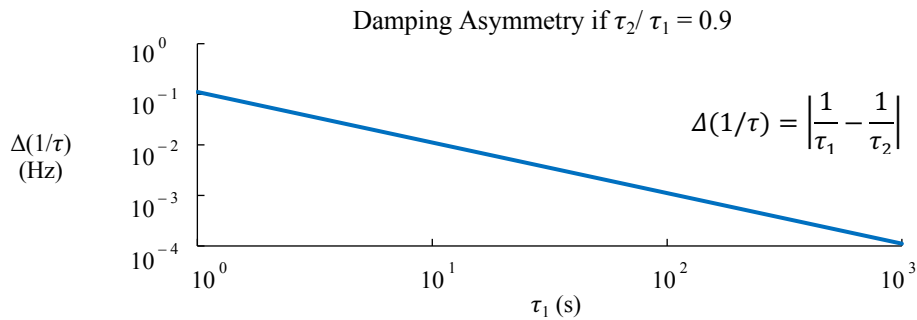
Figure 4.7: If there is a fixed 10% difference between τ_1 and τ_2, $\Delta(1/\tau)$ will improve as τ increases.

To differentiate between improvement in $\Delta(1/\tau)$ due to longer τ and improvement due to better τ symmetry, τ_1/τ_2 is plotted against $\Delta(1/\tau)$ (Figure 4.8). For a given τ symmetry, resonators with a lower $\Delta(1/\tau)$ have longer τs than those with higher $\Delta(1/\tau)$. Metallized resonators with longer τ achieve about two orders of magnitude better (lower) $\Delta(1/\tau)$ than those with shorter τs. Since it is not possible to fabricate perfect resonators with $\tau_1 = \tau_2$, it is

77

advantageous to maximize τ as well as τ symmetry to reach the desired gyroscope performance goals. The effects of individually maximizing τ and τ symmetry are discussed in Section 4.3.

τ_1/τ_2 vs. Damping Mismatch

Legend:
- 2013_11_13 (BB-2.5)
- 2013_11_14 (BB-2.5)
- 2014_02_04 (BB-2.5)
- 2014_02_28 (BB-2.5)
- 2014_03_16 (BB-2.5)
- 2014_03_27 (BB-2.5)
- 2014_04_05 (BB-2.5)
- 2014_05_27 (BB-2.5)
- 2014_05_29 (BB-2.5)
- 2014_08_15 (BB-2.5)
- 2014_09_12 (BB-2.5)
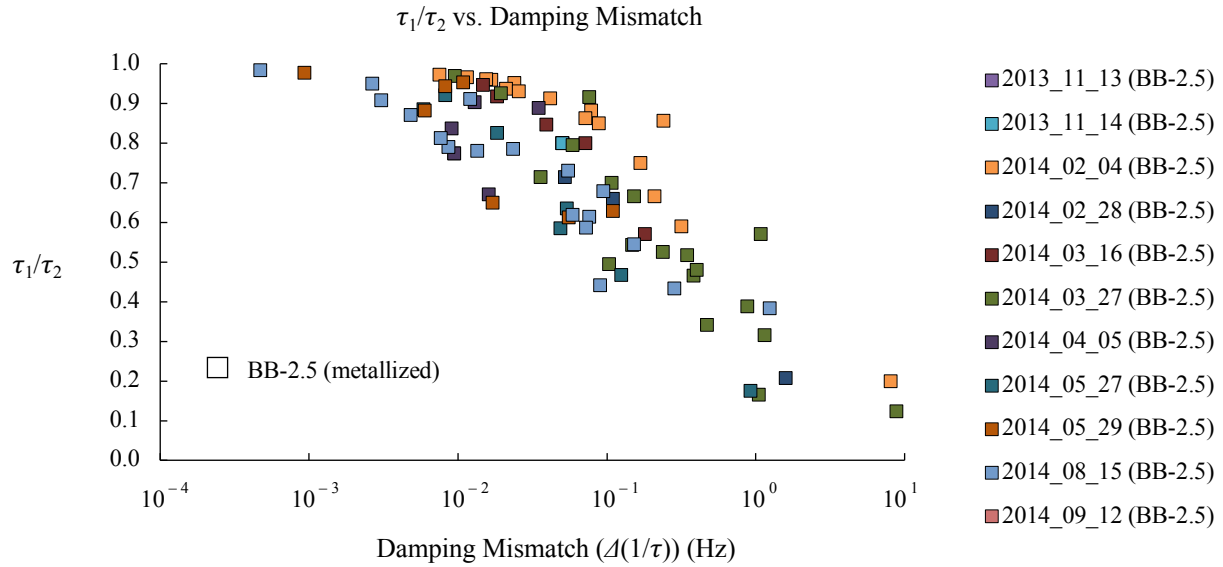
Figure 4.8: Comparing τ_1/τ_2 to $\Delta(1/\tau)$ reveals how much of the correlation seen in Figure 4.6 is due to the benefit of having a long τ and how much is from τ symmetry. Resonators with the same τ_1/τ_2 but with lower damping mismatch have longer τs.

4.3 Resonator Performance Results: Uncoated Fused Silica

At the end of 2014, focus was shifted to fabricating uncoated BB resonators so the performance of the resonator itself could be optimized without conflating the effects of the conductive layer. The Qs of all resonators fabricated and tested over the last four years, including both metallized and uncoated, are summarized in Figure 4.9. The last batch in 2014 was the first to be tested without a conductive layer, and Q reached around 3 million. Performance stagnated until 2016 while the fabrication process parameters were optimized with short loop fabrication runs. Changes to the graphite mold design, blowtorch molding technique, lapping and CMP processes, and post-fabrication baking led to the rapid improvement in performance seen during 2016 and 2017. The introduction of BB-5 designs enabled even higher Qs thanks to their lower S/V ratios, reaching up to around 10 million. This is the highest Q factor we are aware of for a micro shell resonator of this size-scale in the kHz frequency range.
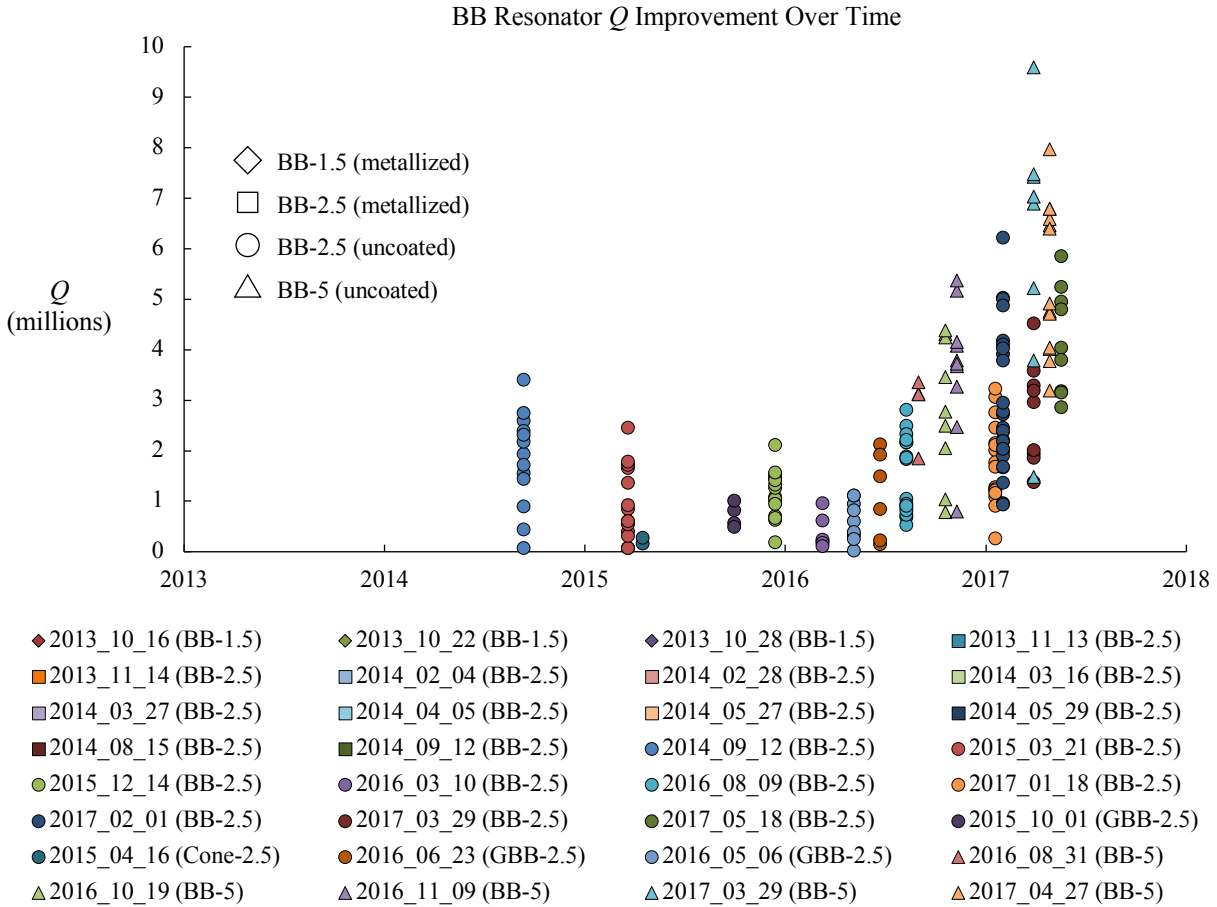
Figure 4.9: Q of the initial metallized resonators never surpassed 1 million. Uncoated resonators initially reached ~3 million, but performance stagnated while fabrication parameters were optimized. Rapid progress was made in 2016 and 2017, with Q approaching 10 million. Each point represents averaged values for both n = 2 WG modes.

The grouping of resonator Qs and frequencies became tighter over time. Improving

graphite mold designs significantly improved batch repeatability; heat flow within the mold was

optimized, greatly reducing erosion of the graphite and increasing the mold life. Optimization of

the isolation process, including identifying a superior mounting thermoplastic and the addition of

a metal barrier layer further improved repeatability in future batches. Figure 4.10 shows the

comparison of Q (a) and τ (b) to the $n = 2$ WG mode frequencies of many batches of uncoated

BB resonators.
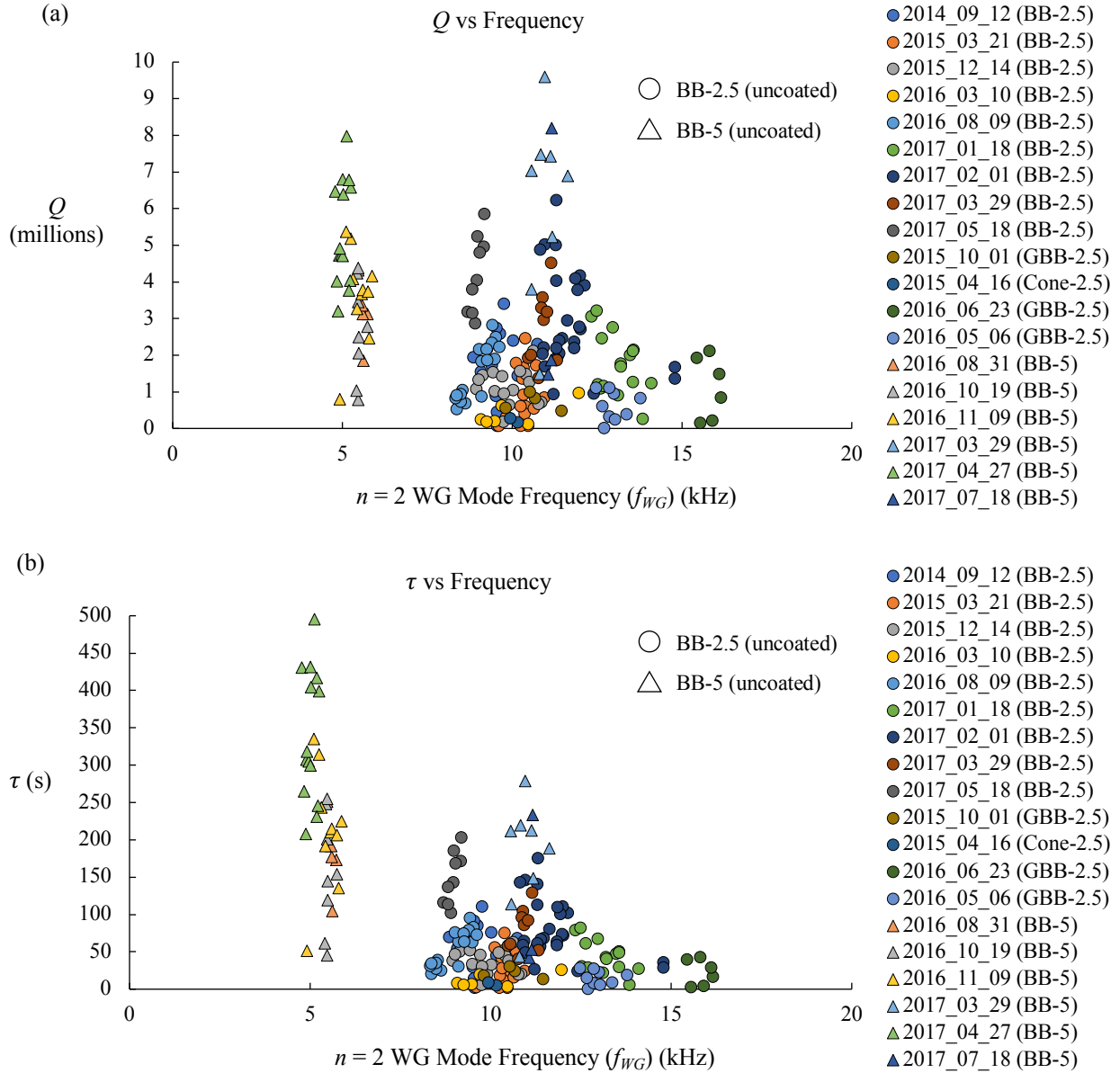
Figure 4.10: Uncoated BB-2.5 and BB-5 resonators can achieve exceptionally high Qs and long τs. As the fabrication process was optimized, batches began to show more tightly grouped performance. Each point represents averaged values for both n = 2 WG modes.

BB-2.5 resonators are fabricated from ~100-μm-thick substrates and generally target 10 kHz, with some variation due to substrate thickness, mold design, and molding depth. The longest τ for a BB-2.5 resonator is 204 s at 9.16 kHz, corresponding to a *Q* of 5.87 million. Its ring-down plot and measured performance are shown in Figure 4.11. If this resonator were packaged as a gyroscope, even if 50% of the *Q* is lost due to conductive layer deposition, the

gyroscope is expected to achieve navigation-grade BI and ARW, with an estimated ARW of ~7.6×10^{-4} °/√hr. The highest Q for a BB-2.5 resonator is 6.24 million at 11.27 kHz. It has a shorter τ of 176 s due to its higher frequency. Its higher frequency and higher Q are due to its greater overall thickness which increases stiffness and decreases S/V ratio; it has a rim thickness of 83 μm compared to 72 μm for the resonator with longer τ.

BB-2.5	WG$_1$	WG$_2$
f (kHz)	9.162	9.209
τ (s)	204	202
Q	5.87	5.84
Δf (Hz)	47.61	
$\Delta(1/\tau)$ (Hz)	4.85 × 10^{-5}	
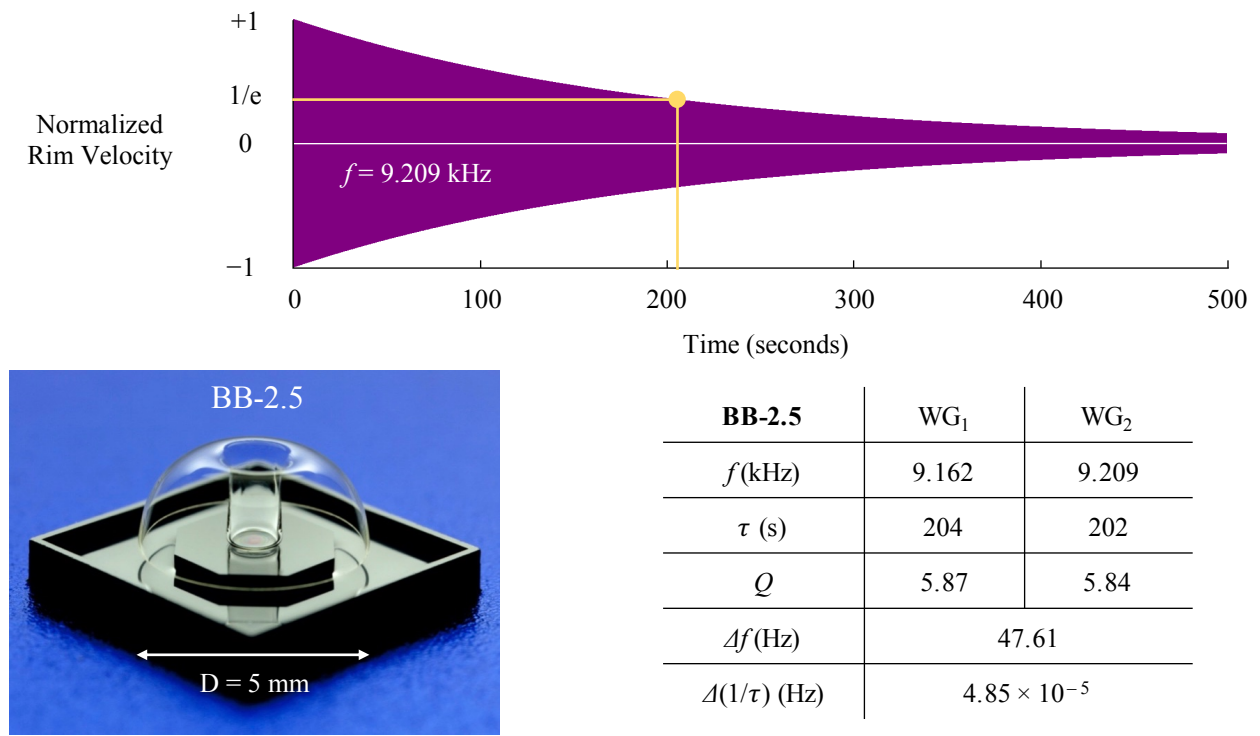
Figure 4.11: Ring-down plot and performance details for the BB-2.5 resonator with the longest τ.

BB-5 resonators are fabricated from either 240-μm-thick or 550-μm-thick FS substrates, leading to f_{WG} of either ~5 kHz or ~10 kHz. The highest τ achieved is 495 s for a 5 kHz BB-5 resonator. Its ring-down plot and performance are shown in Figure 4.12. In addition to long τ, it has an exceptionally low $\Delta(1/\tau)$ of 2.2 μHz and small Δf of 5.74 Hz. The difference between τ_1 and τ_2 for this resonator is only 0.54 s. This performance is truly unprecedented; τ is over an order of magnitude higher than that of similar works. The closest reported value known to us is 23 s for a mm-scale hemispherical resonator produced by Vafanejad and Kim [73]. Even

accounting for loss due to the conductive layer, this resonator is expected to meet or exceed navigation-grade BI and ARW, with an estimated ARW of ~6.5×10^{-4} $°/\sqrt{hr}$. Our highest Q device is a 10 kHz BB-5 resonator that has less surface loss due to its lower S/V ratio. It has similar overall dimensions, but is roughly twice as thick, with a rim thickness of 301 μm compared to 153 μm for the BB-5 with the longest τ. This 10 kHz BB-5 resonator achieves a Q of 9.81 million at 10.96 kHz, and is expected to achieve a low ARW of 5.9×10^{-4} $°/\sqrt{hr}$. Its ring-down plot and performance are shown in Figure 4.13.

BB-5	WG$_1$	WG$_2$
f (kHz)	5.122	5.127
τ (s)	495.5	495.0
Q	7.97	7.97
Δf (Hz)	5.74	
$\Delta(1/\tau)$ (Hz)	2.20×10^{-6}	
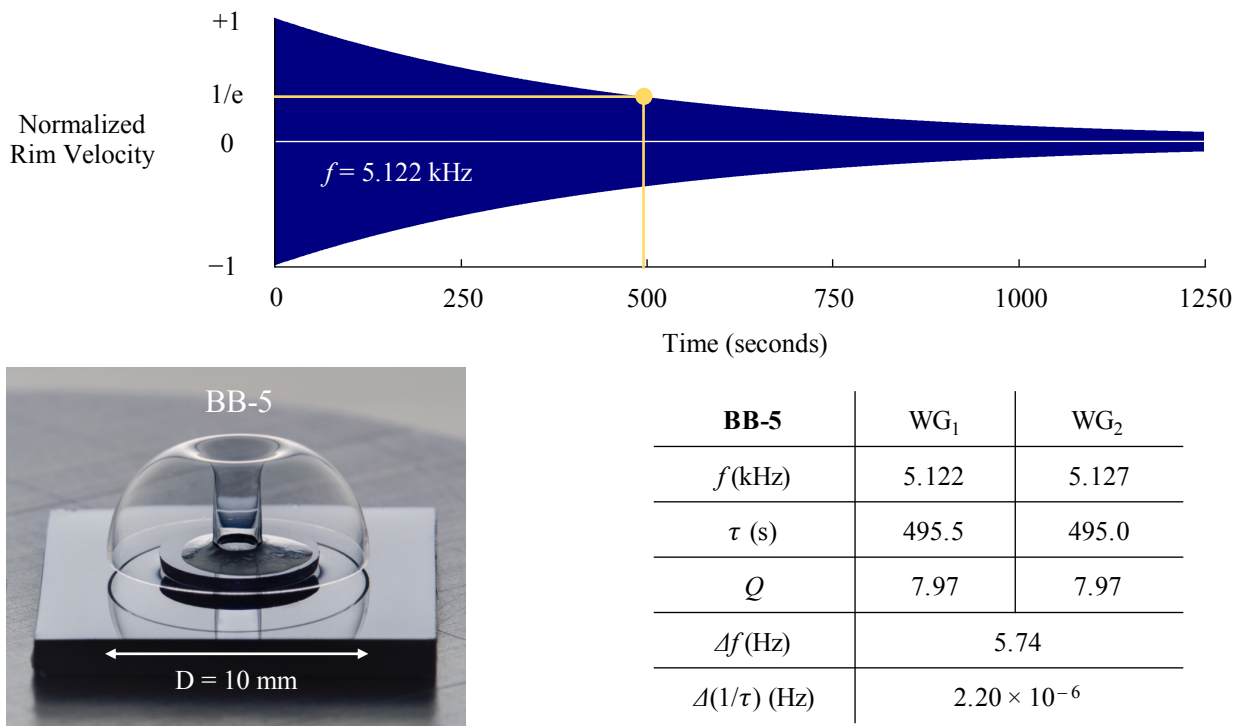
Figure 4.12: Ring-down plot and performance details for the BB-5 resonator with the longest τ.
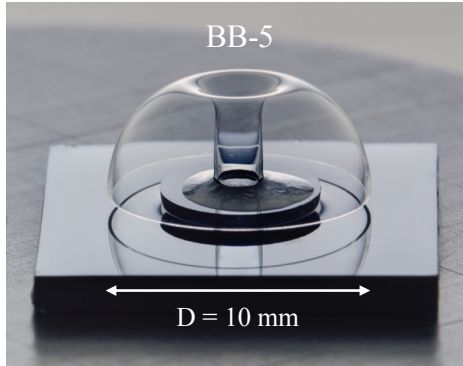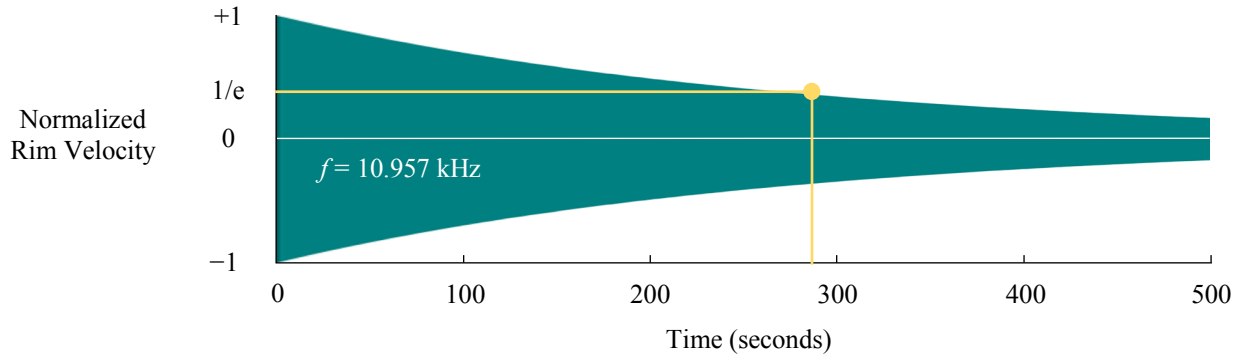
BB-5	WG$_1$	WG$_2$
f (kHz)	10.957	10.967
τ (s)	285.0	272.4
Q	9.81	9.39
Δf (Hz)	10.30	
$\Delta(1/\tau)$ (Hz)	1.62×10^{-4}	

Figure 4.13: Ring-down plot and performance details for the BB-5 resonator with the highest Q.

As with the metallized resonators, there is not a clear dependence of Q on Δf (Figure 4.14). There appears to be a general trend of higher-Q devices having lower Δf, but there are also many low-Q devices with low Δf and several high-Q devices with high Δf. Based on FEM, high Δf is generally caused by fabrication imperfections such a height imbalance or a non-circular shell rim. These types of imperfections increase anchor loss and thermoelastic dissipation, but the measured values of Δf correspond to relatively small imperfections that would not limit Q to the values we have measured. This is discussed in detail in Chapter 6. It is apparent that BB-5 resonators tend to achieve lower Δf than BB-2.5 resonators, with BB-5 typically having $\Delta f < 10$ Hz. As with the higher Δf observed in BB-1.5 resonators compared to BB-2.5 resonators in Section 4.2, the larger size of the BB-5 resonators makes them less susceptible to fabrication imperfections.
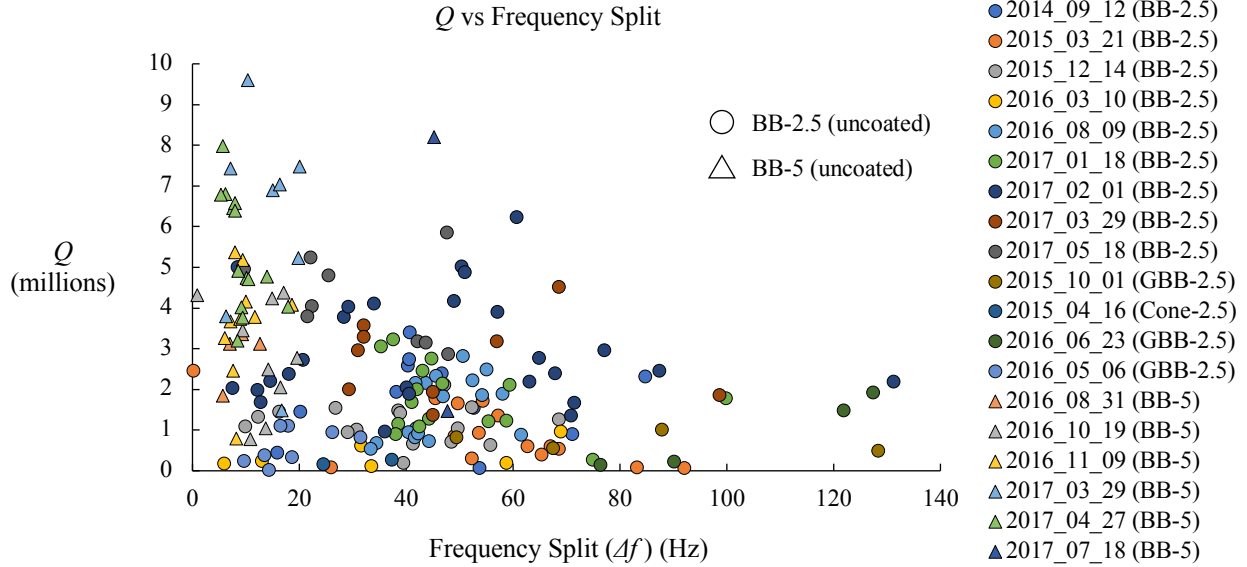
Figure 4.14: There is not a clear dependence of Q on Δf for BB resonators. BB-5 resonators tend to achieve lower Δf due to their larger size and greater tolerance to fabrication imperfections. Each point represents averaged values for both n = 2 WG modes.

The τ vs damping mismatch trend observed for metallized BB-1.5 and BB-2.5 resonators is even more clear with the higher τ and lower $\Delta(1/\tau)$ achieved by uncoated BB-2.5 and BB-5 resonators. BB-5 resonators with f_{WG} of around 5 kHz have achieved impressive performance with τs approaching 500 s and $\Delta(1/\tau)$ reaching down to 2.2 µHz. The BRG electrode integration process has not yet been adapted for this size resonator, but it is expected that such high-performance resonators, even considering a reduction due to conductive layer deposition, will yield navigation-grade MEMS gyroscopes.

As with the metallized resonators, we plot τ_1/τ_2 against $\Delta(1/\tau)$ (Figure 4.16). Again, the higher performance achieved by more recent uncoated resonators creates a clearer trend. For each τ_1/τ_2 value of ~0.9 and below, there are a wide range of damping mismatches that depend on τ, but we do not observe devices reaching below $\Delta(1/\tau)$ of 10^{-4} Hz with more than a 3% difference in τ_1 and τ_2. Two devices reach below 10 µHz. One is the device with the longest measured τ, which has $\Delta(1/\tau)$ of 2.2 µHz, τ_1/τ_2 of 0.999 and τ of ~495 s. The other has $\Delta(1/\tau)$ of 9.16 µHz, τ_1/τ_2 of 0.996 and τ of ~405 s.

84

τ vs. Damping Mismatch

Legend:
- 2014_09_12 (BB-2.5)
- 2015_03_21 (BB-2.5)
- 2015_12_14 (BB-2.5)
- 2016_03_10 (BB-2.5)
- 2016_08_09 (BB-2.5)
- 2017_01_18 (BB-2.5)
- 2017_02_01 (BB-2.5)
- 2017_03_29 (BB-2.5)
- 2017_05_18 (BB-2.5)
- 2015_10_01 (GBB-2.5)
- 2015_04_16 (Cone-2.5)
- 2016_06_23 (GBB-2.5)
- 2016_05_06 (GBB-2.5)
- 2016_08_31 (BB-5)
- 2016_10_19 (BB-5)
- 2016_11_09 (BB-5)
- 2017_03_29 (BB-5)
- 2017_04_27 (BB-5)
- 2017_07_18 (BB-5)

○ BB-2.5 (uncoated)
△ BB-5 (uncoated)
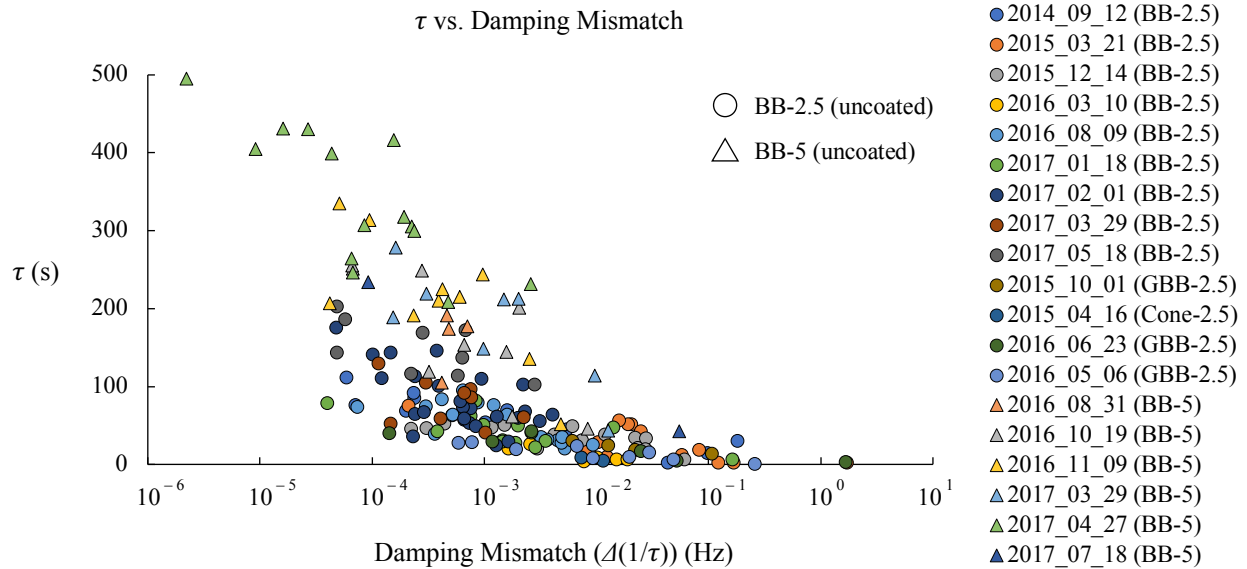
Figure 4.15: There is a clear trend of increasing τ as Δ(1/τ) decreases. There appears to be an upper and lower bound on the relationship between τ and Δ(1/τ). Each point represents averaged τ for both n = 2 WG modes.

τ_1/τ_2 vs. Damping Mismatch

○ BB-2.5 (uncoated)
△ BB-5 (uncoated)
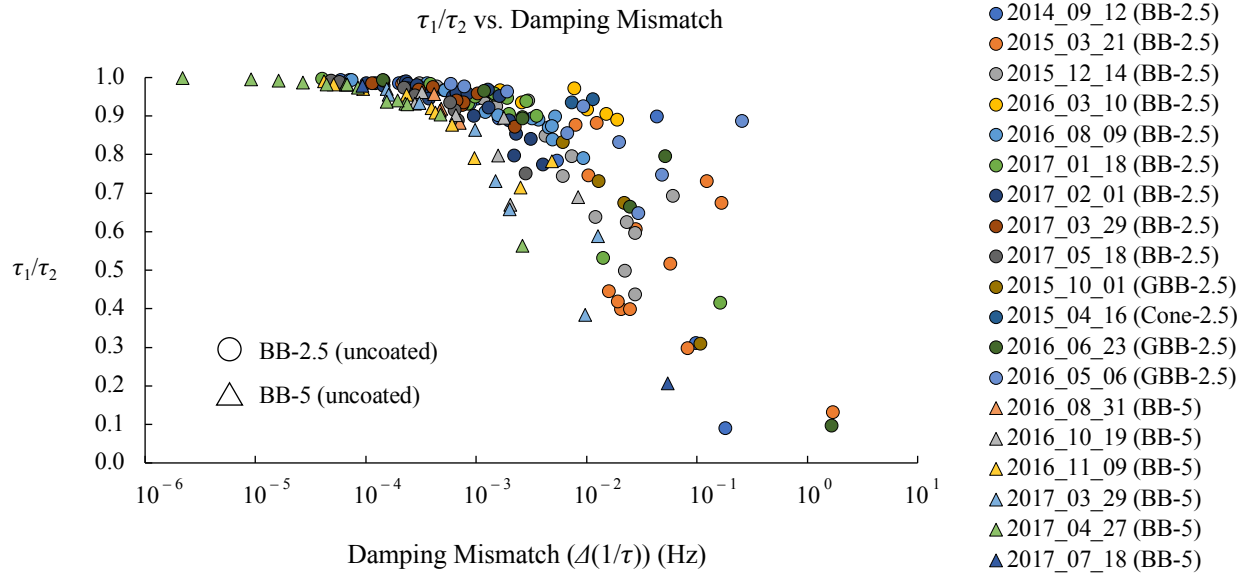
Figure 4.16: Comparing τ_1/τ_2 to Δ(1/τ) reveals how much of the correlation seen in Figure 4.15 is due to the benefit of having a long τ and how much is from τ symmetry. Resonators with the same τ_1/τ_2 but with lower damping mismatch have longer τs.

To examine the theoretical limits of the contributions of τ and τ symmetry on Δ(1/τ), Δ(1/τ) is plotted as a function of τ_2 for a range of τ_1/τ_2 values (Figure 4.17). It is evident that both τ and τ symmetry contribute significantly to Δ(1/τ). For a given τ symmetry, each order of

85

magnitude increase in τ decreases $\Delta(1/\tau)$ by one order of magnitude. τ has improved

considerably over the course of this project, but we believe it is approaching the limit for

resonators of this size and frequency range due to surface loss. As expected, $\Delta(1/\tau)$ is highly

sensitive to τ symmetry. As τ_1/τ_2 approaches unity, $\Delta(1/\tau)$ decreases by about an order of

magnitude from τ_1/τ_2 equals 0.9 to 0.99 to 0.999, etc.
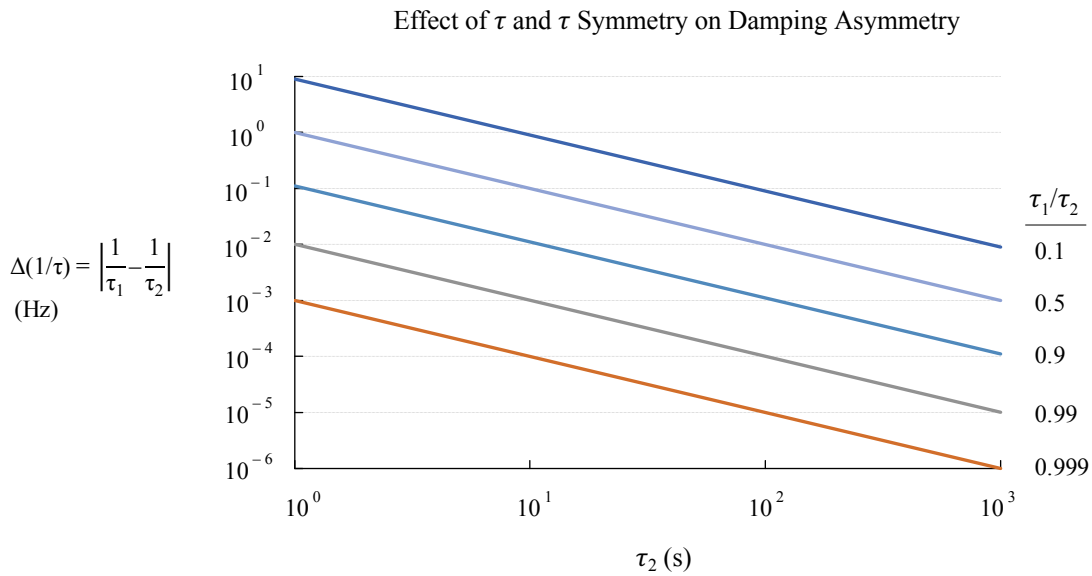
Figure 4.17: *The effect of τ on $\Delta(1/\tau)$ is strongest when τ is less than 100 s. Above 100 s, it is more impactful to increase τ_1/τ_2.*

4.4 Gyroscope Performance

To reach navigation-grade performance, the BRG must achieve a BI of 0.01–0.1 °/hr and

an ARW of $\leq 2\times10^{-3}$ °/$\sqrt{\text{hr}}$. A BRG with electrostatically matched wine-glass modes at 9.058

kHz, τ_1 of 16.98 s, τ_2 of 17.08 s, and $\Delta(1/\tau)$ of 3.45×10^{-4} Hz was tested in the force-to-rebalance

rate mode at room temperature and without temperature control. It achieved BI = 0.0391 °/hr and

ARW = 1.26×10^{-3} °/$\sqrt{\text{hr}}$, which is in the range of navigation-grade performance [74]. The Allan

variance plot for this gyroscope is shown in Figure 4.18. These results are promising, and it is

suspected that the ADC/DAC resolution is the dominant noise source in this measurement, as

preamplifying the signal was found to reduce noise. BB resonators with much higher

performance have since been fabricated. It is anticipated that once they are packaged into gyroscopes, a BRG with beyond navigation-grade performance will be demonstrated.

Allan Variance Plot

Allan Variance (°/hr)

$ARW = 1.26 \times 10^{-3}\ °/\sqrt{hr}$

$BI = 0.0391\ °/hr$

Averaging Time, τ_{Allan} (s)
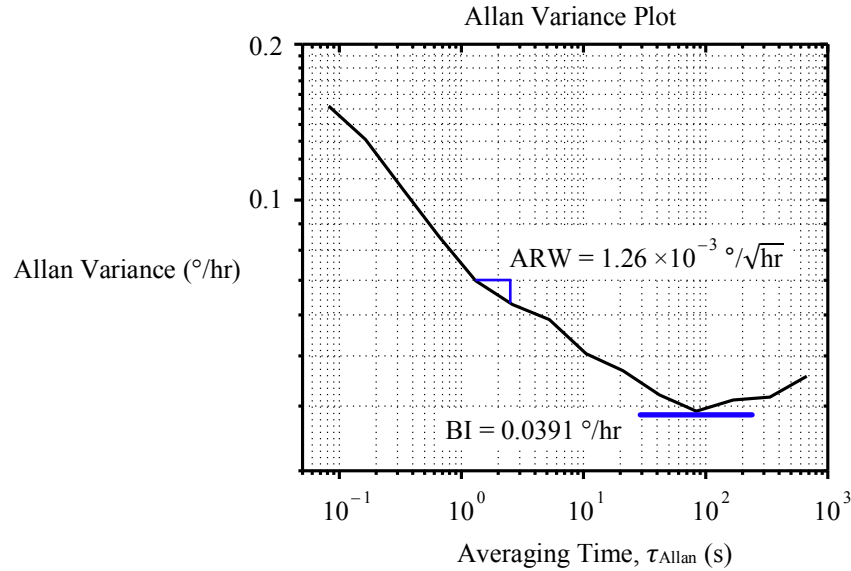
Figure 4.18: Allan variance plot of a BRG with a BB-2.5 resonator having electrostatically matched wine-glass modes at 9.058 kHz, τ_1 of 16.98 s, τ_2 of 17.08 s, and $\Delta(1/\tau)$ of 3.45×10^{-4} Hz. BRG operated in force-to-rebalance rate mode at room temperature without temperature control [74].

4.5 Conclusions

The blowtorch molding process is very flexible. We can easily and effectively control the resonant frequency and S/V ratio of resonators of a given dimension by varying the thickness of the initial bulk FS substrate and the reflow molding depth. Using a mold with a different diameter enables us to keep the frequency low while increasing the S/V ratio to achieve higher values of Q and τ. These changes are easy and inexpensive to make, requiring only the machining of a new mold or purchasing FS wafers of a different thickness. This level of control and flexibility is generally not possible with other fabrication techniques, especially in three dimensions.

After several years of fabrication process optimization, we are producing resonators with previously unheard-of performance at this size and frequency range. To ensure these resonators

will function as navigation-grade gyroscopes, it is critical to maximize their structural symmetry and uniformity, which we have shown is possible. We demonstrated ARW and BI in the navigation-grade range with a BRG having a far poorer performance than many of the BB-2.5 and BB-5 resonators presented in this section. We can therefore conclude that our best resonators, which have values of Q, τ, and $\Delta(1/\tau)$ more than ten times better than that of the resonator tested as a gyroscope, will reach the lower end of navigation-grade BI and ARW.

Chapter 5

Conductive Surface Layer

5.1 Introduction

Fused silica has excellent material properties for a mechanical resonator, but it is a glass and therefore an insulator. To enable electrostatic transduction so the resonator can be operated as a gyroscope, the surface of a FS BB resonator must be coated with a conductive film. This layer must be thick enough to provide a conductive path between the bottom of the stem and the outside of the rim so the shell can be biased at the anchor attachment point; however, due to the sensitivity of BB resonators to their surface condition, even a thin surface layer can significantly reduce Q and τ. Experiments have shown that sputtering only 35 Å of metal on the surface can reduce τ by 40% and that thicker layers reduce it further. There are a number of important considerations including how to bias the shell, what conductive material to use, how to deposit it, and deposition thickness that determine the impact of the conductive layer on resonator performance.

Several different materials have been tested as conductive layers. Noble metals including Au and Pt are tried, as they are resistant to corrosion in air; however, they have poor adhesion to fused silica so an adhesion layer such as Cr or Ti must be deposited first. Devices fabricated in the first year of this research used a variety of Cr/Au or Ti/Au film thicknesses, ranging up to over 1000 Å. The resonator fabrication process and conductive layer had not yet been optimized, so Q remained below 1 million. These early results are summarized in Section 4.2. A conductive

nitride, titanium nitride (TiN), and a conductive oxide, indium tin oxide (ITO), are tried as well. Both of these ceramics adhere to FS and do not require an intermediate adhesion layer. ITO, as an oxide, is expected to be stable in air. TiN is a hard material with excellent chemical resistance that has been used as a semiconductor contact layer as well as a surface passivation layer. Since ITO, TiN, and FS are all ceramics, it is hoped ITO or TiN will form a lower loss interface with FS compared to metals.

This chapter discusses efforts to optimize the conductive layer so energy loss is minimized. The effect of metal layer thickness and metal annealing is discussed. The impact of several different conductive coating materials on Q is shown. With the current techniques, it is not possible to avoid considerable energy dissipation due to the conductive layer, but initial performance is high enough that the resonators should still be able to operate as high-performance gyroscopes.

5.2 Biasing Scheme

Electrostatic transduction requires the BB resonator to be biased to some DC voltage and for the silicon readout-and-control electrodes to be located parallel to the outer shell surface. The resonator can potentially be biased from either side. The two silicon-on-glass electrode integration techniques that have been used are shown in Figure 5.1.

The technique in Figure 5.1(c–d) was used first. The 2-mm-tall electrodes and central silicon post are fabricated with deep reactive ion etching (DRIE). The shell is then assembled to the electrodes using the post as an alignment guide. The shell can either be coated on both sides and biased from a contact on top, or coated only on the outside and biased from a contact on the silicon post. Although the option to coat only one side is attractive for reducing surface loss, this

90

electrode integration technique has poor gap uniformity and relies on an organic polymer that is incompatible with vacuum packaging below 10 mTorr [56].

The technique shown in Figure 5.1(a–b) is the current method for electrode integration. It requires a conductive layer on both sides of the shell so the contact point on the bottom of the stem can bias the outer shell wall nearest the electrodes. Despite the increased surface loss, this technique has the advantage of self-aligned conformal electrodes with uniform ~7 μm gaps and vacuum-compatible materials, making it preferable. Process details are given in [56].
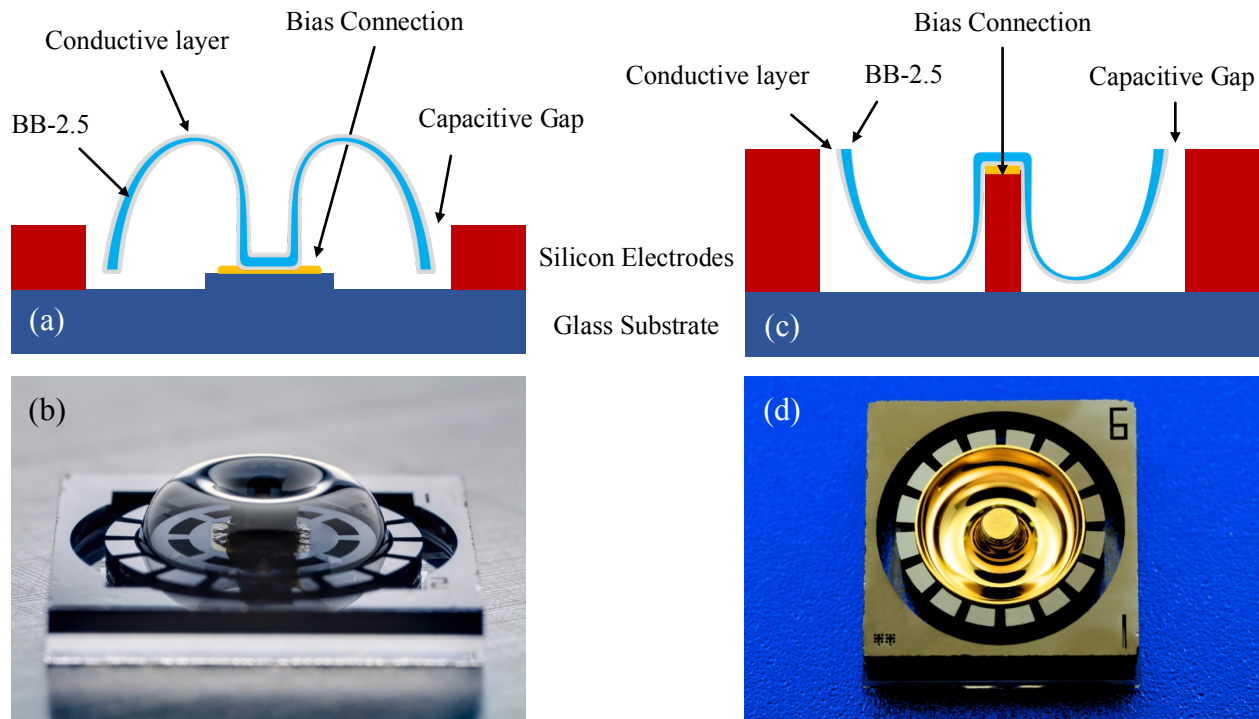
Figure 5.1: Two biasing schemes that have been used for the BRG. (a) requires a conductive layer on both sides but provides automatic alignment and conformal electrodes with uniform gaps. (b) A BRG fabricated using the technique shown in (a) with 15/50 Å Ti/Pt sputtered on each side of the resonator. (c) has poor gap uniformity but only requires metal on one side. (d) A BRG fabricated using the technique in (c) with a sputtered 50/500 Å Cr/Au layer.

5.3 Deposition Technique

The BB resonator needs a conductive path across its entire surface, but its high aspect ratio makes this challenging; the stem and rim regions have over 1 mm of nearly vertical sidewall as well as sharp corners. Sputtering has been used so far because it produces the most

91

conformal film out of all the physical vapor deposition techniques (PVD) available at the Lurie Nanofabrication Facility (LNF) where the BRG is fabricated, but sputtering is still somewhat directional. Chemical vapor deposition (CVD) produces more conformal films, but they are not pure enough to achieve sufficient conductivity at the desired thickness [75].

Considering the inverse relationship between Q and conductive layer thickness discussed in Chapter 5, we want to deposit the minimum amount of material that will produce a continuous path from anchor to rim. It has been experimentally determined that a minimum sputtered thickness of 65 Å is necessary for gyroscope operation; however, this film thickness is based on the deposition rate onto a flat surface, so in reality the only regions of the shell with this thickness are likely the flat area at the bottom of the anchor and the apex of the shell. The angled and vertical regions will have a much thinner layer due both to their angle and shadowing, as depicted in Figure 5.2(a). Therefore, the actual minimum thickness required for gyroscope operation is less than 65 Å, but for sputtering, this thickness must be applied to deposit the actual required thickness in the angled regions.

It is therefore preferable to increase deposition conformality. Atomic layer deposition (ALD) is a promising candidate, as it results in uniform, conformal films with excellent thickness control as fine as 0.1 Å per layer. ALD of Ti, Pt, TiN, and ITO has been demonstrated [76]. Another challenge with PVD is its tendency to form grain structures due to the kinetics of the growth process. This grain structure limits the minimum required thickness to achieve a conductive film, and it has been suggested that slippage between these grains during flexion is a source of energy loss [75]. ALD films are amorphous and do not contain any particulates, eliminating possible energy loss at crystal grain boundaries and resulting in replication of the original surface topology [75]. In a 2014 HRL patent [75] it is suggested that the use of an ALD

metal layer results in higher Q than a PVD metal layer due to both the ability to use a thinner layer and elimination of thickness variation that results in stress gradients when the temperature changes. HRL found that the use of an aluminum oxide (Al_2O_3) adhesion layer under either a Pt or Ru metal layer increases the Q of a fused silica disk resonator by 20% compared to the same resonator with only a Pt or Ru coating. The researchers claim this is due to reduction of interfacial slippage and to surface passivation provided by the Al_2O_3 layer. Unfortunately, due to challenges with the research timeline and difficulty transporting BB resonators to a facility with conductive film ALD capabilities, this has not yet been explored. It is expected that a similar improvement to that seen in the HRL work will be observed for BB resonators.

(a) Sputter deposition   (b) Atomic layer deposition
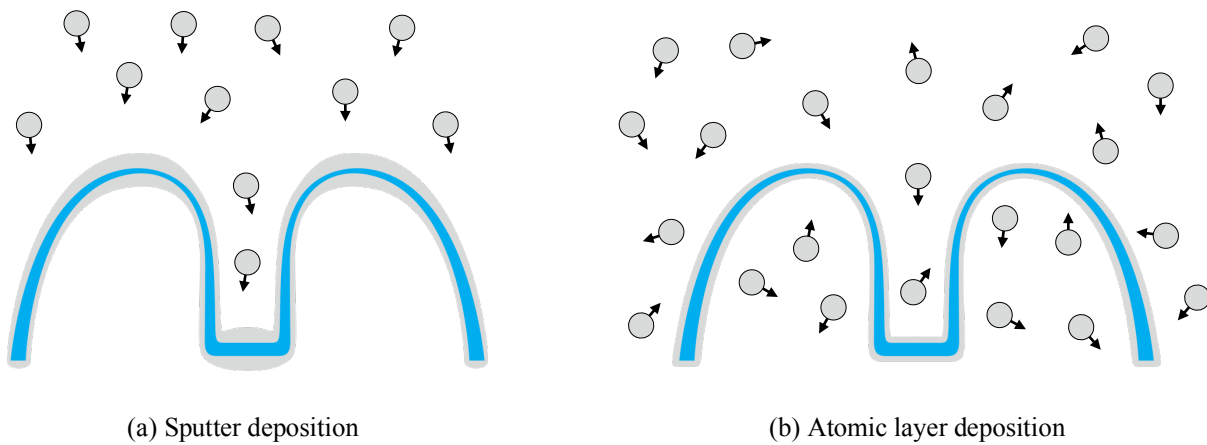
Figure 5.2: (a) Sputter deposition can only coat one side at a time and results in a thickness gradient across the shell due to its directionality. (b) Atomic layer deposition (ALD) is conformal and coats both sides at once with a uniform layer.

5.4 Chromium/Gold

5.4.1 Conductive Layer Thickness

To characterize the effect of metal thickness on performance, the τs of two BB-2.5 resonators are measured before depositing any metal, after sputtering 15/20 Å Cr/Au, and after sputtering three consecutive 40-Å-thick layers of Au on their outer surfaces. Figure 5.3(a) shows the inverse relationship between τ and metal thickness. Notably, there is a large 39% drop in τ

due to the initial deposition of 15/20 Å Cr/Au, but three subsequent 40-Å-thick Au depositions have much less significant effects, reducing τ by 14%, 10%, and finally 7% of its original value. It is surprising to see such a strong effect from the deposition of a layer three orders of magnitude thinner than the resonator itself. This points to the importance of the surface layer condition. A discussion on the nature of this loss is given in Section 6.6.3.

Average surface roughness on the top of the resonator also increases with thickness, then begins to drop, as shown in Figure 5.3(b). A similar increase in roughness of sputtered gold on glass was observed in [77]; the authors found that the roughness plateaued at 7 nm after depositing ~40 nm of Au, but did not observe a decrease like that shown in Figure 5.3(b). The experiments in [77] examined growth of Au directly on glass; it is possible that the presence of a Cr adhesion layer on the BB resonators affects the growth mechanics of the Au film by preventing the degree of islanding they observed in deposition on bare glass.

(a) Effect of Sputtered Cr/Au Thickness on τ (BB-2.5)

(b) Effect of Thickness on Cr/Au Roughness (BB-2.5)
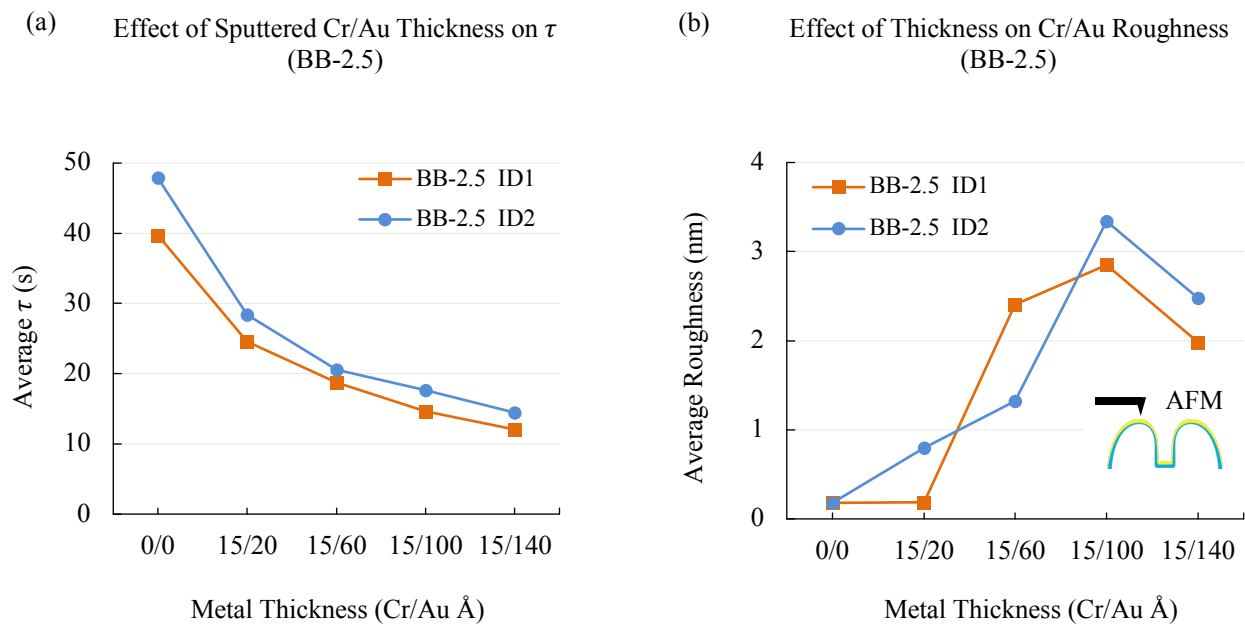
Figure 5.3: (a) Depositing only 35Å of Cr/Au significantly reduces the τ of BB-2.5 resonators. Subsequent 40-Å-thick depositions of Au are not as significant, but continue to reduce τ. Each point is the average of both n = 2 WG modes for one device. (b) Increasing metal thickness tends to increase the average surface roughness over a 10 μm × 10 μm AFM scan, though roughness begins to reduce after depositing 140 Å of Au.

This experiment confirms that it is desirable to use the thinnest possible conductive layer to minimize the negative impact on Q. Other researchers have arrived at the same conclusion for fused silica fibers [78] and stated that they believe conductive Cr coatings of 1 nm thickness or less are possible on their thinner fibers, which are 10 μm in diameter. A sputtered film consisting of a 15-Å-thick adhesion layer of Cr or Ti and a 50-Å-thick conductive layer of Au or Pt has been experimentally found to be the minimum thickness required for electrostatic transduction and gyroscope operation of a BB-2.5 resonator, meaning there is a conductive path between the anchor attachment point and the rim closest to the drive/sense electrodes. This is a limitation of the sputtering technique, as discussed in Section 5.3; it is expected that a thinner layer with lower loss that would still function as a gyroscope could be achieved with ALD.

5.4.2 Chromium/Gold Annealing

Annealing is the process of heating a material to allow the internal stress to relax, then cooling it slowly to prevent formation of new stress. Annealing the conductive layer has been investigated experimentally and found to have mixed effects on resonator τ and Q, but no significant effect on resonant frequency. Recipe parameters are explored to try to minimize the negative effect of metal deposition on Q and to anticipate challenges caused by the elevated temperatures the conductive layer will experience during the packaging process. If Au-Au thermocompression bonding is used to seal the vacuum package, the gyroscope will be heated to 300–400 °C [79]. Two different ovens are used to study the effect of these temperatures. Both are operated at 300 °C in vacuum with a 95/5% N_2/H_2 forming gas atmosphere. The Yield Engineering Systems (YES) oven is operated at 200 Torr and ramped at 2 °C/min. The Angstrom Engineering oven is operated at 100 Torr and ramped at 25 °C/min.

5.4.2.1 Effect of Annealing on τ

Several resonators with a range of initial τs were annealed in the Angstrom Engineering oven for durations ranging from 0–10 minutes, referring to the dwell time once the anneal temperature is reached. These results are shown in Figure 5.4(a). With this oven, the performance of every device suffered. It is suspected that the ramp rate is too fast, and the YES oven is preferred for long annealing runs due to the high cost of the Angstrom engineering oven.

The results were not as clear for devices annealed in the YES oven. Before annealing, the average τ of several initially low-performing BB resonators with 50/15 Å of sputtered Cr/Au is 2.1 s, shown in the lower left corner of Figure 5.4(b). After 2 hours of annealing, the average τ increased to 8.3 s (387% of initial τ) and after a second 2-hour anneal, to 12.8 s (592% of initial τ). Improvements in τ for these initially low-performing resonators range from 2.53–14.68 times, with some devices starting with $\tau \leq 2$ and reaching 18 s. One device with a 15/50 Å sputtered Cr/Au layer showed similar improvement to the other devices annealed for 2 hours. A reduction in τ of initially higher-performing devices from a different batch with 50/15 Å Cr/Au is also observed. The initial average τ of 25.4 s reduces to 8.6 s (34% of initial τ) after 6 hours. Reductions range from 1.85–4.39 times. This change is shown in the lines with negative slopes in Figure 5.4(b).

The only devices whose τs improve with annealing in this experiment are those that are annealed in two-hour intervals in the YES oven. Those annealed for a longer continuous run in the same oven or for shorter times in the Angstrom Engineering oven at the higher ramp rate all experienced reductions in τ. In order to understand the reason for changes in quality factor after metal annealing, several physical aspects of the metal films are characterized before and after annealing. These include film stress, elemental film composition, and surface roughness. The

effect of metal thickness on roughness and τ is also evaluated. The results of these analyses are presented in the following sections.
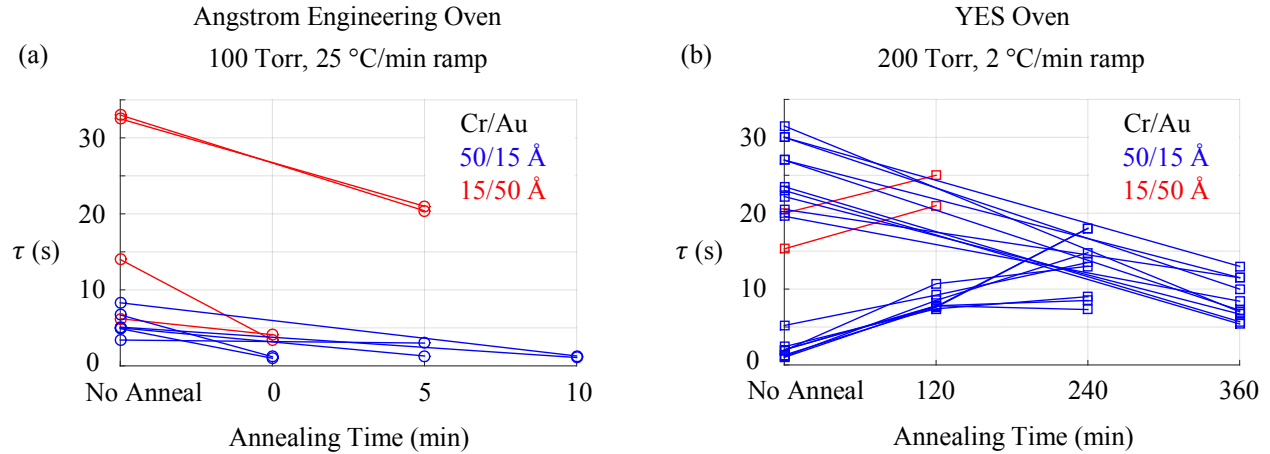
Figure 5.4: Metal annealing at 300 °C in forming gas (95/5% N$_2$/H$_2$) has varied effects on different resonators in different ovens. This result is from 2015, before resonator fabrication was optimized, so the initial τ values are relatively low. Each line represents one WG mode.

5.4.2.2 Effect of Annealing on Film Stress

To understand how annealing affects Cr/Au film stress, 100-Å-thick films in varying Cr to Au ratios are deposited on six ~240-µm-thick FS wafers. The films are annealed at 300 °C in forming gas (95/5% N$_2$/H$_2$) at 100 Torr with a 25 °C/min temperature ramp rate. The substrate interaction stress is measured after annealing for 5, +15, +30, and +60 minutes for a total of 110 minutes. Stress is calculated from wafer curvature measurements on a Dektak XT profilometer. The typical method of laser scanning does not work on bare fused silica because of its high optical transmission. The results are summarized in Figure 5.5.

The measured substrate interaction stress is always tensile. The stress is actually lowest after deposition, with the as-deposited tensile stress increasing with the ratio of Cr to Au. Stress becomes much more tensile after only 5 minutes of annealing. Further annealing reduces stress, and all three film stacks settle around +800 MPa after 110 minutes of annealing. A subsequent 30 minute anneal with a slow (2 °C/min) cool-down does not reduce stress.

The increase in tensile stress of the metal layer is attributed to the formation and growth of intermetallic grains during the annealing process [80]. When the metal layer is first deposited onto the substrate, the atoms are arranged sparsely and the film has the largest effective volume; however, when grains are formed during the annealing step, the volume of the metal layer decreases due to the more compact arrangement of atoms inside the grains. As the grains grow, the metal layer continues to densify and the film exerts increasing levels of tensile stress on the substrate resulting in a change in curvature.
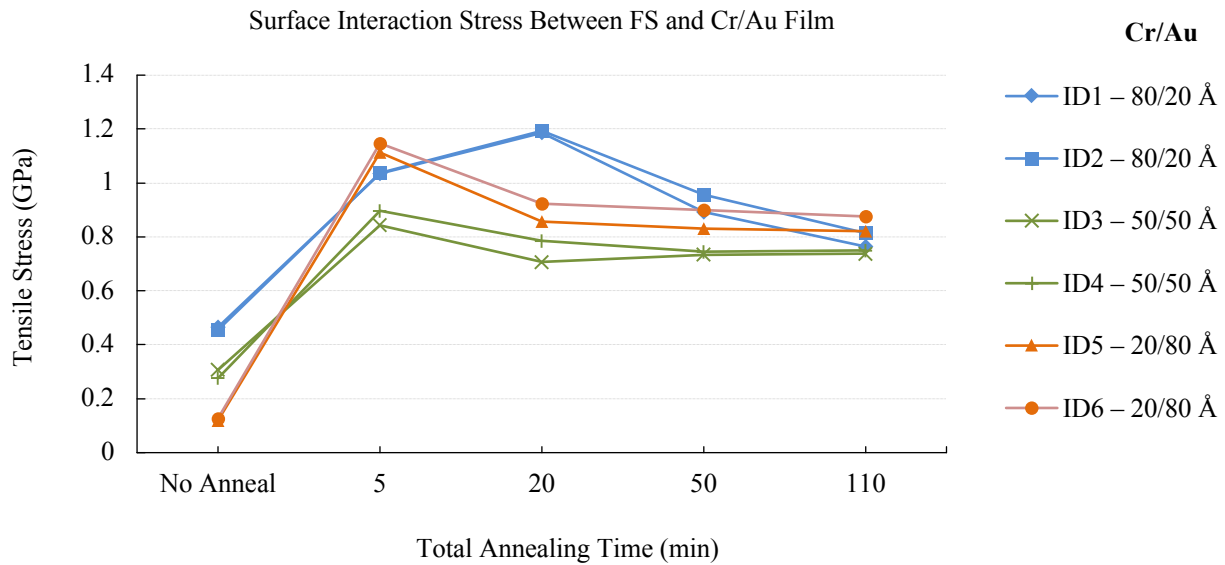
Figure 5.5: Surface interaction stress between 100-μm-thick Cr/Au film stacks with varying compositions and six ~240-μm-thick fused silica wafers for varying anneal times. Annealed in forming gas at 300 °C with 25 °C/min ramp. Stress is calculated from wafer curvature. Each data point is the average of two perpendicular scans. The rapid increase in tensile stress is attributed to the growth of metallic grains.

5.4.2.3 Compositional Analysis

To understand what is happening to the metal films during annealing, the composition of a 50/15 Å Cr/Au film before and after annealing is analyzed with X-ray photoelectron spectroscopy (XPS) [64]. XPS provides surface composition analysis of the top 1–10 monolayers (0.5–5 nm) of a sample. Elements or molecules are identified by the unique energy levels of their photoelectrons that are emitted in response to incident X-rays. A depth-wise compositional

profile of the film is obtained using Ar^+ ions to sputter away the top metal film layer between

XPS scans. The concentration of each element is inferred from the number of electrons counted

per second from each of the selected electron orbitals, 2p for Cr and 4f for Au. The depthwise

compositions of the film before and after annealing are shown in Figure 5.6, where the

composition is normalized to 100% for Cr plus Au. The difference in metal concentrations

throughout the depth is much greater before annealing, suggesting metal diffusion during

annealing. It is known that Cr readily diffuses along Au grain boundaries at 300 °C [81], and

[82] reports that it can even be completely depleted from the substrate interface.
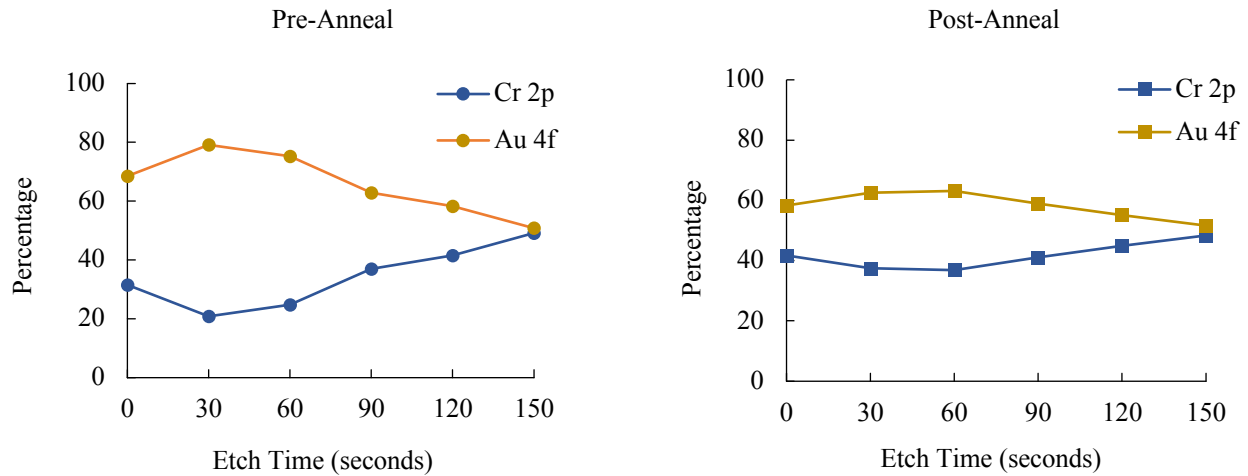
Figure 5.6: XPS analysis of Cr and Au compositions on the surface of a BB resonator. Initial film was 50/15 Å Cr/Au. Data from an elemental peak height report based on the number of counts per second for the 2p and 4f orbitals of Cr and Au, respectively.

It is reported in [82] that a Cr adhesion layer tends to diffuse to the surface of the gold

and form Cr_2O_3. The stacked XPS scan profiles in Figure 5.7 help visualize the concentrations of

Cr and Cr_2O_3 throughout the film depth. Figure 5.7(a–b) show the profile before annealing, while

(c–d) show the profile after annealing. (a) and (c) show the profile stack looking from the top of

the film stack towards the resonator, while (b) and (d) show the view looking from the shell

surface toward the top of the film stack. Both before and after annealing, Cr_2O_3 is detected on the

top surface of the film stack, which is not surprising considering how thin the Au layer is in the

test. Before annealing there is a small Cr peak at the top that appears to absorb into the Cr_2O_3

peak after annealing. The concentration of Cr and Cr_2O_3 increases considerably throughout the

film stack after annealing, confirming the diffusion and oxidation of Cr. It is also possible that Cr

is oxidizing with O_2 from the FS (SiO_2) surface. The film quality change is depicted in Figure

5.8. This is a potential problem, as unregulated growth of oxide in the film could prevent

electrical contact for biasing the shell as well as interfere with gyroscope operation due to

charging.
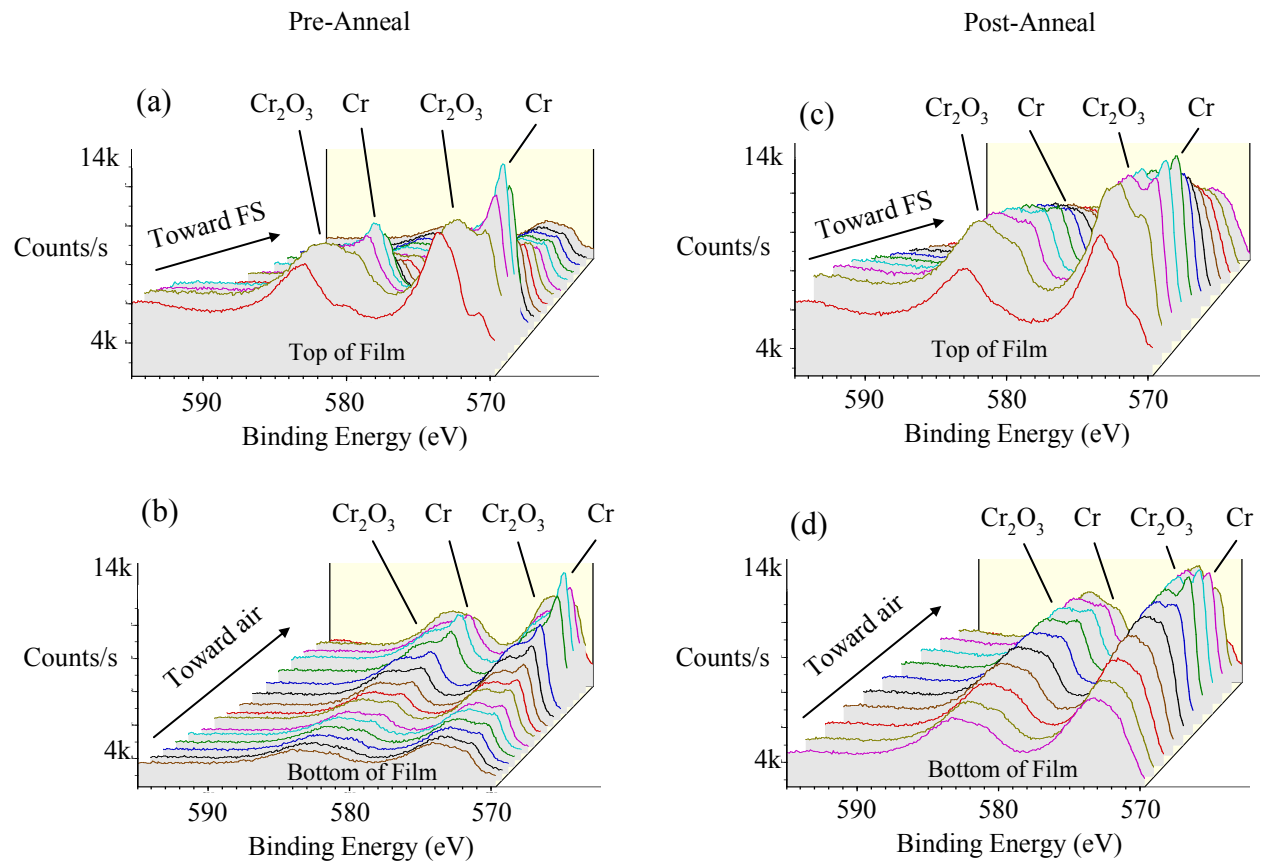
Figure 5.7: Stacked XPS scan profiles of a BB-2.5 resonator with a sputtered 50/15 Å Cr/Au film on the surface. (a) Before annealing, looking from top of film toward FS. (b) Before annealing, looking from bottom of film toward air. (c) After annealing, looking from top of film toward FS. (d) After annealing, looking from bottom of film stack toward air. Cr 2p$_{3/2}$ binding energies are 583.4 eV and 574.1 eV, Cr$_2$O$_3$ 2p$_{3/2}$ binding energies are 586.3 eV and 576.6 eV [83].
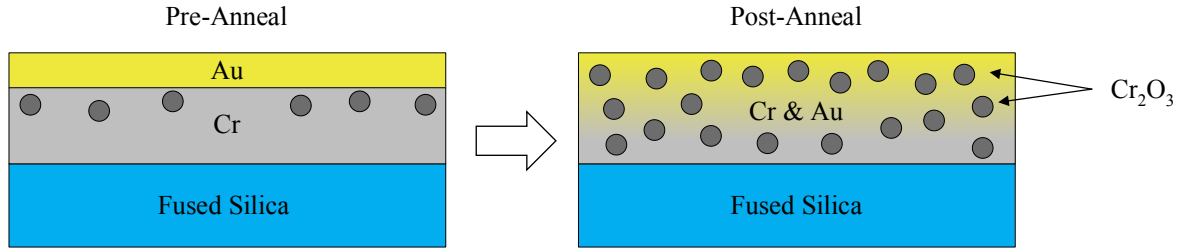
Figure 5.8: Depiction of the state of a Cr/Au film before and after annealing. During annealing, the Cr diffuses along the Au grain boundaries and oxidizes to form Cr_2O_3.

5.4.2.4 Surface Morphology

The blowtorch molding process produces an extremely smooth resonator surface, with average roughness, R_a, of only ~2 Å over a 10 μm × 10 μm scan area. Sputtering metal on top of a bare shell increases the average roughness by ~1.2× for Cr/Au 15/50 Å and by ~1.1× for Cr/Au 50/15 Å. After annealing for 30 minutes, average roughness increases by ~6.5× for Cr/Au 15/50 Å and by ~5.3× for Cr/Au 50/15 Å compared to the uncoated shells. These results are summarized in Table 5.1.

Table 5.1: Summary of surface roughness measured for BB-2.5 resonators before metal deposition, with sputtered Cr/Au film stacks, and after annealing the metal films. Average (R_a) and RMS (R_q) roughness are calculated over a 10 μm × 10 μm area.

Sample Condition	Sample 1: Cr/Au 15/50 Å		Sample 2: Cr/Au 50/15 Å	
	R_a (nm)	R_q (nm)	R_a (nm)	R_q (nm)
Uncoated	0.189	0.237	0.180	0.229
Metal	0.226	0.294	0.201	0.265
Annealed	1.23	1.55	0.958	1.21

Figure 5.9 shows atomic force micrographs of two resonator surfaces before depositing metal, after sputtering 15/50 Å or 50/15 Å Cr/Au, and after annealing for 30 minutes at 300 °C. The anneal is performed at 100 Torr in forming gas with a temperature ramp rate of 25 °C/min. The deposition of metal creates a dense array of sharp peaks that grow into large, smooth

hillocks after annealing. The increase in roughness and formation of hillocks in the metal film are attributed to the growth of Cr and Au metal grains, which are known to grow at 300 °C within Cr/Au films [81].
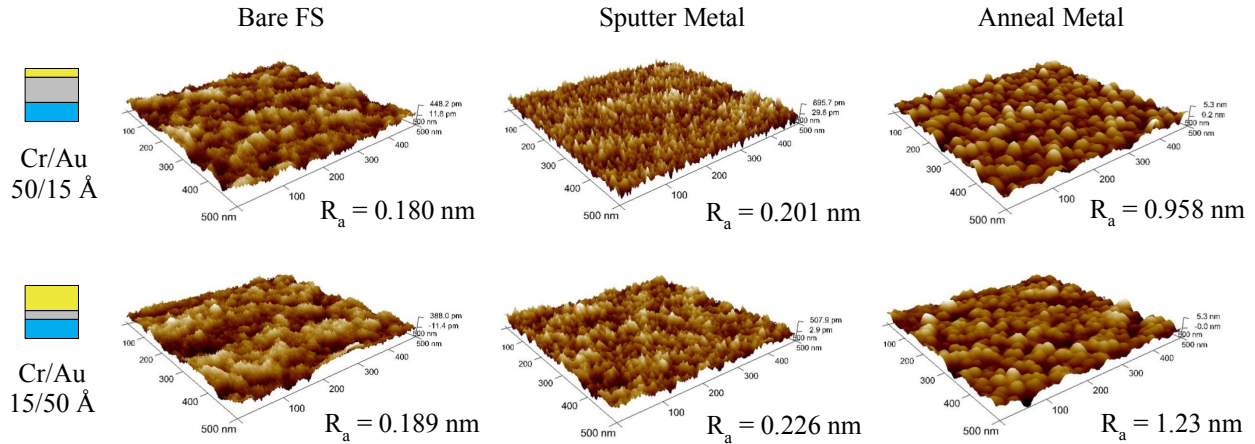
Figure 5.9: Average roughness measured with AFM scans over a 10 μm × 10 μm area on an uncoated BB-2.5 resonator, after sputtering metal, and after annealing the metal at 300 °C in forming gas. The formation of hillocks is attributed to metallic grain growth during annealing.

This grain growth may have several effects. It has been observed that Cr diffuses not only along Au grain boundaries, but also into Au grains, causing an increase in resistivity by 25% after 2 hours at 300 °C [81]. Formation of voids in a Cr adhesion layer was also reported due to preferential diffusion of Cr into Au without fully compensated diffusion of Au into Cr. The creation of voids in the Cr layer increases the likelihood of Cr corrosion and reduces the amount of corrosion required to lose adhesion [84]. This may increase friction loss due to interfacial slippage. Another concern is the potential for increased energy dissipation at the grain boundaries. An HRL patent about quartz disk resonator gyroscopes suggests that slippage between metal grains due to bending of the resonator is a relevant source of energy loss [75]. [85] explains that energy is stored at metallic grain boundaries due to the pile up of dislocations and that energy dissipation occurs when dislocations are transferred between boundaries. If annealing causes the formation of new grain boundaries, they could be a source of increased

energy dissipation; however, for longer annealing times the grains will continue to grow, reducing the total grain boundary area, which should reduce this type of loss.

5.4.3 Discussion on Cr/Au Film

A gold conductive layer over a chromium adhesion layer is commonly used for microsystem contacts. In most cases, the device is not as sensitive to surface effects as the BB resonator. Here, we must holistically consider this film stack, including the structure of the film upon deposition and how it may change when heated. Although very common, sputtering is not the best technique for depositing the conductive layer in this case. Its non-conformality results in thickness and stress gradients across the resonator, and due to the inherent growth mechanics of sputtering, metallic grains will form during deposition. Annealing will cause these grains to grow and exert stress on the substrate. Although there is no clear mechanism by which stress affects τ, it is clearly affected by baking at 300 °C. Experiments have shown both increases and decreases in τ of several BB resonators, where short anneals with a higher temperature ramp rate always cause a decrease and longer anneals with a slow ramp rate have mixed results.

The apparently conflicting effect of annealing on τ between different batches of resonators under different conditions cannot be readily explained by a single mechanism and is likely the result of multiple mechanisms that have opposing effects. The primary purpose of annealing is to relax stress. It has been shown that asymmetric stress can reduce Q as a result of laser trimming [86], but there is no clear mechanism by which blanket stress in a surface film should increase energy dissipation. Annealing also causes the formation and growth of metal grains whose boundaries may be a source of energy dissipation. The reduction in total grain boundary area due to metal grain growth during a long anneal is one potential benefit, but in general, annealing a Cr/Au film will cause structural and electrical changes that degrade BB

103

resonator performance. It seems likely then, that the positive changes observed in some resonators are due to improvements in the resonator itself rather than the metal film. These positive effects occur more slowly than the negative effects, causing resonators baked in the Angstrom Engineering oven to see only the negative effects. This may be explained by the rapid formation of new grain boundaries during a short anneal.

We have observed that uncoated BB resonators that undergo a vacuum bake-out under the same conditions of the above metal annealing show considerably improved Q and τ that is attributed to the removal of adsorbed species from their surfaces (Section 6.6.2). It is reasonable to conclude that this positive effect opposes the negative effects of metal annealing, especially considering that none of the resonators discussed in this section were baked prior to metal deposition. If we consider that BB resonators will in general all tend towards similar performance, that the variation in performance observed in the past is due to varying surface conditions following the fabrication process, and that that optimal performance can be reached by cleaning the surface with a vacuum bake-out in forming gas, it makes sense that resonators with initially lower performance stand to improve more from bake-out than those with initially higher performance. Therefore, if a Cr/Au film is to be used as the conductive layer, the shell should undergo vacuum bake-out first, then be coated with metal, and finally be packaged with the lowest possible thermal budget.

5.5 Titanium/Platinum

Due to the challenges associated with Cr/Au films, Ti/Pt is investigated as an alternative. Contrary to Cr/Au films, the electrical resistivity (ρ) of Ti/Pt films has been found to decrease following annealing at 300 °C. It is suggested that this is due to relaxation of intrinsic film stress that occurs at this temperature. Resistivity is shown to increase above the as-deposited values

beginning at annealing temperatures around 450 °C and to continue to increase for higher temperatures up to 700 °C [87]. Film roughness has been shown to remain unchanged at 300 °C, with a tendency to decrease slightly at 450 °C, but then to increase with temperature in the 600–800 °C range [87]–[89]. The authors found that the metallic grain size remains unchanged at 300 °C or in some cases shrinks. This suggests that a Ti/Pt film stack should be more stable in the 300–400 °C temperature range required for gyroscope packaging.

As with Cr/Au it is found that 65 Å of Ti/Pt is sufficient for electrostatic actuation. It is expected that a sputtered metal layer will have less of an effect on BB-5 than BB-2.5 resonators due to the lower S/V ratio of BB-5 resonators, but it is experimentally determined that the impact is similar on both sizes. Figure 5.10 shows the large initial impact of depositing a 10/20 Å Ti/Pt film on two 5 kHz BB-5 resonators, which lowers τ of both of them to 0.54× their original values, τ_0. Adding another 40 Å of Pt lowers τ to ~0.46·τ_0. The samples are then annealed two times for two hours each in the YES oven at 300 °C in forming gas with a 2 °C/min ramp rate. The first anneal increases τ to ~0.49·τ_0, but the second time only increases   to ~0.50·τ_0. The resonators are then left in the LDV vacuum chamber at around 1 µTorr and tested again after 11 and 15 days. After 15 days, τ has considerably improved for both resonators, reaching ~0.60·τ_0. After several months of sitting in vacuum storage (around 200 Torr), the shells are annealed again, this time at 420 °C and for 18 hours. This had a minor effect, bringing them to ~0.61·τ_0. After 12 days in vacuum at ~1 µTorr, device 1 improves further to ~0.62·τ_0.

The improvements after deposition are attributed to the removal of adsorbed substances from the resonator surface, including water. This is discussed in Section 6.6.2. Based on these experiments, Ti/Pt is stable at the elevated temperatures required to package the BRG, making it a better choice than Cr/Au; however, it still causes a reduction of at least ~40% of τ_0 in order to

sputter a sufficiently conductive film. Still, even with this large reduction, device 1 from Figure

5.10 is expected to achieve navigation-grade BI and ARW, with an estimated ARW of 6.9×10^{-4}

$°/\sqrt{hr}$.
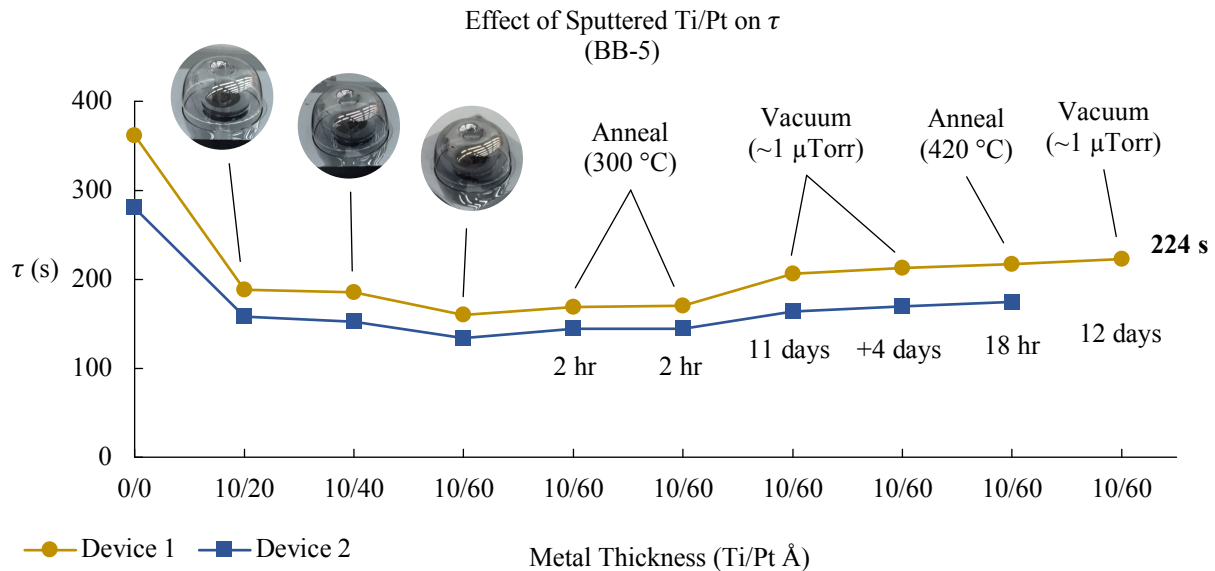
Figure 5.10: Depositing only 30 Å of Ti/Pt significantly reduces the τ of BB-5 resonators. Subsequent 20-Å-thick depositions of Au are not as significant but continue to reduce τ. The resonator can be seen to darken with increasing deposition thickness. After repeated anneals and leaving the resonator under vacuum for extended lengths of time, the performance recovers to 62% of its original value. Each point represents the averaged values of both n = 2 WG modes for a given device as measured with LDV.

5.6 Titanium Nitride

Titanium nitride (TiN) is widely used in a number of industries, including space, biomedical, machining, and microelectronics. It is a gold-colored ceramic with many advantageous material properties, including high hardness, resistance to corrosion, high conductivity, biocompatibility, and excellent thermal and chemical stability [90]. Although it has seen use in the microelectronics industry as a diffusion barrier [91], adhesion layer [92], and contact layer [93], we have seen few examples of use as a conductive layer for resonators. Notably, [94] presented thermally grown SiO_2 hemispherical shell resonators coated with 30 nm of ALD TiN.

TiN can be deposited in the LNF with reactive sputtering by flowing N_2 during Ti sputtering. Resistivity can be quite low with this technique, with as-deposited values below 100 $\mu\Omega$-cm that can be reduced to below 50 $\mu\Omega$-cm after annealing at 900 °C for 1–20 minutes [93]. The reduction in resistivity is attributed to a reduction in grain boundary area due to grain growth that reduces the number of scattered conducting electrons. The improvements did not show a time-dependence, suggesting this change happens within one minute at 900 °C.

Sputtered TiN film properties depend heavily on the deposition parameters. A study investigating the electrical properties of reactively sputtered TiN films concluded that optimal conditions for depositing a low-ρ film include a substrate temperature above 200 °C and gas pressure below 4 mTorr. $Ar:N_2$ flow ratios ranging from 4:1 to 2:3 all produced films with low ρ [95]. [96] looked at the effect of Ar flow on several TiN film properties. The researchers found that a higher proportion of Ar to N_2 flow increases ρ and hardness, but decreases elastic modulus. They also found that higher Ar flow increases crystalline grain size and decreases dislocation density. Other researchers have also reported an increase in ρ as the proportion of Ar to N_2 increases [93], [95]. The authors of [93] attribute the reduction in ρ for high N_2 content to a transition toward [200] crystallographic orientation at 95% N_2 compared to the predominantly [111] orientation with 20% N_2 flow that creates a smoother surface and reduces electron scattering.

Reactive TiN sputtering was not previously characterized in the LNF. To determine the optimal gas composition for achieving a low-ρ film with our Lab 18 sputtering tool, TiN is deposited with mixtures of 10, 30, 50, and 70% N_2 onto both a glass slide and a Si wafer with 5000 Å SiO_2. These test substrates are chosen to enable both transmission and reflection ellipsometry measurements, increasing the confidence of the measured material properties. All

depositions were performed for 1000 s at 400 W at 10 mTorr. The results are summarized in Figure 5.11. They confirm the observation in [93] of lower roughness at higher N_2 concentrations.

Effect of % N_2 on Sputtered TiN Deposition Rate and Roughness
400 W, 10 mTorr, Lab 18-1
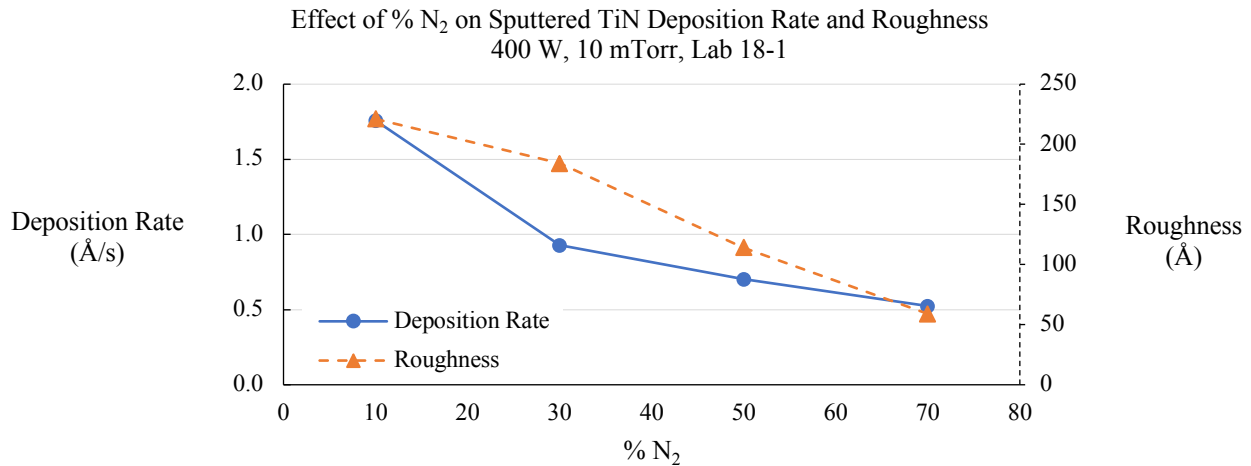
Figure 5.11: Deposition rate and film roughness for reactively sputtered TiN at various percentages of $N_2 / (N_2 + Ar)$ gas flow during DC sputtering. Measurements taken on an ellipsometer.

ρ is measured before and after annealing at 450 °C with a four-point probe on the films deposited on glass slides. The results are summarized in Table 5.2. A sputtered 15/50 Å Ti/Pt film, which is known to have sufficient conductivity for gyroscope operation, is measured for comparison. The TiN deposition recipe in the LNF clearly needs additional development, as the the measured values of ρ are several orders of magnitude higher than those reported in literature. One key difference is that the substrate was not heated during these depositions, whereas it was heated to 250 °C in [93] and 70 °C in [96]. [95] reported the effect of different substrate temperatures ranging from 40–300 °C. The authors found similar low values of ρ for 200 °C and 300 °C, but 10× higher ρ for a 100 °C substrate. They do not report the ρ of films deposited on 40 °C substrates. Heating the substrate was not possible during the depositions performed in the LNF due to the method by which the resonators were mounted to the carrier wafer. It is suspected that this is the primary reason for the measured high ρ.

Six BB-2.5 resonators with initially high Qs are coated with TiN, two resonators with each of the three compositions. The resonators are all baked out at 450 °C in forming gas for 8 hours before depositing the TiN films. After TiN deposition, the Qs of all six devices tend toward around 2 million, with no clear relationship to N_2 concentration during sputtering (Figure 5.12). Rather, they all decrease to 40–50% of their uncoated Q (Q_0). This is similar to the effect of sputtering 15/60 Å Cr/Au on BB-2.5 resonators (~47% of Q_0) and 10/60 Å of Ti/Pt on BB-5 resonators (46% of Q_0).

Table 5.2: Electrical resistivity of TiN films taken with a four-point probe. All TiN samples were sputtered for 1000 s on a glass slide with Ar and N_2. A thin sputtered Ti/Pt film that has been reliably used for gyroscope operation was measured with the same technique for comparison. After annealing at 450 °C in forming gas for 2 hours, the Ti/Pt resistivity decreases slightly while that of TiN increases above the measurable range.

Film	% N_2	Thickness (Å)	Resistivity ($\Omega \cdot$cm)	Annealed Resistivity ($\Omega \cdot$cm)
TiN	10%	1758	16.8	Open circuit
	30%	927.8	203	Open circuit
	50%	702.6	Open circuit	Open circuit
	70%	524	Open circuit	Open circuit
Ti/Pt	N/A	15/50	3.7×10^{-3}	2.5×10^{-3}
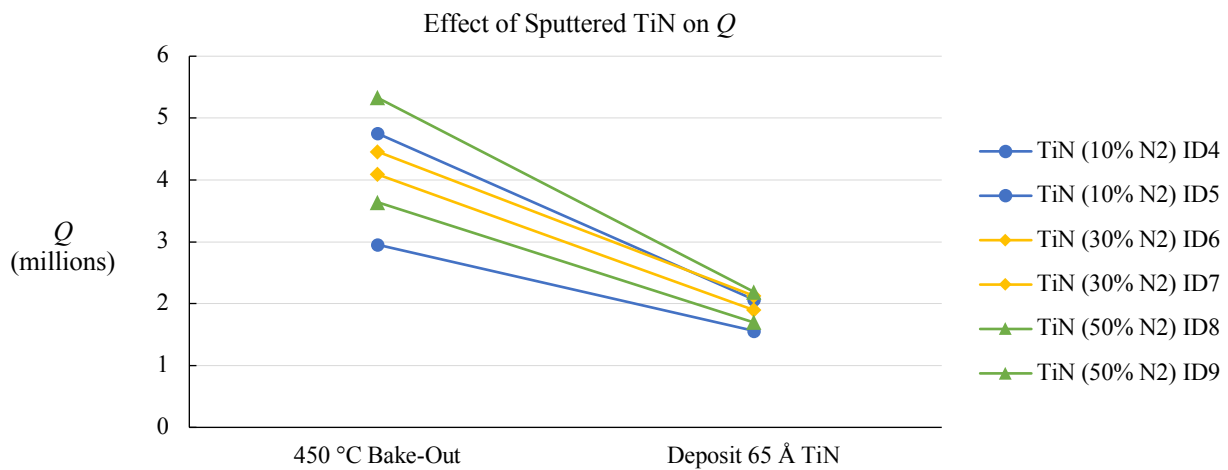
Figure 5.12: Sputtering 65 Å of TiN onto six BB-2.5 resonators results in a reduction in Q of 50–60% for all of them. There is no clear relationship to the N_2 to Ar composition during sputtering. Each data point represents the averaged values of both n = 2 WG modes for a given device as measured with LDV.

TiN reduces Q by a similar percentage as comparable thicknesses of Cr/Au and Ti/Pt. If we achieved lower resistivities similar to the published values, 65 Å would be sufficient for a sputtered film; however, since the measured resistivities are so high, a much thicker film would be required to enable gyroscope operation with our current TiN depositions, which would further reduce Q. If ρ could be reduced, TiN would be a good option compared to the metallic films we have previously used. It has the benefits of high hardness, surface passivation, and chemical and thermal stability. Indeed, [93] showed a reduction in ρ during 900 °C annealing, which is the annealing range for FS as well. TiN would certainly stand up to any high temperature steps encountered during packaging.

Although TiN significantly reduces Q, because of the initially high Qs of these devices they still achieve long ring-down times and high Qs. ID8 has $f = 8.96$ kHz, $\tau = 78.9$ s, $Q = 2.22$ million, $\Delta f = 22.0$ Hz, and $\Delta(1/\tau) = 3.64 \times 10^{-4}$ Hz. This is the best performance for a coated BB-2.5 resonator to date. Packaged as a gyroscope, this resonator is expected to expected to achieve navigation-grade BI and ARW, with an estimated ARW of 8.8×10^{-4} °/$\sqrt{\text{hr}}$.

5.7 Indium Tin Oxide

Indium tin oxide (ITO) is a transparent conductive oxide that is widely used in display and solar technologies to enable electrical routing without interfering with light transmission, though we have not found evidence of its use as a conductive layer for electrostatic actuation of mechanical resonators. It is considered for BB resonators because it is a stable conductive oxide with low ρ that can be deposited in the LNF with sputtering. It is hoped that the interface between two oxides, FS and ITO, will have less loss than between FS and metal or TiN.

To determine ρ and the impact of film annealing, a 500-Å-thick ITO film is sputtered onto a glass slide. ρ is measured with a four-point probe immediately after deposition and again

after annealing at 450 °C for two hours in forming gas. ρ reduces significantly from 1.76 Ω·cm

to 4.4×10^{-2} Ω·cm following annealing, unlike the Ti/Pt film that reduces slightly and the TiN

film that increases considerably. These results are summarized in Table 5.3. The optical

transmittance also increases considerably, as shown in Figure 5.13.

Table 5.3: Electrical resistivity of sputtered ITO, Ti/Pt, and *10% N_2 TiN films taken with a four-point probe. The Ti/Pt film has been reliably used for gyroscope operation. After annealing at 450 °C in forming gas for 2 hours, the ITO resistivity decreases by almost two orders of magnitude.

Film	Thickness (Å)	Resistivity (Ω·cm)	Annealed Resistivity (Ω·cm)
ITO	500	1.76	4.4×10^{-2}
Ti/Pt	15/50	3.7×10^{-3}	2.5×10^{-3}
TiN*	1758	16.8	Open circuit

500 Å ITO Sputtered on Glass Slide

As deposited   2 hour 450 °C anneal
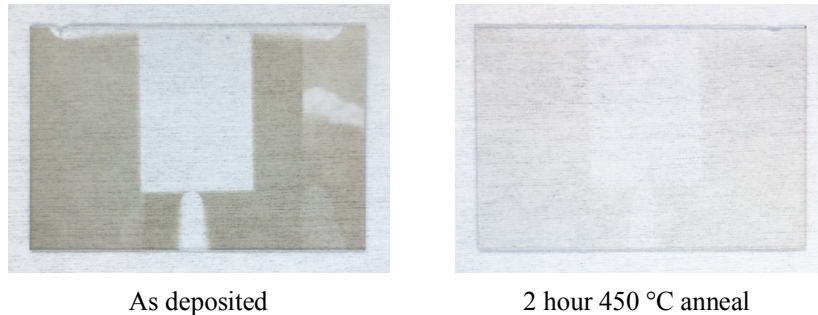
Figure 5.13: The optical transmission of a 500-Å-thick sputtered ITO film increases significantly after annealing for 2 hours in forming gas at 450 °C. This is accompanied by a reduction in resistivity by almost two orders of magnitude.

Similar results have been observed in literature. [97] demonstrated a 30–40% increase in

transmittance of 300–1100 nm light after annealing in forming gas at 300 °C. Interestingly, they

found a decrease in transmittance from the as-deposited state when annealing in forming gas at

400 °C, which is contrary to our observation after annealing at 450 °C. The substrates were at

room temperature in both cases, but the films were deposited with e-beam evaporation in [97],

while the samples in this research were sputtered. The observations presented in [98] for ITO

sputtered at room temperature are more aligned with ours; they found an increase in

transmittance at 200 °C that improved as temperature increased to 500 °C during vacuum annealing.

Of more relevance to this research is the observed decrease in ρ. [98] found that ρ of ITO films sputtered onto a 250 °C substrate decreases slightly when they are annealed at 300–500 °C; however, ρ of films deposited onto a room temperature substrate decreases from 9×10^{-4} $\Omega \cdot$cm to ~2×10^{-4} $\Omega \cdot$cm when annealed above 200 °C. [97] notes that the reducing reaction caused by hydrogen in the forming gas can improve the electrical conductivity of sputtered ITO films. Forming gas causes a reduction-oxidation reaction, reducing the concentration of oxide in the film. This increases the concentration of oxygen vacancies which are one of the electrical carriers in ITO.

Initial measurements of a BB-2.5 resonator sputtered with 65 Å of ITO are promising. The average Q of the 11.3 kHz $n = 2$ WG modes reduced to $0.69 \cdot Q_0$, where Q_0 was 3.31 million. This is the smallest reduction observed throughout this research for any sputtered film of this thickness, and the final Q is higher than any of the TiN-coated resonators. This result was measured recently, and further investigation is necessary to draw a conclusion about the efficacy of ITO as the conductive layer for BB resonators. It is expected that further process optimization will further reduce ρ of our sputtered ITO, but even with the current values this film is expected to provide sufficient conductivity for gyroscope operation. ALD deposition of ITO should further reduce loss by enabling application of a thinner, conformal layer.

5.8 Conclusion

It is clear that BB resonators are highly sensitive to the deposition of thin films on their surfaces, as evidenced by the ~45% reduction in Q caused by only 30 Å of Ti/Pt on a ~150-μm-thick BB-5 shell. It is interesting to note that Q tends to reduce by a percentage of its initial value

rather than to an absolute value. This has been observed for resonators of different sizes with a range of initial Qs and τs. Both 10 kHz BB-2.5 and 5 kHz BB-5 resonators are observed to lose 50–60% of their initial Q due to the deposition of a ~65-Å-thick conductive layer, which we have determined is the minimum thickness for a sputtered conductive layer required for gyroscope operation.

A likely explanation for the source of this loss is interfacial slippage between the FS and conductive layer [99]–[101]. The two materials will invariably have different Young's moduli, so flexion of the shell induces a jump in stress across the interface that converts mechanical energy into thermal energy, which dissipates irreversibly. This matches our observations that the presence of even a very thin layer with a different Young's modulus would cause a large increase in energy dissipation, and that as the layer thickness increases, more stress would be generated and therefore more energy would be dissipated. This theory suggests that dissipation at the interface can be mitigated by depositing a film with a Young's modulus as close as possible to that of FS. This theory is discussed further in Section 6.6.3.

Chapter 6

Energy Loss Mechanisms

6.1 Introduction

A primary goal of this research it to maximize the ring-down time, τ, and quality factor, Q, of birdbath resonators in order to reduce birdbath resonator gyroscope drift. This is inherently challenging at the micro-scale, as the small size and low mass of micro-resonators limits the amount of energy they can store and increases their susceptibility to damping mechanisms. They are especially sensitive to surface effects due to the increase in surface-to-volume (S/V) ratio as linear dimensions decrease. This is a critical barrier that must be overcome to create MEMS gyroscopes with navigation-grade performance, which so far has only been commercially achieved with macro-scale gyroscopes. The relevant energy loss mechanisms for the birdbath resonator include fluidic damping, thermoelastic dissipation, anchor loss, intrinsic loss, and surface loss, each of which will be discussed in this chapter. Each plays a role in the total measured Q, and each could potentially become dominant under certain conditions. Their relationship to the measured Q is given by

$$\frac{1}{Q} = \frac{1}{Q_{fluidic}} + \frac{1}{Q_{TED}} + \frac{1}{Q_{anchor}} + \frac{1}{Q_{intrinsic}} + \frac{1}{Q_{surface}} \qquad (6.1)$$

6.2 Fluidic Damping

Fluidic damping refers to the loss of kinetic energy from an oscillating resonator due to the interaction between its surfaces and the surrounding fluid, typically air. This type of damping

tends to dominate the Q of MEMS resonators at atmospheric pressure. As the resonator moves it generates tangential (shear) and normal (pressure) forces that act on the surrounding air.

Slide damping, or Couette damping, occurs when air moves parallel to a surface. This commonly occurs when two parallel planes slide past each other, such as the fingers of a comb drive (Figure 6.1(a)). This causes a gradient in air flow velocities, as the air nearest each surface moves at nearly the same velocity as that surface. A difference in velocity between the surfaces and surrounding air generates friction that is dissipated as heat into the adjacent walls [102].

(a) Comb Capacitor   (b) Parallel Plate Capacitor
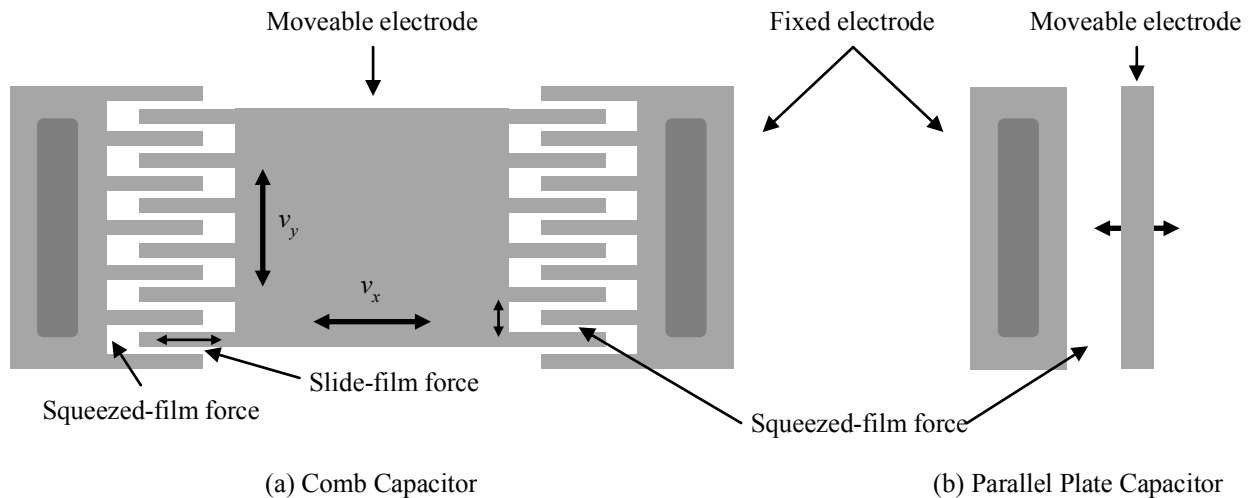
Figure 6.1: Depiction of fluidic damping forces that act on MEMS resonators. When a comb capacitor (a) moves in the x direction it is subject to slide damping on the sides of the tines and squeeze damping at the ends. In the y direction, it has squeeze damping as the fingers approach each other. The parallel plate capacitor (b) has large squeeze damping as gap closes.

Normal force causes both Couette and squeeze damping when two parallel plates move toward and away from each other. When the plates approach each other, some air between them is squeezed out to the sides and some is squeezed between the plates. As they move away, air is drawn back in to fill the expanding gap. The air motion parallel to the plates generates Couette damping, while the air that is squeezed between them causes squeezed-film damping. This occurs with comb drives, when the ends of the moving comb fingers approach the back of the receiving comb or when the fingers move laterally toward each other, and with parallel plate

capacitors as the plates approach each other. This is illustrated in Figure 6.1. The local air

compression translates kinetic energy into heat due to increased friction in the surrounding gas;

this kinetic energy is irreversibly lost when the heat dissipates into the surrounding walls [102].

This is a concern for the BRG, as it has a large surface area facing its drive and sense electrodes.

Even for a standalone BB resonator without any nearby surfaces, the normal force pushes and

pulls on the surrounding air, impeding its motion and dissipating kinetic energy as friction

through acoustic radiation [103].
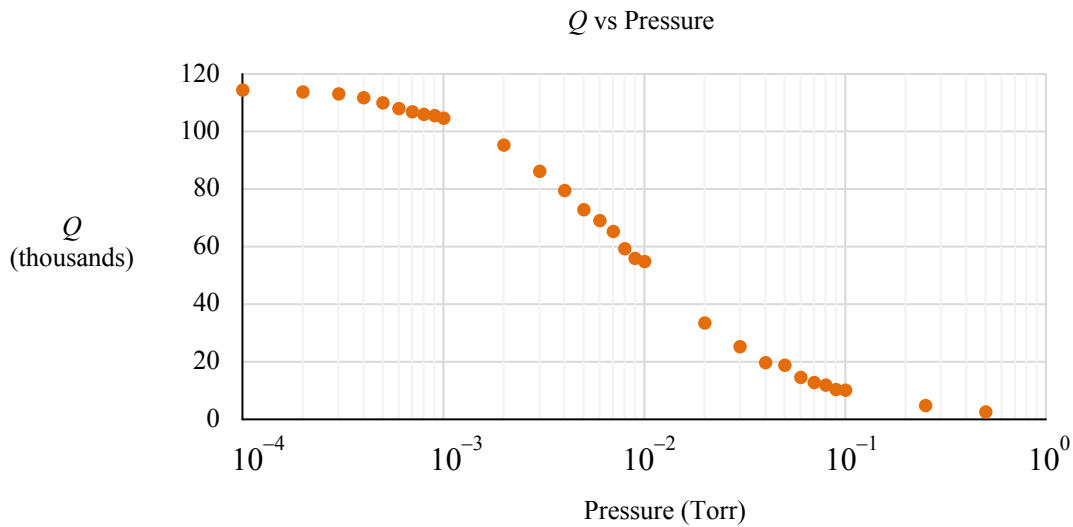
Figure 6.2: Pressure has a strong effect on Q due to fluidic damping. Below 1 mTorr and above 100 mTorr Q is relatively stable, but between these regions, Q is sensitive to pressure. Data provided by Mr. Christopher Boyd.

Fortunately, fluidic damping can be eliminated by reducing the air pressure. At

atmospheric pressure, the mean free path (l_{MFP}) between air molecules is ~65 nm [102], meaning

that a resonator displacing by several microns will interact with many air molecules. Operating

in a vacuum of 1 mTorr increases l_{MFP} to ~4.4 cm, and reducing pressure to 1 μTorr increases

l_{MFP} to ~43 m [104]. These long mean free paths drastically reduce the number of air molecules

the resonator interacts with, increasing $Q_{fluidic}$. The effect of pressure on Q of a packaged BRG,

as measured by Mr. Christopher Boyd, is shown in Figure 6.2. These results indicate that fluidic

116

damping is greatly reduced in the mTorr range, and all but eliminated at 100 µTorr. Testing is typically carried out below 10 µTorr, so it is safe to say fluidic damping is not the dominant energy loss mechanism for BB resonators.

6.3 Thermoelastic Dissipation

When a material undergoes strain, regions under compression become warmer while regions under tension become cooler. If a horizontal beam is bent downwards, a thermal gradient will be generated with the bottom being warmer than the top. Heat immediately begins to flow upwards to the cooler region until the beam reaches thermal equilibrium. If the beam bends back upwards, the thermal gradient reverses and heat begins to flow in the opposite direction. This occurs during each oscillation period for a resonating cantilever. Generation of this temperature gradient consumes vibrational energy, and as the temperature equalizes, that energy is lost. This process is known as thermoelastic dissipation (TED).

In 1937, Clarence Zener published a model [105], [106] for calculating the TED-limited Q (Q_{TED}) of cantilever beams, which can be written in terms of the material properties and beam geometry as

$$Q_{TED} = \frac{\rho\, C_{SP}}{E\, \alpha^2\, T_0} \frac{1 + (\omega_{mech} \cdot \tau_{th})^2}{\omega_{mech} \cdot \tau_{th}} \tag{6.2}$$

where ρ is material density, C_{SP} is specific heat capacity, E is Young's modulus, α is the coefficient of thermal expansion, T_0 is average temperature, ω_{mech} is the angular resonant frequency (equal to $2\pi f$), and τ_{th} is the thermal transport time constant, given as

$$\tau_{th} = \frac{b^2}{\pi^2 D} \tag{6.3}$$

where b is beam thickness in the bending direction and D is thermal diffusivity [61]. Due to this relationship, a cantilever beam will have a minimum Q_{TED} when $\omega_{mech} \cdot \tau_{th} = 1$, i.e., the thermal

relaxation time equals the period of oscillation. The frequency at which this minimum occurs shifts depending on the beam thickness, as shown for fused silica in Figure 6.3, courtesy of Mr. Ali Darvishian. A BB resonator can be thought of as a revolved cantilever beam, so this same basic analysis applies.
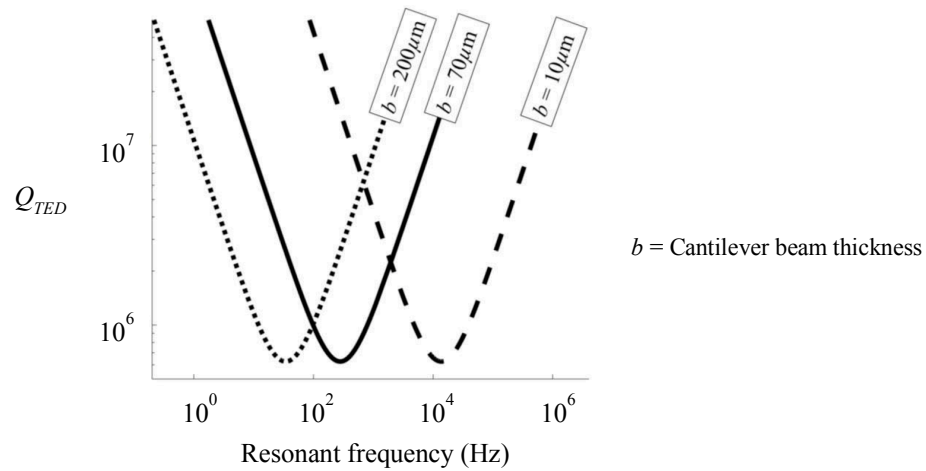
Figure 6.3: A minimum value of Q_{TED} occurs at different frequencies for cantilever beam resonators of different thicknesses. The data shown here are for fused silica beams. Reprinted from [61] with permission from Mr. Ali Darvishian.

One of the reasons behind selecting FS as the resonator material is its inherently low TED. In [61], Ali Darvishian calculated the expected Q_{TED} of BB resonators made from a number of different materials. He concluded that FS and Zerodur, a low-α glass, are the best options from the TED standpoint. These results and the material properties used in the calculations are shown in Table 6.1. Notably, FS and Zerodur have low E, k, and α compared to other materials, where k is thermal conductivity. Although Zerodur actually appears to be a better option, there are other important properties to consider, such as intrinsic loss. Both of these materials were under consideration for use as the mirrors for gravitational wave detectors, but it was concluded that FS has an intrinsic quality factor ($Q_{intrinsic}$) hundreds of times higher than that of Zerodur [107], and FS was ultimately chosen for the mirrors and suspension fibers for gravitational wave detectors.

118

Table 6.1: FEM comparison of Q_{TED} of 10 kHz BB resonators if they were made from different materials. Calculations of quality factor, Q, are based on their material properties: Young's modulus (E), Poisson's ratio (v), density (ρ), thermal conductivity (k), coefficient of thermal expansion (α), and heat capacity (C_{SP}). Reprinted from [61] with permission from Mr. Ali Darvishian.

Material*	E (GPa)	v	ρ (kg/m³)	k (W/(m·K))	α ($10^{-6} \times 1/K$)	C_{SP} (J/(kg·K))	Q (FEM)	Q (Analytical model)
SiO₂	70	0.17	2200	1.4	0.5	730	7.5 x10⁷	7.9 x10⁷
Zerodur	90.3	0.24	2530	1.46	0.02**	820	4.6 x10¹⁰	5.9 x10¹⁰
Al₂O₃	400	0.22	3965	35	6.5	730	1.7 x10⁴	1.8 x10⁴
SiC(6H)	748	0.45	3216	490	4.3	690	8.2 x10³	6.5 x10³
Si₃N₄	250	0.23	3100	20	2.3	700	1.8 x10⁵	2.0 x10⁵
Borosilicate	63	0.2	2230	1.13	3.3	754	2.0 x10⁶	2.5 x10⁶
GaAs	85.9	0.31	5316	33	5.7	550	5.2 x10⁴	5.2 x10⁴
Ge	103	0.26	5323	58	5.9	310	2.1 x10⁴	1.5 x10⁴
InSb	409	0.35	5770	18	5.4	200	5.7 x10³	6.8 x10³
C[100]	1050	0.1	3515	990	0.8	520	3.3 x10⁵	1.8 x10⁵
Si(c)	170	0.28	2329	130	2.6	700	6.7 x10⁴	4.7 x10⁴

Silicon has historically been the choice material for MEMS gyroscopes, but silicon resonators in the desirable frequency and size range tend to be limited by TED [62], [108]. Based on FEM, a 10 kHz BB-2.5 resonator has a Q_{TED} of 75×10^6, which is almost an order of magnitude higher than the maximum Q measured experimentally. Even the addition of a thin metal layer with poor TED is not expected to have a major impact on overall Q_{TED}. To confirm this, the relationship between metal layer thickness and the Q_{TED} of a BB resonator is calculated using the finite element method with COMSOL Multiphysics by Dr. Behrouz Shiari. The resonator is modeled with a gold layer of uniform thickness covering the entire surface. The simulation shows that Q_{TED} increases from 0.99 million to 12.6 million as the thickness of the metal layer decreases from 1 μm to 100 nm [109]. Further reduction in the modeled metal thickness has not been possible due to difficulty creating a model in COMSOL; creating a continuous mesh between a 6-nm-thick layer and an ~80-μm-thick BB-2.5 shell has been very challenging with the computational resources available. The trend of Q_{TED} increasing with reduction in metal layer thickness is due to the smaller amount of heat generated in the metal layer during expansion and contraction as the resonator vibrates, reducing dissipation. Our BB resonator has a metal coating layer with thickness < 10 nm but exhibits much lower Q than the

simulated Q_{TED} for a 100-nm-thick Au layer. Thus, we believe that TED in the film is not the dominant energy loss mechanism.

While TED is not expected to limit the performance of an ideal shell, it is important to consider the effect of fabrication imperfections on Q_{TED}, particularly height and circularity imperfections. A height imperfection (Figure 6.4(a)) is defined as the difference in height between two sides of the shell divided by the nominal height; this can occur if the mold is not centered under the torch, causing a non-uniform heat distribution. A circularity imperfection (Figure 6.4(b)) is defined as the difference in outer radius between two sides of the shell divided by the nominal radius; this can occur if the outer mold wall is not perfectly circular or if the mold temperature distribution is non-uniform. Dr. Behrouz Shiari carried out simulations to examine the effects of these defects on a BB-2.5 resonator simulated to have nominal $f_{WG\,1,\,2} = 13.156$ kHz and $Q_{TED\,1,\,2} = 46.62$ million.
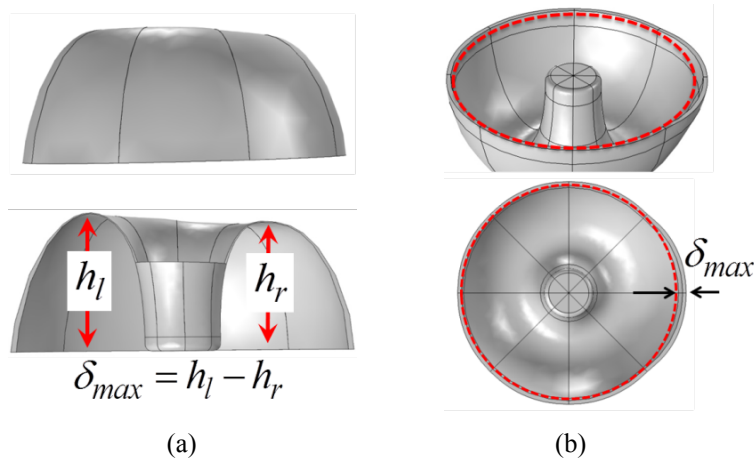
Figure 6.4: FEM of a shell with a height (a) and circularity (b) imperfection. These models are created by applying a local force to deform the shell, then saving the deformed geometry as a new shape. Figures provided by Dr. Behrouz Shiari.

Figure 6.5 shows the simulated effect of height and circularity imperfections on the Q_{TED} of both WG modes and the resulting $\Delta(1/\tau)$. A 7% height imperfection results in an average reduction in Q_{TED} of 26% and a 13% difference between the two modes, which translates to a

$\Delta(1/\tau)$ of 2.0×10^{-4} Hz. Figure 6.7(b) shows an extreme example of a BB-2.5 resonator fabricated with a 20% height imperfection, caused by an intentional misalignment of the torch and mold. The resonator shown in Figure 6.7(a) is typical, with no detectable height imperfection. A 5% circularity imperfection results in an average reduction in Q_{TED} of 20% for one mode while the other is essentially unchanged, giving a $\Delta(1/\tau)$ of 1.9×10^{-4} Hz.
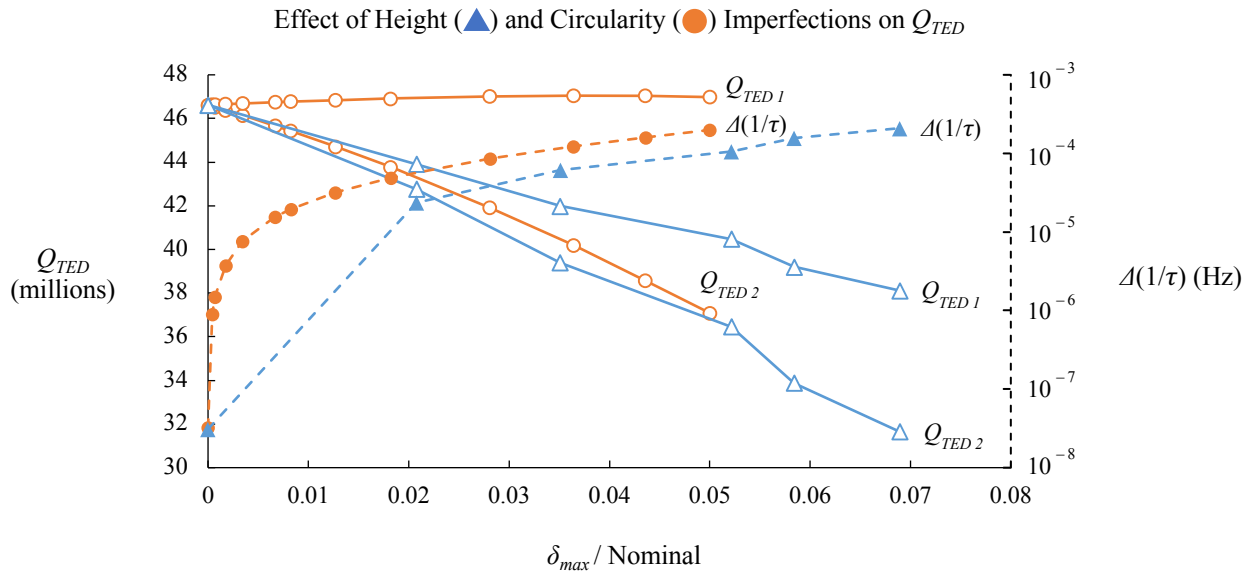
Figure 6.5: Effect of height and circularity imperfections on Q_{TED} of each n = 2 WG mode and the resulting $\Delta(1/\tau)$.

Figure 6.6 shows simulated effect of height and circularity imperfections on the frequency (f_{WG}) of each WG mode and the resulting Δf. A 7% height imperfection results in an average reduction in f_{WG} of ~3% and a 0.5% difference between frequencies, which translates to a Δf of 66 Hz. A 5% circularity imperfection results in an average reduction in f_{WG} of ~2% and a 3% difference between frequencies, translating to a large Δf of 401 Hz. Circularity imperfection clearly results in a larger bifurcation in frequency than height imperfection, which is concerning due to the challenge of mode matching a resonator with a large Δf. To look for circularity imperfections in fabricated resonators, circles are superimposed onto photos of their rims when they are still encapsulated in the lapping jig wafer, as shown in Figure 6.7(c). Fortunately,

measureable levels of circularity imperfection have not been observed and Δf rarely exceeds 40 Hz, suggesting that the extent to which this defect exists in fabricated resonators is quite small and therefore does not significantly effect Q_{TED}.
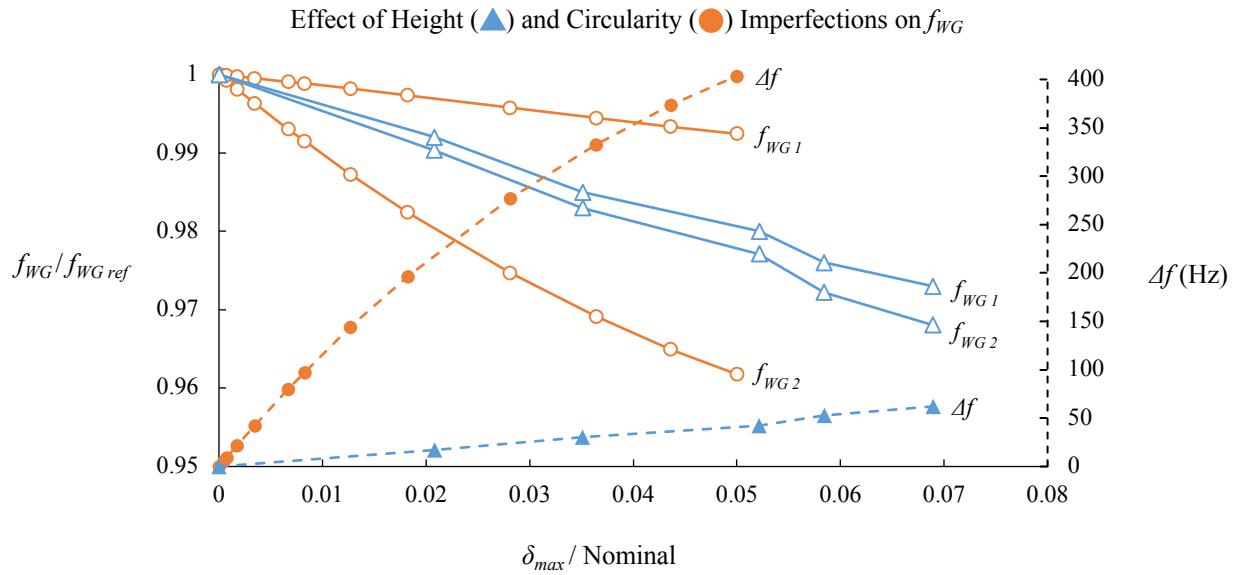
Figure 6.6: Effect of height and circularity imperfections on the n = 2 WG mode frequencies and frequency split, Δf.
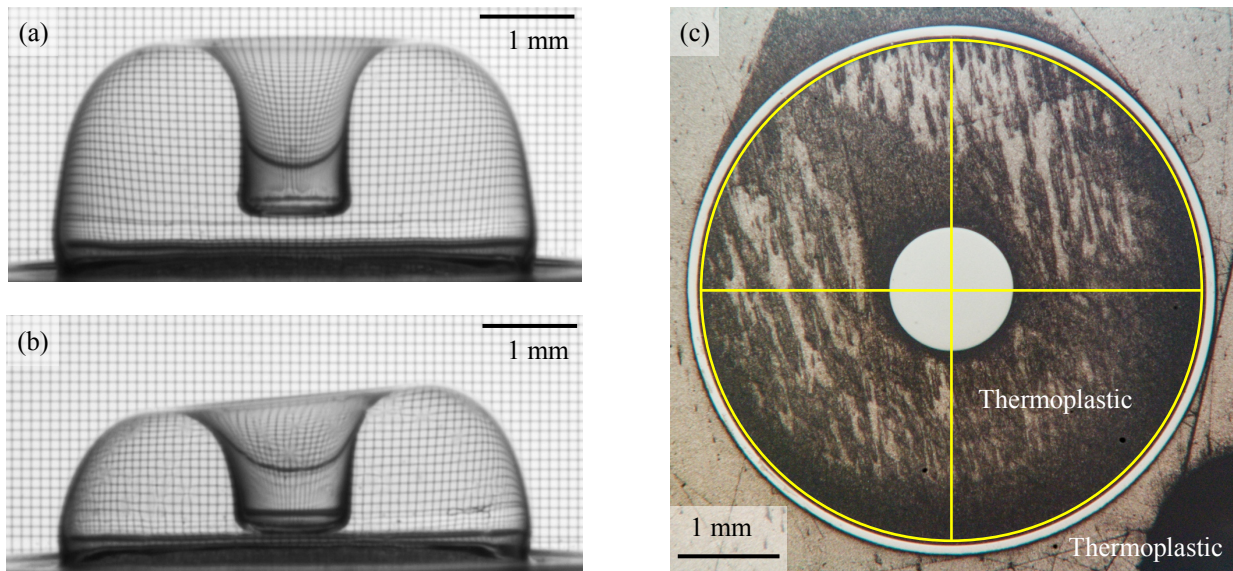
Figure 6.7: (a) shows a balanced BB-2.5 resonator photographed against a reference optical grid with 100 μm spacing. (b) shows a BB-2.5 resonator with a 20% height imbalance, caused intentionally by misaligning the torch and mold. (c) shows a photo of a BB-2.5 resonator with a circle superimposed to look for circularity imperfections.

The simulated Q_{TED} of an ideal BB-2.5 resonator is over seven times higher than our best measured device. Even for the worst simulated scenario of a 33% reduction in Q_{TED} due to a 7% height imperfection, Q_{TED} is still 31.7 million, which is around five times higher than our best BB-2.5 experimental results. It is therefore concluded that TED is not the dominant energy loss mechanism for BB resonators.

6.4 Anchor Loss

Anchor loss refers to the loss of vibrational energy through a resonator's attachment point, or anchor. The structure of the resonator determines its anchor loss, and is therefore critical when designing for a high quality factor. Normal vibrational modes with mode numbers ≥2 have nodal points where there is zero displacement. A musical tuning fork is a good example of this. When the fork is tapped against a hard surface the tines begin to resonate out of phase in the flexural mode. Since they are always moving away or towards each other at the same time, there is a node where they connect to the handle (anchor). This allows the fork to be held by the handle with minimal anchor loss through your hand. If one side of the fork is removed, the node is lost and the vibrational energy is quickly dissipated through the anchor. Tuning fork gyroscopes use this same principle, but with a pair of microfabricated proof masses connected with cantilevers. If the anchors are located precisely at the node, anchor loss is eliminated.

Ring, disc, and hemispherical shell resonators take advantage of anchoring at the node as well. The wine-glass modes each have nodal points at the center and at four locations around the rim, as shown in Figure 6.8. The locations on the rim are not useful because they change depending on which WG mode is excited; however, the nodal point at the center is common to both modes, so it is the logical attachment point. If the resonator is cylindrically symmetric and anchored in the center, zero energy will be dissipated through the anchor. A BB resonator has a

123

hollow anchor with a flat region at the bottom that is fixed to a substrate. In reality, only the very

center is stationary, so even for an ideal resonator, the surrounding mass of the anchor will

displace slightly and pass mechanical waves to the substrate (Figure 6.9(a)). Despite this, the

anchor loss-limited quality factor, Q_{anchor}, is simulated to be 180.93 million for both WG modes

of an ideal BB-2.5 resonator.

Wine-Glass 1   Wine-Glass 2
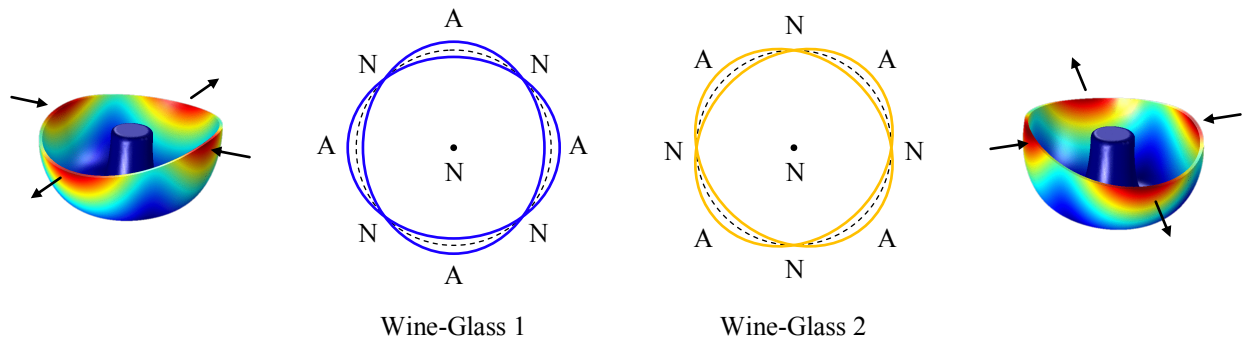
Figure 6.8: The location of nodes (N), where there is zero displacement, and anti-nodes (A), where there is maximum displacement, of the n = 2 wine-glass modes in the x'y' sensor plane.

If the anchor is not centered on the node, anchor loss will increase considerably. The BB

resonator geometry and fabrication process are designed to prevent this with inherently self-

alignment. The shell is defined from a single reflow-molding step using a cylindrically

symmetric mold, so there is no need to align multiple mask layers. The design also includes a

long, smooth transition region that connects the rim to the anchor. This long transition region

isolates the part with the most mechanical energy (rim) from the energy sink (anchor). The

smooth curvature also reduces the concentration of mechanical stress near the anchor. These

features effectively trap the mechanical energy in the rim, greatly reducing energy leakage to the

anchor. Still, rigid anchor attachment is required to minimize motion at the attachment point. We

have found that glass frit works well for this purpose.

As with Q_{TED}, it is important to consider the impact of fabrication imperfections on

Q_{anchor}. A simulated depiction of the effect of height and rim imperfections on anchor loss are

shown in Figure 6.9. For the perfect shell in Figure 6.9(a), there is zero anchor loss at the very center and a small amount in the outer regions of the anchor. Introducing a height (b) or circularity (c) imperfection shifts the center of mass and changes stiffness, causing an imbalance that increases the total anchor loss.
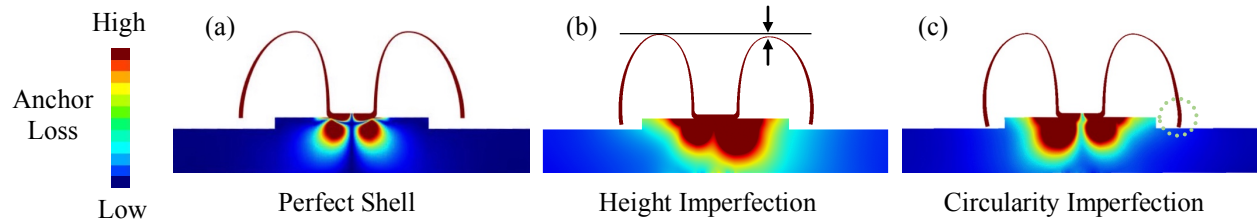
Figure 6.9: Visual comparison of anchor loss for a perfect shell (a) and a shell with a height imperfection (b) or a circularity imperfection (c). These imperfections increase and imbalance the anchor loss. Figures provided by Dr. Behrouz Shiari.
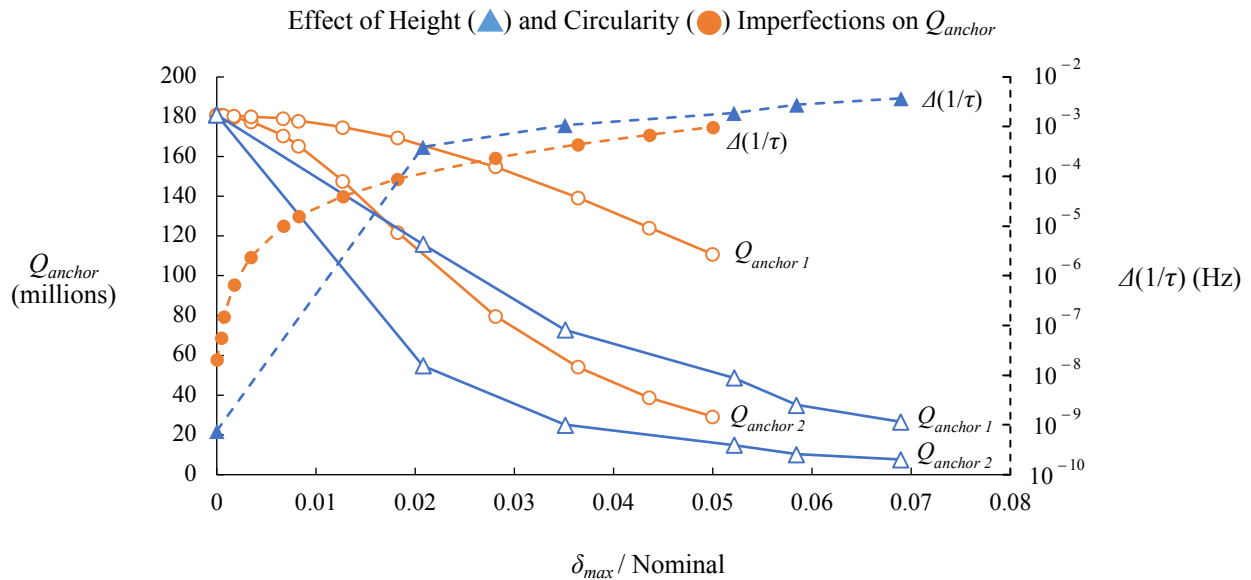

Figure 6.10: Effect of height and circularity imperfections on Q_{anchor} of each n = 2 WG mode and the resulting $\Delta(1/\tau)$.

Figure 6.10 shows the effect of height and circularity imperfections on the Q_{anchor} of both WG modes; the effect on Q_{anchor} is much greater than it is on Q_{TED}. A 7% height imperfection results in an average reduction in Q_{anchor} of 90% and a 10% difference between the two modes, which translates to a high $\Delta(1/\tau)$ of 2.8×10^{-3} Hz. Although the percent difference between modes is smaller than for Q_{TED}, $\Delta(1/\tau)$ is higher from the anchor loss perspective because the

overall Q and τ are lower, making $\Delta(1/\tau)$ more sensitive to mismatch. This principle is discussed in Section 4.3. A 5% circularity imperfection results in an average reduction in Q_{anchor} of 66%, but with a large 55% difference between modes that translates to a high $\Delta(1/\tau)$ of 2.6×10^{-3} Hz. As with Q_{TED}, there is a larger bifurcation in Q_{anchor} of the two modes for a circularity imperfection than for a height imperfection; the resulting increase in $\Delta(1/\tau)$ due to either height or circularity imperfections would be quite problematic.

The worst-case imperfections presented in these simulations would reduce Q_{anchor} to the 10 million range, which is on the order of experimental results; however, as discussed above, the blowtorch molding process produces highly symmetric shells, and imperfections on the high end of the simulated defect range have not been experimentally observed. Still, it is apparent that anchor loss could become the dominant energy loss mechanism, especially if multiple geometric imperfections are present.

The goal for this research is to achieve navigation-grade BI and ARW, which requires long τ, low $\Delta(1/\tau)$, and $Q > \sim 500,000$ depending on drive amplitude. A low Δf of < 5 Hz is also desirable to enable effective electrostatic tuning with less than 100 V. To meet all of these parameters with a BB-2.5 resonator, we can tolerate a height imperfection of ~0.5%, but almost zero rim imperfection due to how quickly the frequencies separate. Even if we remove the Δf goal, the tolerances are the same due to the rapid bifurcation of Q_{anchor} that increases $\Delta(1/\tau)$. Considering we have produced BB-2.5 and BB-5 resonators that meet the $\Delta(1/\tau)$ goal, with, we can conclude that fabricated shell symmetry is very high and that anchor loss is not likely the dominant loss mechanism.

6.5 Intrinsic Loss

Intrinsic loss, also known as bulk or internal loss, refers to energy dissipation within a material. A commonly accepted explanation for the source of intrinsic loss in FS is the generation of internal friction associated with strained Si–O–Si bonds. The bonds have energy minima at two different angles, forming an asymmetric double-well potential; strain leads to redistribution of the bond angles and therefore mechanical dissipation [110]. FS has exceptionally low intrinsic loss, and therefore low thermal displacement noise [111], [112]. This property led to its selection as the preferred material for the suspension fibers and mirrors of gravitational wave detectors, which require very high Qs to lower the noise floor. This requirement inspired extensive study of fused silica's intrinsic losses and Q limits and led to the observation of extremely high Qs, up to 203 million [59].

A number of exotic setups have been used to ensure operation in the intrinsic-loss-dominated regime. For example, methods to reduce anchor loss include a 10-cm-diameter FS cylinder that is supported by ruby balls at its nodal points [112], [113] and a rod of FS suspended from a series of fibers and heavy isolation bobs, all hand drawn from a single FS rod [59], [114]. Intrinsic loss can be separated from surface loss by measuring Q for fibers with varying diameters [59], [114], [115]; the fibers will become dominated by surface loss when the S/V ratio becomes high enough. Comparing the Q of cylinders supported along their central axis resonating at different frequencies with different mode shapes can help separate surface, anchor, and intrinsic loss [112], [113]. If the cylinder is supported at its nodes, there will not be any anchor loss for modes of orders greater than unity, while modes of order 0 or 1 will be limited by Q_{anchor}. The effect of surface loss is expected to be proportional to the strain energy on the surface, which varies with mode shape. If higher order modes have similar Qs to lower order

modes, it can be concluded that intrinsic loss is dominant. This is not the case for the BB resonator; higher order WG modes have been found to have lower Qs, as shown in Figure 6.12. BB resonators have also been found to be highly sensitive to their surface conditions. Considering these observations and that the measured Qs of BB resonators are over an order of magnitude below those of intrinsic-loss-limited resonators, we can conclude that BB resonators are not currently dominated by intrinsic loss.

6.6 Surface Loss

Surface loss refers to energy dissipation related to the surface of a resonator. For macro-scale resonators with a low S/V ratio, other energy loss mechanisms are dominant and the surface loss can be ignored; however, as the dimensions scale down, the S/V ratio increases to the point where surface loss can become the dominant loss mechanism. We believe this is the case for BB resonators. Three types are surface loss are discussed: that related to the fused silica resonator itself, that due to the presence of surface contaminants, and that due to the addition of a conductive layer.

6.6.1 Fused Silica Surface

There is no consensus on the exact mechanism of FS surface loss, but it is believed that strain on the surface causes energy dissipation. One theory on the physical origin of surface loss is that strained Si-O-Si (siloxane) surface groups with larger bond angle distributions near the surface than the bulk are responsible for energy dissipation due to applied strain [116]. This is similar to the commonly accepted mechanism for intrinsic dissipation due to an asymmetric double-well potential arising from strained siloxane bonds in bulk FS. The difference of the surface state compared to the bulk has been described by excess energy called surface free energy [68].

128

Several researchers have proposed numerical models for surface loss. These models are helpful for fitting data and predicting the limitations of a given process and design. Yasumura et al. present a formula for $Q_{surface}$ for cantilevers:

$$Q_{surface} = \frac{wb}{2\delta\,(3w + b)}\frac{E_1}{E_2^S} \tag{6.4}$$

where w is the beam width, b is beam thickness, δ is surface layer thickness, and E_1 and E_2^S are the conventional (real-valued) and dissipative Young's moduli of the surface layer, respectively [117]. E_2^S is explained as a property of the absorbate layer and its defects that is closely related to surface stress and that results in surface loss [118]. Due to the difficulty in characterizing δ and E_2^S, they are typically determined by fitting the data for a given fabrication process [119].

Ru derives a formula for $Q_{surface}$ of a micro-cantilever following the ideas of Zener's "anelastic" model:

$$\frac{1}{Q_{surface}} = \omega K \frac{E_s(\tau_\sigma - \tau_\epsilon) + \gamma v \tau_\epsilon}{D_{eff} + \omega^2 K\tau_\epsilon + EI\tau_\epsilon} \tag{6.5}$$

where ω is angular frequency, E_s is the surface elastic modulus, τ_σ and τ_ϵ are relaxation times that characterize time-dependent deformation and dissipation, γ is surface tension, v is the Poisson ratio of the bulk material, D_{eff} is the effective bending rigidity of the cantilever taking initial surface tension into account, and EI is the bending rigidity (K is not explicitly defined) [120]. This method seeks to calculate $Q_{surface}$ more directly from the device geometry, but still requires knowledge of parameters that typically must be found experimentally.

Gretarsson and Harry have performed extensive analysis on energy dissipation in fused silica fibers. They describe the surface loss angle, $\phi_{surface}$, as

$$\phi_{surface} = \mu d_s \frac{S}{V} \tag{6.6}$$

where $\phi_{surface} = 1/Q_{surface}$ at resonance, μ is a factor of order unity that depends on the resonant mode shape, d_s is the surface loss parameter (given as δ in Equation 6.4), and S/V is the surface-to-volume ratio [114]. Modes with higher strain on the surface will produce a higher μ. Derivations of μ and d_s are given in [114]. They can be determined experimentally if the S/V ratio is known. To identify d_s, several resonators with similar structures but different S/V ratios can be operated in the same mode. Once d_s is found by fitting the data, μ can be calculated. When d_s is on the order of or greater than the minimum thickness of the resonator, surface loss is likely to be the dominant loss mechanism. Penn et al. find that d_s is typically several picometers for flame-polished fused silica, but much higher for abrasively polished surfaces [110]. Despite their high S/V ratio, BB resonators have the advantage of having very smooth flame-polished surfaces with Angstrom-level roughness; however, considering the following evidence, it appears they are still limited by surface loss.

Equations 6.4–6.6 all include a parameter that takes surface strain into consideration because energy is dissipated when the surface of a resonator is strained. Resonant modes that generate higher surface strain due to their mode shape will therefore incur higher surface loss [110], [112]. Using FEM, Dr. Behrouz Shiari confirmed that the stress, and therefore strain, generated on the surface of a BB resonator increases with mode order. This is modeled by analyzing the normal stress induced on the surface mesh elements around the rim of a BB-2.5 resonator due to displacement during oscillation in the WG modes. The simulation is limited to the rim to reduce computational cost; however, the rim experiences the highest strain of any part of the shell in the WG modes and is representative of the rest of the surface. Figure 6.11 shows the normalized stress in the radial direction, σ_{rr}, at each location around the rim when the shell flexes in the $n = 2$, 3, and 4 WG modes. The higher surface stress in the higher order modes is

expected to lead to increased surface loss. This has been experimentally observed with BB resonators when measuring wine-glass modes of higher orders, as shown in Figure 6.12 for several BB-2.5 resonators.
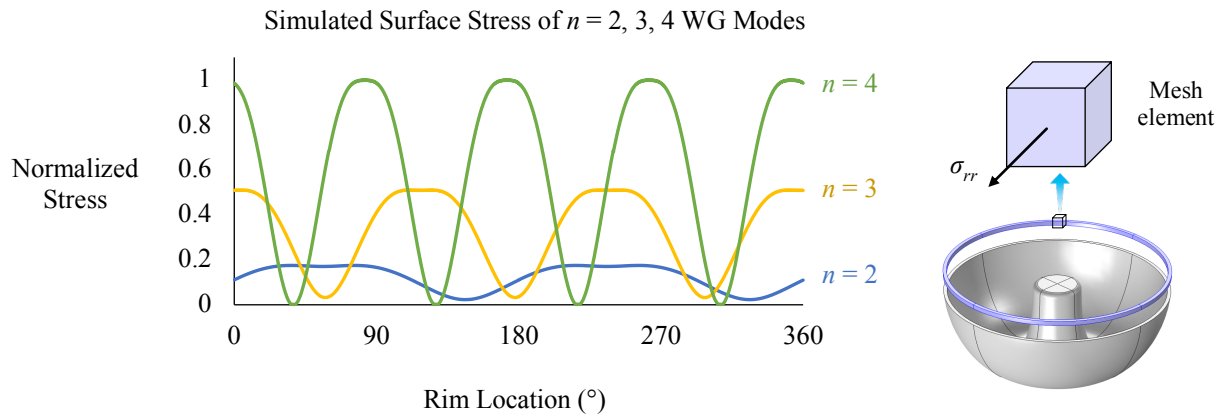
Figure 6.11: FEM analysis of the radial tensors generated on the outer mesh elements of the rim of a BB-2.5 resonator due to displacement during oscillation in the n = 2, 3, and 4 WG modes. The stresses are normalized, as their magnitudes are not necessarily accurate. More important is their proportionality, which indicates that higher surface stress and therefore strain is generated in n = 3 and 4 modes.
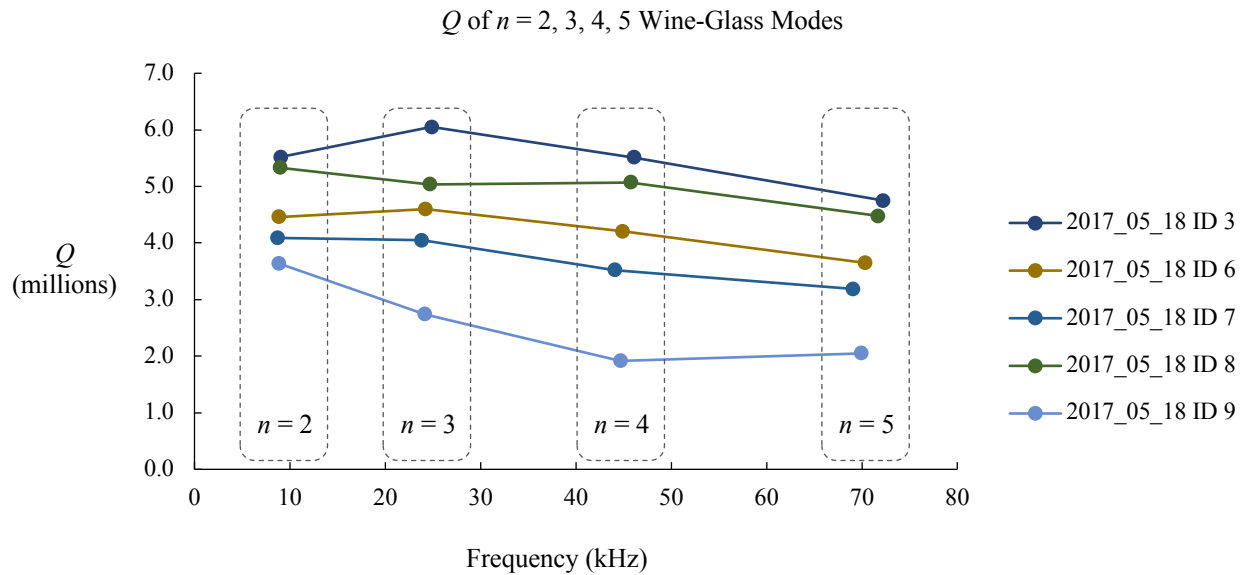
Figure 6.12: Comparison of Q for the n = 2, 3, 4, and 5 WG modes of five BB-2.5 resonators fabricated in the same batch. Higher order modes incur higher surface strain, which is believed to lower Q due to increased surface loss.

Researchers working on the LIGO gravitational wave detectors have thoroughly investigated loss mechanisms in FS, as their measurement accuracy is limited by the quality

factor of their FS interferometer mirrors. They have found that for thin suspension fibers and other structures with a high S/V ratio they are limited by surface loss. A summary of the relationship between Q^{-1} and V/S ratio (inverse of S/V ratio discussed previously) for samples from many different publications including fibers and solid masses is given in Figure 6.13. The performance of the highest Q BB resonators for each size presented in Table 3.1 is overlaid for comparison.

The BB-1.5 resonator has the highest S/V ratio and is relatively far from the surface loss "limit"; however, this result is quite old, as BB-1.5 resonators have not been fabricated since the beginning of this work. Performance would likely be improved if new devices were fabricated with the updated techniques. The LIGO community is at the forefront of high-Q FS structures and have published the highest Qs of any FS resonator. Still, the BB-2.5 and BB-5 resonators all achieve performance better than the surface loss "limit," and better than the results reported by the LIGO community at the same S/V ratios. Clearly this is not an absolute surface loss limit, as it depends on parameters such as the mode shape and lossy surface layer thickness, but it provides a helpful trend for comparing resonators believed to be in the surface-loss-limited regime. The BB resonators closely follow the Q^{-1} vs. V/S ratio trend, providing strong evidence that they are indeed limited by surface loss. We believe a major reason for the superior performance achieved by BB resonators is due to the blowtorch reflow of the entire structure, which leaves a highly uniform material with less than 2 Å of surface roughness.
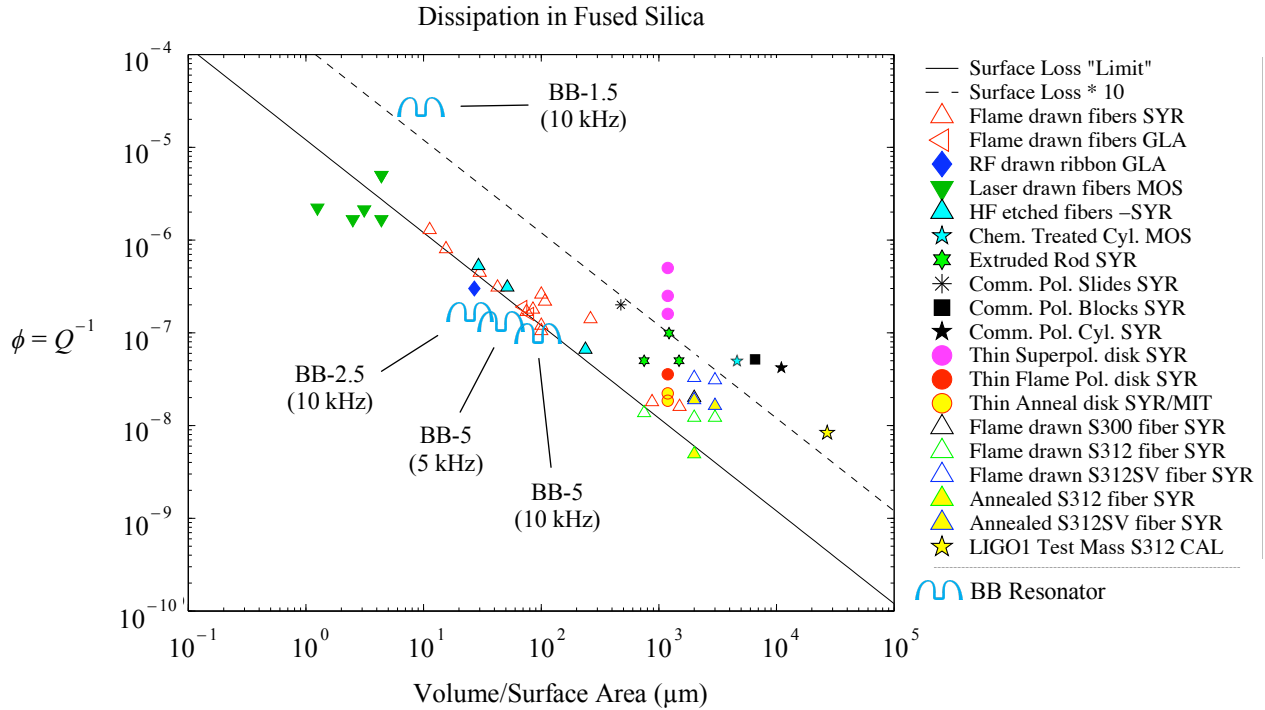
Figure 6.13: Summary of loss angles with respect to volume-to-surface ratio for a number of works. Original plot is from [116]; *the best performance achieved for each of the BB resonator designs presented in Table 3.1 are overlaid for comparison.*

BB resonators achieve unprecedented performance for resonators of their size. Based on the observed dependences of Q on WG mode number and S/V ratio that align with the literature, we believe BB resonators of the dimensions presented in Table 3.1 are limited by surface loss within the fused silica. This makes their Qs highly sensitive to surface contaminants and added layers, as discussed in the following sections.

6.6.2 Surface Contaminants

We have experimentally observed a high sensitivity of BB Q factors to surface contaminants. There are many possible sources of surface contamination, including adsorbed water [121], [122], adsorbed gas molecules [121], [123], adsorbed organic compounds [121], carbonaceous contamination [124], and water diffusion [125]. Loss mechanisms that result from these types of contamination include surface scattering [126], interfacial losses [99], and acoustic dissipation [123].

Ono and Esashi find that adsorbed gas molecules and contaminants capture single or multiphonons and emit them as acoustic dissipation [123]. This sort of dissipation is expected to be higher on the surface compared to the bulk due to the higher concentration of defects on the surface. Yasumura et al. reported improvement in Q by a factor of three following annealing of 1700-Å-thick single-crystal silicon cantilevers for 1 hour at 700 °C in N_2 [117]. They also reported a factor of two increase for 700-Å-thick cantilevers following 1 hour at 700 °C in forming gas (95.75/4.25% Ar/H_2). They attribute these results to improvement of surface defects created during fabrication and to removal of adsorbates.

We have observed the same phenomenon with uncoated BB-2.5 resonators when baking them in a Yield Engineering Systems oven at 450 °C in forming gas (95/5% N_2/H_2) at 200 Torr and at 600 °C in a Sentro Tech oven in Ar at atmospheric pressure. Temperature was limited by the YES oven and by the glass frit used to attach the resonators to their silicon carrier substrates, which melts at ~500 °C. For both ovens, the temperature is ramped slowly at 2 °C/min to reduce thermal stress at the resonator attachment point. Resonators baked in forming gas at 450 °C showed improvements up to ~2.7× (Figure 6.14(a)), while those baked in Ar at 600 °C typically improved by ~1.75× (Figure 6.14(b)). One exceptional device had a low Q before annealing and improved by ~13×. These results are summarized in Figure 6.14. The BB-2.5 resonators in Figure 6.14 were not coated with a protective metal barrier layer during lapping and CMP, so it is possible that there was thermoplastic residue remaining on their surfaces that is removed during baking.

Baking in forming gas rather than Ar may be beneficial due to a change in surface termination. The surface of fused silica in atmosphere is commonly terminated by silanol groups (SiOH) that are susceptible to hydration in the presence of humidity [123], [127], [128]. For the

case of silicon resonators with an oxide layer having an OH termination with a thin water layer, it has been shown that exposure to H_2^+ ions will terminate the active sites on the surface and make them inactive or less active to mechanical dissipation, increasing the Q [123]. It is possible that resonators baked in forming gas and Ar reach the same Q during baking, but the bake-out is *ex situ*, so there is a ~20-minute delay between bake-out and testing during which the resonators are exposed to atmosphere. Exposure to the H_2 in forming gas may create a more lasting effect than Ar due to surface passivation, accounting for the difference in improvements measured for these two bake-out environments. More data needs to be collected on baking in an Ar atmosphere before it can be confidently compared to forming gas.
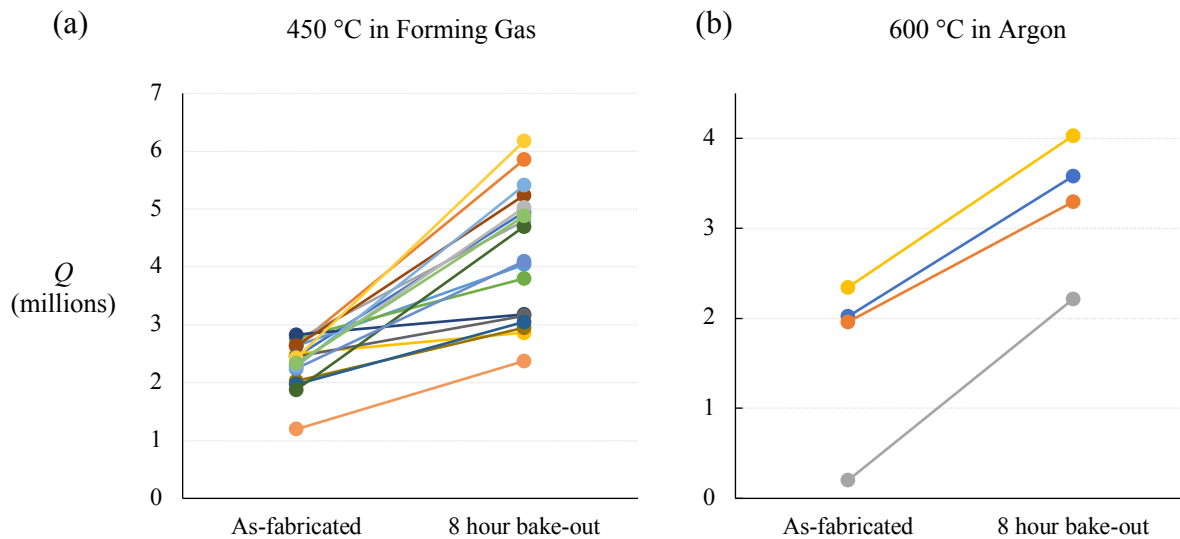
Figure 6.14: BB-2.5 resonators without a conductive coating show a considerable performance improvement after baking at elevated temperatures in both forming gas (95/5% N₂/H₂) (a) and Ar (b). Several devices baked in forming gas improve by ~2.7×. Devices in Ar typically improve by ~1.75×, with one exceptional device with initially low Q improving by over ~13×. These resonators did not have a metal barrier layer on their surfaces during lapping and CMP.

We have also observed that BB-5 resonators with a metal barrier layer applied before thermoplastic encapsulation tend to improve with baking, but not as significantly as BB-2.5 resonators without the barrier layer. Improvements of up to ~2×, which are still quite large, have been observed for BB-5 resonators baked under identical conditions to the BB-2.5 resonators.

These results are summarized in Figure 6.15. The large benefit of bake-out seen by devices with a metal barrier layer suggests that the improvement is not only from removal of thermoplastic residue, but also due to removal of adsorbed water, which can be removed at 330 °C [122], and other contaminants from the surface.
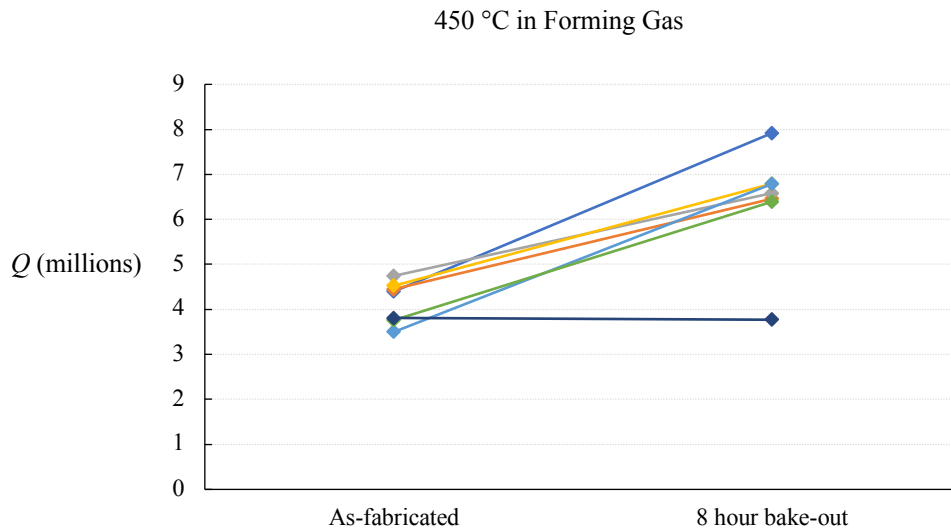
Figure 6.15: BB-5 resonators without a conductive coating show a considerable performance improvement after baking at 450 °C in forming gas (95/5% N_2/H_2). Improvements of up to ~2× are seen. These resonators had a metal barrier layer deposited during lapping and CMP.

The removal of contaminants from the surface of BB resonators is temporary. We have observed that Q tends to drop over time for resonators stored in a ~200 Torr chamber in air. In addition to the gradual decline in performance, it was also observed that each time resonators were left in the LDV test chamber at ~1 μTorr overnight, their Qs dropped. Figure 6.16 shows the performance of one BB-2.5 resonator over 6 months. The Q reduction appears to follow an exponential decay, settling out around half of the initial value. This reduction is caused by two mechanisms that both affect the surface. The slow reduction is due to adsorption of water and other contaminants from the atmosphere. The rapid reduction associated with storage in the LDV vacuum chamber was traced to a patch of adhesive residue in the test chamber that was outgassing and depositing onto the resonator surface. The Q is restored to near its initial value

with a bake-out in N_2 at 300 °C for 1 hour that removes these residues and adsorbates. After cleaning the residue from the LDV test chamber, BB resonator Qs were observed to improve when left in the vacuum chamber; as shown in Figure 5.10, leaving the resonators under vacuum in a clean chamber for 15 days causes their Qs to increase by up to 25% (Device 1) from the value measured immediately after bake-out. This suggests that moisture and other contaminants adsorb on the resonator surfaces during transfer from the oven to the test chamber, but that they will eventually desorb from the surface under vacuum.
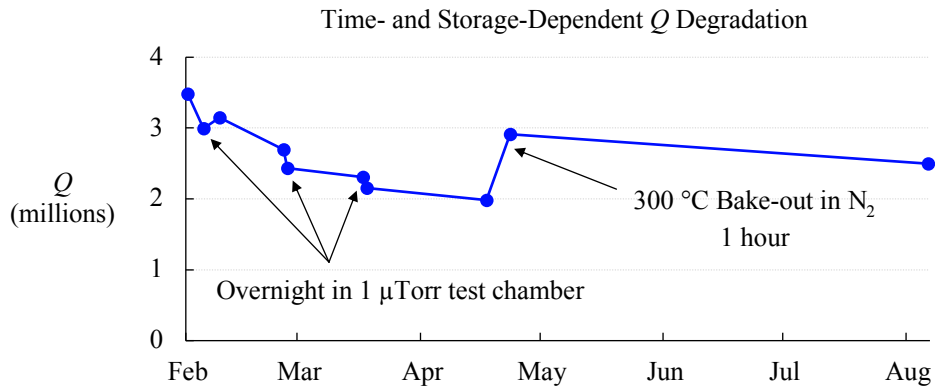
Figure 6.16: Degradation of Q is observed over time and due to leaving the resonator in the LDV vacuum test chamber at ~1 μTorr overnight. It was determined that residue in the test chamber was outgassing and depositing on the resonator. An N₂ bake-out largely restores the initial performance.

A time-dependent reduction in Q was also observed by Liu et al. for a silicon micromechanical oscillator [129]. Similarly, they found that the reduction could be reversed with an 800 °C anneal for 30 s in N_2, but that Q began to degrade right after annealing. They attribute this phenomenon to adsorption of water, oil, other hydrocarbons, and even metallic particles that the resonator may be exposed to due to the *ex situ* nature of their annealing process. We believe BB resonators are subject to the same phenomena.

The BB resonator fabrication process also carries the risk of introducing a large number of particles during the CMP process. As discussed in Section 3.3.6, silica nanoparticles from the CMP slurry tend to stick to the sidewalls of BB resonators when their rims are polished. Figure

6.17 shows the copious number of silica nanoparticles left on the rims even after ultrasonic cleaning. It is difficult to model the full extent of the resulting energy loss, but a considerable amount of friction will be generated as the particles rub against each other and the resonator sidewall during oscillation. Fortunately, the adsorption of these particles can be largely prevented by applying a metal barrier layer to the shells before the lapping and CMP processes.
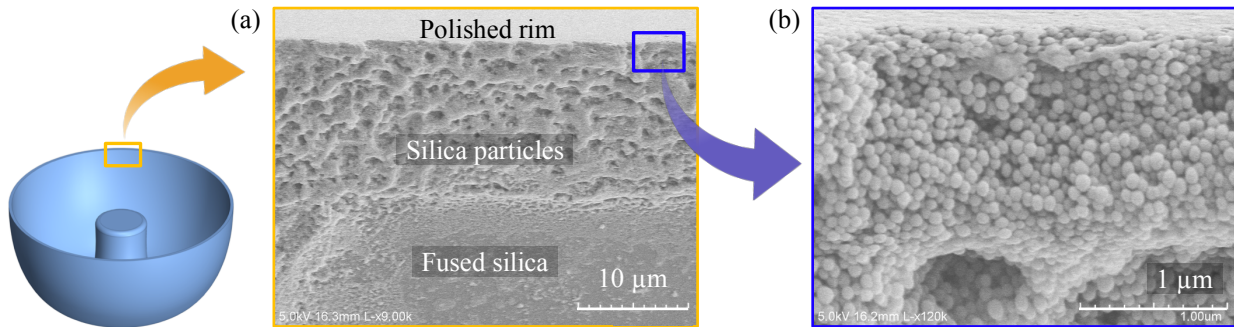
Figure 6.17: Copious numbers of silica nanoparticles from the CMP slurry used to polish BB resonator rims remain adsorbed on the rim surface sidewalls, even after ultrasonic cleaning. Friction generated during oscillation will cause energy loss.

6.6.3 Conductive Layer

The addition of foreign species onto the surface of BB resonators is undesired and clearly has a strong effect on performance; however, it is necessary to apply a conductive layer to enable electrostatic transduction. Chapter 5 presents experimental results showing high sensitivity to an added conductive layer. It is found that even the addition of a 30-Å-thick Cr/Au or Ti/Pt layer can reduce Q by ~40–50%, and that adding a thicker layer continues to reduce Q. As discussed in Section 5.4.2.4, pile-up and transfer of dislocations at metal grain boundaries has been proposed as a source of energy dissipation within deposited metal films [85]. We have seen changes in Q that accompany formation and growth of metal grains, but did not observe a definitive trend with regard to this mechanism, so we do not believe it is dominant.

Others have also observed high sensitivity of FS resonators to added surface layers. Gretarsson et al. analyzed the effect of a high-reflective (HR) coating on the Q of polished FS

microscope slides measuring 76 mm × 25 mm × 1 mm [130]. They found that the addition of a 2.4-μm-thick coating of 14 alternating layers of SiO_2 and Ta_2O_5 reduced Q by almost two orders of magnitude from 4.9 million to 110,000. They also reported that the equivalent dissipation depth of the sample increases from 0.86 mm to 46 mm as a result of the added layer. They do not offer a physical explanation for the cause of loss, but suggest it is due to a lossy interface between the coating and the silica. Based on the discussion of Equation 6.6, the equivalent dissipation depth of 0.86 mm before adding the HR coating means the slide is in the surface-loss-limited regime before deposition, making it highly sensitive to its surface condition.

Hao and Liao present an analytical study on interfacial dissipation in [99]. They explain that from the continuum mechanics perspective, energy dissipation at the interface of two solid materials can be explained by thermal energy generation and dissipation. Because the layers are stacked, there is strain compatibility at their interface; however, they have different Young's moduli, causing an increase in stress at the interface under applied strain. This stress causes an interfacial slip that can occur without breaking the interfacial bond of the two solid layers. This slippage generates thermal energy due to friction that is dissipated.

It follows that the presence of even a very thin layer with a different Young's modulus from FS would cause a large increase in energy dissipation, and that as the layer thickness increases, that more stress would be generated and therefore more energy would be dissipated. Indeed, this matches the experimental results collected throughout this research, and we posit that interfacial energy dissipation is the dominant loss mechanism in BB resonators with a conductive surface layer. This source of loss could be reduced by matching the Young's modulus of the conductive layer as closely as possible to that of the fused silica (72.7 GPa); however, it is difficult to make this selection, as the published values vary widely depending on deposition

139

process, conditions, and film thickness. Future work on this research would likely benefit from the characterization of Young's moduli of suitable conductive layers to verify this theory. The use of ALD rather than sputtering should also reduce loss, as a thinner and more uniform film can be applied to produce a conductive path from anchor to rim.

6.7 Conclusion

There are many known energy dissipation mechanisms, only a handful of which are relevant to this research and are discussed here. Many different parameters determine which mechanism is dominant, including resonator design, size, shape, frequency, material, operating atmosphere, and cleanliness standards. BB resonators are designed from the ground up to mitigate energy dissipation mechanisms that typically limit MEMS resonators. FS is chosen due to its low intrinsic loss and low TED. While FS is a historically difficult material to work with on the micro scale, our novel blowtorch fabrication technique allows us to create high-aspect ratio structures with a high level of precision and control in three dimensions. By forming the entire shell geometry in a single molding step, the anchor is automatically aligned to the rest of the resonator. This self-aligned and long, mechanically isolated anchor enables us to avoid being dominated by anchor loss, which is a common challenge for cylindrically symmetric MEMS resonators. Intrinsic and surface losses are unavoidable damping mechanisms that will ultimately limit the Q of any FS resonator. The highest Qs are achieved for FS resonators that are limited by intrinsic dissipation, but it is difficult to reach this regime on the MEMS scale.

Birdbath resonators are designed to function as high-performance rate or rate-integrating gyroscopes. To improve their performance, we need to minimize ARW and BI. ARW is related to thermo-mechanical noise, while BI is related to circuit noise and changes in resonator characteristics due to environmental variations. ARW can be reduced by maximizing Q, while BI

can be reduced by maximizing τ and minimizing $\Delta(1/\tau)$. If we simply wanted to maximize Q, we could create a thick resonator with a low S/V ratio that operates at a high frequency but has less surface loss; however, this would make it very difficult to achieve long τs and low bias instability. If we only needed low bias instability, we could create a very thin and low-frequency shell that has higher surface loss and lower Q but achieves long τs and low $\Delta(1/\tau)$. We need to strike a balance between frequency, size, and Q in order to optimize the birdbath resonator gyroscope. The results of this optimization and the novel design of the BB resonator have led to a surface-loss-limited regime. With the deposition of a conductive layer, we believe this transitions to an interfacial-loss-limited regime. Despite these limitations, we achieve unprecedented performance for resonators of this scale.

Chapter 7

Conclusions and Future Work

7.1 Summary

There is a need for an affordable supplementary navigation technique to assist the growing number of technologies that rely on GPS. Dead reckoning navigation using inertial sensors is an excellent choice, as it does not require any external frame of reference and is not susceptible to interference; however, to maintain accurate navigation, the sensors must have low drift. The only commercial gyroscopes that achieve sufficiently low drift are too large, heavy, and too expensive for the majority of applications. MEMS Coriolis vibratory gyroscopes are a promising technology with the potential to address the growing interest in dead reckoning navigation from the defense, aerospace, and consumer sectors. They have long been used for less demanding applications because of their low cost, size, weight, and power requirements, but so far they have fallen short of the performance of high-end macro-scale gyroscopes. The birdbath resonator gyroscope presented in this research is designed to fill this gap.

One of the major barriers to achieving navigation-grade performance with a MEMS CVG is the increased sensitivity to noise at the micro-scale. Micro-scale sensors measure smaller quantities and are therefore more susceptible to fundamental noise sources than their macro-scale counterparts. The challenge of controlling dimensions as structures scale down further increases the tendency for sensor drift.

This research has focused on the development of a high aspect ratio fused silica micro-shell resonator, the BB resonator, to reduce two types of drift: bias instability and angle random walk. The BB resonator is fabricated with a novel blowtorch molding process that enables a high level of control over its shape in three dimensions and enables rapid and affordable prototyping of new designs that are not possible with conventional micromachining. Considerable emphasis was put on the resonator's quality factor, Q, and the symmetry and length of its vibratory decay time constants, τ, as these are directly related to ARW and BI, respectively.

B and BI are improved with low damping asymmetry, $\Delta(1/\tau)$, which we have attempted to minimize by producing highly symmetric resonators with very long τs. Damping asymmetry as low as 2.2 µHz has been demonstrated in a 10-mm-diameter resonator with τ of 495 s and a difference between τ_1 and τ_2 of only 0.54 s. The difference between wine-glass mode frequencies is also low, with an untuned Δf of only 5.74 Hz at 5.13 kHz that helps improve gyroscope resolution. This performance indicates an extremely high degree of structural and damping symmetry, and a very low level of energy dissipation. Indeed, this device has a Q of 7.97 million. It is expected to achieve navigation-grade BI and ARW, with an estimated ARW of ~6.5×10^{-4} °/$\sqrt{\text{hr}}$. Even higher Qs have been demonstrated, up to 9.81 million for a similar device, but at a higher frequency of 10.97 kHz. This device still achieves a low untuned Δf of 10.3 Hz and has an even lower expected ARW of 5.9×10^{-4}°/$\sqrt{\text{hr}}$. This resonator performance is unrivaled amongst comparable published MEMS resonators.

To reach these levels of Q and τ, simulations and experiments were performed to determine the dominant energy loss mechanism. It was observed that BB resonators are very sensitive to their surface condition due to their particularly high S/V ratio. This discovery led to the investigation of surface treatments, including protective barrier layers and baking in forming

gas to remove adsorbed species. The process improvements implemented over the course of this research increased the performance of BB resonators by nearly two orders of magnitude, bringing them up to the theoretical surface loss limit. They have achieved even lower energy loss than resonators with the same S/V ratio published in support of gravitational wave detection research.

To operate BB resonators as gyroscopes, it is necessary to deposit a ~65-Å-thick conductive film on the surface. Because of their sensitivity to surface condition, even this thin layer has a major negative impact, reducing Q by ~50%. Several different conductive layers have been tried, including Cr/Au, Ti/Pt, TiN, and ITO. The first three all have similar effects, reducing Q by ~50%, but initial trials with ITO show that the resonator may maintain 70% of its initial Q. Further investigation is necessary to fully characterize this film and to confirm its efficacy as an electrode for gyroscope operation.

It is surprising to see such a large reduction in Q due to the deposition of a 65-Å-thick layer onto one side of a ~80–150-μm-thick resonator. This large loss is attributed to interfacial dissipation between the FS and conductive layer. The difference in Young's modulus between the two layers generates a large stress during flexion that causes the generation and dissipation of thermal energy. This source of energy dissipation may be mitigated by identifying a conductive layer with a Young's modulus that is closely matched to that of FS.

7.2 Future Work

7.2.1 Fused Silica Annealing

The blowtorch molding process happens in only ~10 seconds, during which the fused silica substrate is heated from room temperature to around 1700 °C and back down to room temperature. While softened, the substrate undergoes extreme deformation, stretching several

millimeters out of plane and therefore thinning by more than 80% in some regions. The rapid cooling following the molding process likely results in stress gradients developing in the shell. High temperature annealing at around 900 °C has been shown to relieve internal stress in FS resonators and reduce intrinsic loss.

BB resonators are dominated by surface loss, but even for resonators in which intrinsic loss is not the dominant energy loss mechanism, annealing has been shown to improve Q. We have observed improvements after baking at 450–600 °C, which is sufficient to remove adsorbed water and gas molecules, but higher temperatures are noted to improve Q by reducing OH content in the FS matrix [131]. It has also been suggested that SiOH groups may be responsible for energy dissipation, and that these can be removed by baking in vacuum at 900 °C [122]. Therefore, even if annealing does not improve the Q of BB resonators by reducing intrinsic loss, there are other dissipation mechanisms that may be mitigated.

7.2.2 Conductive Layer ALD

The films presented in this research were deposited with sputtering, which is the most conformal PVD technique. CVD produces more conformal films, but the purity is not high enough to achieve sufficient conductivity at the desired low film thickness. ALD is a promising candidate, as it results in uniform, conformal films with excellent thickness control as fine as 0.1 Å per layer. It has been observed that for sputtered films, an initial deposition of only 30 Å of metal reduces Q by around 40%, and that subsequent deposition up to the required 65 Å continues to reduce Q by up to 60%. It is not expected that ALD would eliminate this loss, but due to its high deposition conformality, a thinner layer could be used. It is expected that this would prevent Q from dropping by more than ~30%. Except for Cr/Au, all of the conductive

films trialed in this research can be deposited with ALD. Based on the findings presented, ALD

ITO is a promising candidate for a low-loss conductive layer.

References

[1] G. Turner, "History of Gyroscopes," 2017. [Online]. Available: http://www.gyroscopes.org/history.asp. [Accessed: 06-Mar-2017].

[2] T. B. Greenslade, "Bohnenberger's Apparatus." [Online]. Available: http://physics.kenyon.edu/EarlyApparatus/Mechanics/Bohnenbergers_Apparatus/Bohnenbergers_Apparatus.html. [Accessed: 06-Mar-2017].

[3] T. B. Greenslade, "Gyroscope." [Online]. Available: http://physics.kenyon.edu/EarlyApparatus/Mechanics/Gyroscope/Gyroscope.html. [Accessed: 06-Mar-2017].

[4] T. Mai, "Global Positioning System History," *NASA*, 2017. [Online]. Available: https://www.nasa.gov/directorates/heo/scan/communications/policy/GPS_History.html. [Accessed: 11-Sep-2017].

[5] U.S. Air Force, "GPS Accuracy," *How accurate is GPS?*, 2017. [Online]. Available: http://www.gps.gov/systems/gps/performance/accuracy/#how-accurate. [Accessed: 03-Mar-2017].

[6] Stanford University, "The Extraordinary Technologies of GP-B." [Online]. Available: https://einstein.stanford.edu/TECH/technology1.html. [Accessed: 11-Aug-2017].

[7] "Ring laser gyroscope," *Encyclopaedia Britannica*, 2017. [Online]. Available: https://www.britannica.com/technology/ring-laser-gyroscope. [Accessed: 11-Aug-2017].

[8] E. A. Donley, "Nuclear magnetic resonance gyroscopes," in *2010 IEEE Sensors*, 2010, pp. 17–22.

[9] G. W. Hoth, B. Pelle, S. Riedl, J. Kitching, and E. A. Donley, "Point source atom interferometry with a cloud of finite size," *Appl. Phys. Lett.*, vol. 109, no. 7, p. 71113, Aug. 2016.

[10] A. A. Trusov, A. D. Meyer, G. H. McCammon, A. Bettadapura, and M. R. Philips, "Toward software defined coriolis vibratory gyroscopes with dynamic self-calibration," *2016 DGON Inert. Sensors Syst. ISS 2016 - Proc.*, 2016.

[11] J. Bernstein, S. Cho, A. T. King, A. Kourepenis, P. Maciel, and M. Weinberg, "A micromachined comb-drive tuning fork rate gyroscope," in *[1993] Proceedings IEEE Micro Electro Mechanical Systems*, 1993, pp. 143–148.

[12]   G. M. Keiser *et al.*, "Gravity probe B," *Riv. del Nuovo Cim.*, vol. 32, no. 11, pp. 555–589, 2009.

[13]   G. T. Schmidt, N. M. Barbour, P. Robertson, R. E. Hopkins III, M. Angermann, and M. J. Veth, "Low-Cost Navigation Sensors and Integration Technology," 2011.

[14]   H. Yu, W. Wu, M. Wu, G. Feng, and M. Hao, "Systematic angle random walk estimation of the constant rate biased ring laser Gyro," *Sensors (Switzerland)*, vol. 13, no. 3, pp. 2750–2762, 2013.

[15]   D. S. Durfee, Y. K. Shaham, and M. A. Kasevich, "Long-Term Stability of an Area-Reversible Atom-Interferometer Sagnac Gyroscope," *Phys. Rev. Lett.*, vol. 97, no. 24, p. 240801, Dec. 2006.

[16]   A. D. Challoner, H. H. Ge, and J. Y. Liu, "Boeing Disc Resonator Gyroscope," in *2014 IEEE/ION Position, Location and Navigation Symposium - PLANS 2014*, 2014, pp. 504–514.

[17]   D. Meyer and M. Larsen, "Nuclear magnetic resonance gyro for inertial navigation," *Gyroscopy Navig.*, vol. 5, no. 2, pp. 75–82, 2014.

[18]   J. Kitching, S. Knappe, and E. A. Donley, "Atomic Sensors – A Review," *IEEE Sens. J.*, vol. 11, no. 9, pp. 1749–1758, Sep. 2011.

[19]   R. Antonello and R. Oboe, "MEMS Gyroscopes for Consumer and Industrial Applications," *Microsensors*, pp. 253–280, 2011.

[20]   Ieee, *IEEE Standard Specification Format Guide and Test Procedure for Single –Axis Interferometric Fiber Optic Gyros*, vol. 1997. 1998.

[21]   E. J. Loper and D. D. Lynch, "Projected System Performance Based on Recent HRG Test Results," in *Proceedings/IEEE/AIAA 5th Digital Avionics Systems Conference*, 1983, p. 18.1.1 – 18.1.6.

[22]   F. Marcelja, D. B. DeBra, G. M. Keiser, and J. P. Turneaure, "Precision spheres for the Gravity Probe B experiment," *Class. Quantum Gravity*, vol. 32, no. 22, p. 224007, Nov. 2015.

[23]   KVH Industries Inc., "Guide to comparing gyro and IMU technologies – Micro-electro-mechanical systems and fiber optic gyros." pp. 1–10, 2014.

[24]   Vectornav, "Inertial Measurement Units and Inertial Navigation," 2017. [Online]. Available: http://www.vectornav.com/support/library/imu-and-ins. [Accessed: 03-Mar-2017].

[25] J. Cho, J. Yan, J. A. Gregory, H. Eberhart, R. L. Peterson, and K. Najafi, "High-Q Fused Silica Birdbath and Hemispherical 3-D Resonators Made by Blow Torch Molding," in *2013 IEEE 26th International Conference on Micro Electro Mechanical Systems (MEMS)*, 2013, pp. 177–180.

[26] M. I. Younis, *MEMS Linear and Nonlinear Statics and Dynamics*, vol. 20. 2011.

[27] P. Greiff, B. Boxenhorn, T. King, and L. Niles, "Silicon monolithic micromechanical gyroscope," in *TRANSDUCERS '91: 1991 International Conference on Solid-State Sensors and Actuators. Digest of Technical Papers*, 1991, pp. 966–968.

[28] I. Roland, S. Masson, O. Ducloux, O. Le Traon, and A. Bosseboeu, "GaAs 3-axis Coriolis vibrating micro rate gyro: concept and preliminary characterization," *Procedia Eng.*, vol. 5, pp. 1442–1445, 2010.

[29] Y. Chen, J. Jiao, B. Xiong, L. Che, X. Li, and Y. Wang, "A novel tuning fork gyroscope with high Q-factors working at atmospheric pressure," *Microsyst. Technol.*, vol. 11, no. 2–3, pp. 111–116, Feb. 2005.

[30] M. S. Weinberg *et al.*, "A micromachined comb-drive tuning fork gyroscope for commercial applications," in *Sensor Expo*, 1994, pp. 187–193.

[31] The Charles Stark Draper Laboratory Inc., "Draper History," 2017. [Online]. Available: http://www.draper.com/history. [Accessed: 10-Mar-2017].

[32] M. W. Putty and K. Najafi, "A Micromachined Vibrating Ring Gyroscope," in *Hilton Head Solid State Sensors, Actuators, and Microsystems Workshop*, 1994, pp. 213–220.

[33] F. Ayazi, H. H. Chen, F. Kocer, H. Guong, and K. Najafi, "A High Aspect-Ratio Polysilicon Vibrating Ring Gyroscope," in *Hilton Head*, 2000, pp. 289–292.

[34] G. He and K. Najafi, "a Single-Crystal Silicon Vibrating Ring Gyroscope," *Micro Electro Mech. Syst. MEMS 2002 IEEE*, no. 734, pp. 718–721, 2002.

[35] S. Nitzan *et al.*, "Epitaxially-encapsulated polysilicon disk resonator gyroscope," in *2013 IEEE 26th International Conference on Micro Electro Mechanical Systems (MEMS)*, 2013, pp. 625–628.

[36] D. Senkal *et al.*, "100K Q-factor toroidal ring gyroscope implemented in wafer-level epitaxial silicon encapsulation process," in *2014 IEEE 27th International Conference on Micro Electro Mechanical Systems (MEMS)*, 2014, pp. 24–27.

[37] "Smithsonian National Air and Space Museum." [Online]. Available: https://airandspace.si.edu. [Accessed: 04-May-2017].

[38] A. A. Trusov *et al.*, "MHRG: Miniature CVG with beyond navigation grade performance and real time self-calibration," *IEEE 3rd Int. Symp. Inert. Sensors Syst. ISS 2016 - Proc.*, pp. 29–32, 2016.

[39]   D. Senkal, M. J. Ahamed, and A. M. Shkel, "Design and Modeling of Micro-glassblown Inverted-wineglass Structures," no. 1, pp. 2–5, 2014.

[40]   V. Tavassoli, B. Hamelin, and F. Ayazi, "Substrate-Decoupled 3D Micro-Shell Resonators," in *2016 IEEE SENSORS*, 2016, pp. 1–3.

[41]   M. M. Rahman, Y. Xie, C. Mastrangelo, and H. Kim, "3-D hemispherical micro glass-shell resonator with integrated electrostatic excitation and capacitive detection transducers," in *2014 IEEE 27th International Conference on Micro Electro Mechanical Systems (MEMS)*, 2014, pp. 672–675.

[42]   D. M. Rozelle, A. D. Meyer, A. A. Trusov, and D. K. Sakaida, "Milli-HRG inertial sensor assembly – a reality," in *2015 IEEE International Symposium on Inertial Sensors and Systems (ISISS) Proceedings*, 2015, pp. 1–4.

[43]   D. Senkal, A. Efimovskaya, and A. M. Shkel, "Minimal realization of dynamically balanced lumped mass WA gyroscope: dual foucault pendulum," in *2015 IEEE International Symposium on Inertial Sensors and Systems (ISISS) Proceedings*, 2015, pp. 1–2.

[44]   M. W. Putty, "A Micromachined Vibrating Ring Gyroscope," University of Michigan, 1995.

[45]   S. a. Zotov, A. a. Trusov, and A. M. Shkel, "Demonstration of a wide dynamic range angular rate sensor based on frequency modulation," in *2011 IEEE SENSORS Proceedings*, 2011, no. 3, pp. 149–152.

[46]   Gladiator Technologies, "Glossary," 2017. [Online]. Available: http://www.gladiatortechnologies.com/glossary/. [Accessed: 01-Jan-2017].

[47]   H. Gavcar, "Compensation methods for quasi-static acceleration sensitivity of mems gyroscopes," MIddle East Technical University, 2014.

[48]   Vectornav, "Gyroscope." [Online]. Available: http://www.vectornav.com/support/library/gyroscope. [Accessed: 19-Mar-2017].

[49]   J. Cho, "High-performance micromachined vibratory rate- and rate-integrating gyroscopes," University of Michigan, 2012.

[50]   W. Stockwell, "Angle Random Walk," *Crossbow*, pp. 1–4, 2003.

[51]   G. Billingsley and LIGO Scienctific Collaboration, "Advanced LIGO Test Mass Material Down-select Plan," 2004.

[52]   H. G. Wang and T. C. Williams, "Strategic inertial navigation systems - high-accuracy inertially stabilized platforms for hostile environments," *IEEE Control Syst. Mag.*, vol. 28, no. 1, pp. 65–85, Feb. 2008.

[53]   S. Askari, M. H. Asadian, K. Kakavand, and A. M. Shkel, "Vacuum sealed and getter activated MEMS Quad Mass Gyroscope demonstrating better than 1.2 million quality factor," in *2016 IEEE International Symposium on Inertial Sensors and Systems*, 2016, pp. 142–143.

[54]   E. J. Loper, D. D. Lynch, and K. M. Stevenson, "Projected Performance of Smaller Hemispherical Resonator Gyros," in *PLANS '86 - Position Location and Navigation Symposium*, 1986, pp. 61–64.

[55]   "IEEE Standard Specification Format Guide and Test Procedure for Coriolis Vibratory Gyros," *IEEE Std 1431-2004*, pp. 1–78, 2004.

[56]   J. Cho, T. Nagourney, A. Darvishian, and K. Najafi, "Ultra conformal high aspect-ratio small-gap capacitive electrode formation technology for 3D micro shell resonators," in *2017 IEEE 30th International Conference on Micro Electro Mechanical Systems (MEMS)*, 2017, pp. 1169–1172.

[57]   K. Najafi, T. Nagourney, and J. Cho, "Three dimensional microstructures and fabrication process," US9796586B2, 2017.

[58]   W. J. Startin, M. A. Beilby, and P. R. Saulson, "Mechanical quality factors of fused silica resonators," *Rev. Sci. Instrum.*, vol. 69, no. 10, pp. 3681–3689, Oct. 1998.

[59]   A. Ageev, B. C. Palmer, A. De Felice, S. D. Penn, and P. R. Saulson, "Very high quality factor measured in annealed fused silica," *Class. Quantum Gravity*, vol. 21, no. 16, pp. 3887–3892, Aug. 2004.

[60]   "Corning® HPFS® 7979, 7980, 8655 Fused Silica." Corning Inc., Canton, NY.

[61]   A. Darvishian, T. Nagourney, J. Cho, B. Shiari, and K. Najafi, "Thermoelastic Dissipation in Micromachined Birdbath Shell Resonators," *J. Microelectromechanical Syst.*, vol. 26, no. 4, pp. 758–772, Aug. 2017.

[62]   S. Askari, M. H. Asadian, K. Kakavand, and A. M. Shkel, "Near-Navigation Grade Quad Mass Gyroscope With Q-Factor Limited By Thermo-Elastic Damping," in *Solid-State Sensors, Actuators and Microsystems Conference (Hilton Head)*, 2016, pp. 254–257.

[63]   T. Nagourney, J. Cho, A. Darvishian, B. Shiari, and K. Najafi, "Micromachined high-Q fused silica bell resonator with complex profile curvature realized using 3D micro blowtorch molding," in *2015 Transducers - 2015 18th International Conference on Solid-State Sensors, Actuators and Microsystems (TRANSDUCERS)*, 2015, pp. 1311–1314.

[64]   T. Nagourney, J. Cho, A. Darvishian, B. Shiari, and K. Najafi, "Effect of metal annealing on the Q-factor of metal- coated fused silica micro shell resonators," in *2015 IEEE International Symposium on Inertial Sensors and Systems (ISISS) Proceedings*, 2015, pp. 1–5.

[65]   McGraw, "Transfer of Heat in Glass During Forming," *J. Am. Ceram. Soc.*, vol. 44, no. 7, pp. 353–363, 1961.

[66]   S. K. Pchelyakov and Y. A. Guloyan, "Heat Transfer at the Glass-Mold Interface," *Glas. Ceram.*, vol. 42, no. 9, pp. 400–403, 1985.

[67]   J. Cho, J. Yan, J. A. Gregory, H. W. Eberhart, R. L. Peterson, and K. Najafi, "3-Dimensional Blow Torch-Molding of Fused Silica Microstructures," *J. Microelectromechanical Syst.*, vol. 22, no. 6, pp. 1276–1284, Dec. 2013.

[68]   B. Shiari and K. Najafi, "Surface effect influence on the quality factor of microresonators," in *2013 Transducers & Eurosensors XXVII: The 17th International Conference on Solid-State Sensors, Actuators and Microsystems (TRANSDUCERS & EUROSENSORS XXVII)*, 2013, no. June, pp. 1715–1718.

[69]   B. Shiari, A. Darvishian, T. Nagourney, J. Cho, and K. Najafi, "A Comparison Between Experiments and FEM Predictions for Blowtorch Reflow of Fused Silica Micro-Shell Resonators," in *2015 Transducers - 2015 18th International Conference on Solid-State Sensors, Actuators and Microsystems (TRANSDUCERS)*, 2015, pp. 776–779.

[70]   B. Shiari, T. Nagourney, A. Darvishian, J. Cho, and K. Najafi, "Simulation of Blowtorch Reflow of Fused Silica Micro-Shell Resonators," *J. Microelectromechanical Syst.*, vol. 26, no. 4, pp. 782–792, Aug. 2017.

[71]   F. E. Materials, "Pb-Based Sealing Glass Pastes," 2008. [Online]. Available: http://www.ferro.com/non-cms/ems/EPM/content/docs/11-036, 11-155, 11-201, 1180A.pdf. [Accessed: 03-Mar-2017].

[72]   ASM International, "Thermal Expansion," in *Thermal Properties of Metals*, ASM International, 2002, p. 12.

[73]   A. Vafanejad and E. S. Kim, "Sub-Degree Angle Detection Using Micromachined Dome-Dhaped-Diaphragm Resonator with Wine-glass Mode Vibration," *Solid-State Sensors, Actuators, Microsystems Work. (hilt. Head)*, pp. 391–394, 2014.

[74]   C. Boyd *et al.*, "Effect of drive-axis displacement on MEMS Birdbath Resonator Gyroscope performance," in *2017 IEEE International Symposium on Inertial Sensors and Systems (INERTIAL)*, 2017, pp. 1–2.

[75]   R. L. Kubena, D. T. Chang, and R. L. Larson, "Quartz-based disk resonator gyro with ultra-thin conductive outer electrodes and method of making same," US8766745 B1, 2014.

[76]   R. W. Johnson, A. Hultqvist, and S. F. Bent, "A brief review of atomic layer deposition: from fundamentals to applications," *Mater. Today*, vol. 17, no. 5, pp. 236–246, Jun. 2014.

[77] P. Malinský, P. Slepička, V. Hnatowicz, and V. Švorčík, "Early stages of growth of gold layers sputter deposited on glass and silicon substrates," *Nanoscale Res. Lett.*, vol. 7, no. 1, p. 241, 2012.

[78] C. A. Hagedorn, S. Schlamminger, and J. H. Gundlach, "Quality Factors of Bare and Metal-Coated Quartz and Fused Silica Torsion Fibers," in *AIP Conference Proceedings*, 2006, vol. 873, pp. 189–193.

[79] J. Fan and C. Seng, "Low Temperature Wafer-Level Metal Thermo-Compression Bonding Technology for 3D Integration," in *Metallurgy - Advances in Materials and Processes*, vol. 52, no. 2, InTech, 2012, pp. 302–311.

[80] D. Miller, C. Herrmann, H. Maier, S. George, C. Stoldt, and K. Gall, "Intrinsic stress development and microstructure evolution of Au/Cr/Si multilayer thin films subject to annealing," *Scr. Mater.*, vol. 52, no. 9, pp. 873–879, May 2005.

[81] P. H. Holloway, "Gold/chromium metallizations for electronic devices," *Gold Bull.*, vol. 12, no. 3, pp. 99–106, Sep. 1979.

[82] M. George, W. Glaunsinger, T. Thundat, and S. Lindsay, "Electrical, spectroscopic, and morphological investigation of chromium diffusion through gold films," *Thin Solid Films*, vol. 189, no. 1, pp. 59–72, Aug. 1990.

[83] J. F. Moulder, W. F. Stickle, P. E. Sobol, and K. D. Bomben, *Handbook of X-ray Photoelectron Spectroscopy*. Eden Prairie, MN: Perkin-Elmer Corporation, 1993.

[84] R. E. Hampy, F. G. Yost, and F. P. Ganyard, "Interfacial behavior of Cr–Au films in the 423–573-K temperature range," *J. Vac. Sci. Technol.*, vol. 16, no. 1, pp. 25–30, 1979.

[85] G. Z. Voyiadjis, D. Faghihi, and Y. Zhang, "A theory for grain boundaries with strain-gradient plasticity," *Int. J. Solids Struct.*, vol. 51, no. 10, pp. 1872–1889, 2014.

[86] M. A. Abdelmoneum, M. M. Demirci, Yu-Wei Lin, and C. T.-C. Nguyen, "Location-dependent frequency tuning of vibrating micromechanical resonators via laser trimming," in *Proceedings of the 2004 IEEE International Frequency Control Symposium and Exposition, 2004.*, 2004, vol. 0, no. c, pp. 272–279.

[87] U. Schmid, "The impact of thermal annealing and adhesion film thickness on the resistivity and the agglomeration behavior of titanium/platinum thin films," *J. Appl. Phys.*, vol. 103, no. 5, 2008.

[88] U. Schmid and H. Seidel, "Influence of thermal annealing on the resistivity of titanium/platinum thin films," *J. Vac. Sci. Technol. A Vacuum, Surfaces, Film.*, vol. 24, no. 6, pp. 2139–2146, 2006.

[89] U. Schmid and H. Seidel, "Effect of high temperature annealing on the electrical performance of titanium/platinum thin films," *Thin Solid Films*, vol. 516, no. 6, pp. 898–906, 2008.

[90] V. Merie, M. Pustan, G. Negrea, and C. Bîrleanu, "Research on titanium nitride thin films deposited by reactive magnetron sputtering for MEMS applications," *Appl. Surf. Sci.*, vol. 358, pp. 525–532, Dec. 2015.

[91] F. Solis-Pomar *et al.*, "Preparation and characterization of nanostructured titanium nitride thin films at room temperature," *Ceram. Int.*, vol. 42, no. 6, pp. 7571–7575, May 2016.

[92] R. H. Dauskardt, M. Lane, Q. Ma, and N. Krishna, "Adhesion and debonding of multi-layer thin film structures," *Eng. Fract. Mech.*, vol. 61, no. 1, pp. 141–162, Aug. 1998.

[93] N. K. Ponon *et al.*, "Effect of deposition conditions and post deposition anneal on reactively sputtered titanium nitride thin films," *Thin Solid Films*, vol. 578, pp. 31–37, Mar. 2015.

[94] P. Shao, L. D. Sorenson, X. Gao, and F. Ayazi, "Wineglass-On-a-Chip," in *Solid-State Sensors, Actuators and Microsystems Conference (Hilton Head)*, 2012, vol. 7, pp. 275–278.

[95] Y. Jin, Y.-G. Kim, J. H. Kim, and D. K. Kim, "Electrical Properties of DC Sputtered Titanium Nitride Films with Different Processing Conditions and Substrates," *Journal of the Korean Ceramic Society*, vol. 42, no. 7. pp. 455–460, 2005.

[96] K. Khojier, H. Savaloni, E. Shokrai, Z. Dehghani, and N. Z. Dehnavi, "Influence of argon gas flow on mechanical and electrical properties of sputtered titanium nitride thin films," pp. 2–7, 2013.

[97] R. X. Wang *et al.*, "Influence of annealing temperature and environment on the properties of indium tin oxide thin films," *J. Phys. D. Appl. Phys.*, vol. 38, no. 12, pp. 2000–2005, Jun. 2005.

[98] M. Higuchi, S. Uekusa, R. Nakano, and K. Yokogawa, "Postdeposition Annealing Influence on Sputtered Indium Tin Oxide Film Characteristics," *Jpn. J. Appl. Phys.*, vol. 33, no. Part 1, No.1A, pp. 302–306, Jan. 1994.

[99] Z. Hao and B. Liao, "An analytical study on interfacial dissipation in piezoelectric rectangular block resonators with in-plane longitudinal-mode vibrations," *Sensors Actuators, A Phys.*, vol. 163, no. 1, pp. 401–409, 2010.

[100] A. Frangi, M. Cremonesi, A. Jaakkola, and T. Pensala, "Analysis of anchor and interface losses in piezoelectric MEMS resonators," *Sensors Actuators A Phys.*, vol. 190, pp. 127–135, Feb. 2013.

[101] P. Shao, V. Tavassoli, C. Liu, L. Sorenson, and F. Ayazi, "Electrical characterization of ALD-coated silicon dioxide micro-hemispherical shell resonators," in *2014 IEEE 27th International Conference on Micro Electro Mechanical Systems (MEMS)*, 2014, pp. 612–615.

[102] V. Kempe, *Inertial MEMS: Principles and Practice*. Cambridge University Press, 2011.

[103] H. Campanella, *Acoustic Wave and Electromechanical Resonators: Concept to Key Applications*. Artech House, 2010.

[104] R. Nave, "Mean Free Path," *HyperPhysics*. [Online]. Available: http://hyperphysics.phy-astr.gsu.edu/hbase/Kinetic/menfre.html. [Accessed: 01-Jan-2017].

[105] C. Zener, "Internal Friction in Solids. I. Theory of Internal Friction in Reeds," *Phys. Rev.*, vol. 52, no. 3, pp. 230–235, Aug. 1937.

[106] C. Zener, "Internal friction in solids II. General theory of thermoelastic internal friction," *Phys. Rev.*, vol. 53, no. 1, pp. 90–99, 1938.

[107] K. Danzmann, "Laser interferometric gravitational wave detectors," in *13th Int. Conf. on General Relativity and Gravitation*, 1992, pp. 3–20.

[108] R. Lifshitz and M. L. Roukes, "Thermoelastic damping in micro- and nanomechanical systems," *Phys. Rev. B*, vol. 61, no. 8, pp. 5600–5609, Feb. 2000.

[109] A. Darvishian, B. Shiari, J. Cho, T. Nagourney, and K. Najafi, "Investigation of Thermoelastic Loss Mechanism in Shell Resonators," in *Volume 10: Micro- and Nano-Systems Engineering and Packaging*, 2014, p. V010T13A062.

[110] S. D. Penn *et al.*, "Frequency and surface dependence of the mechanical loss in fused silica," *Phys. Lett. A*, vol. 352, no. 1–2, pp. 3–6, Mar. 2006.

[111] P. Willems, C. Lamb, A. Heptonstall, and J. Hough, "Search for stress dependence in the internal friction of fused silica," *Phys. Lett. A*, vol. 319, no. 1–2, pp. 8–12, 2003.

[112] K. Numata *et al.*, "Systematic measurement of the intrinsic losses in various kinds of bulk fused silica," *Phys. Lett. A*, vol. 327, no. 4, pp. 263–271, Jul. 2004.

[113] K. Numata *et al.*, "Measurement of the intrinsic mechanical loss of low-loss samples using a nodal support," *Phys. Lett. A*, vol. 276, no. 1–4, pp. 37–46, 2000.

[114] A. M. Gretarsson and G. M. Harry, "Dissipation of mechanical energy in fused silica fibers," *Rev. Sci. Instrum.*, vol. 70, no. 10, pp. 4081–4087, Oct. 1999.

[115] S. D. Penn *et al.*, "High quality factor measured in fused silica," *Rev. Sci. Instrum.*, vol. 72, no. 9, pp. 3670–3673, 2001.

[116] S. Penn, "Update on Mechanical Loss Studies in Fused Silica," 2006.

[117] K. Y. Yasumura *et al.*, "Quality factors in micron- and submicron-thick cantilevers," *J. Microelectromechanical Syst.*, vol. 9, no. 1, pp. 117–125, 2000.

[118] Jinling Yang, T. Ono, and M. Esashi, "Energy dissipation in submicrometer thick single-crystal silicon cantilevers," *J. Microelectromechanical Syst.*, vol. 11, no. 6, pp. 775–783, Dec. 2002.

[119] Z. Hao, A. Erbil, and F. Ayazi, "An analytical model for support loss in micromachined beam resonators with in-plane flexural vibrations," *Sensors Actuators A Phys.*, vol. 109, no. 1–2, pp. 156–164, Dec. 2003.

[120] C. Q. Ru, "Size effect of dissipative surface stress on quality factor of microbeams," *Appl. Phys. Lett.*, vol. 94, no. 5, p. 51905, Feb. 2009.

[121] V. B. Braginsky, V. P. Mitrofanov, and V. I. Panov, *Systems with Small Dissipation*. 1985.

[122] V. P. Mitrofanov and K. V. Tokmakov, "Effect of heating on dissipation of mechanical energy in fused silica fibers," *Phys. Lett. A*, vol. 308, no. 2–3, pp. 212–218, Feb. 2003.

[123] T. Ono and M. Esashi, "Effect of ion attachment on mechanical dissipation of a resonator," *Appl. Phys. Lett.*, vol. 87, no. 4, pp. 2003–2006, 2005.

[124] A. Picard, P. Barat, M. Borys, M. Firlus, and S. Mizushima, "State-of-the-art mass determination of 28 Si spheres for the Avogadro project," *Metrologia*, vol. 48, no. 2, pp. S112–S119, Apr. 2011.

[125] R. H. Doremus, "Diffusion of water in silica glass," *J. Mater. Res.*, vol. 10, no. 9, pp. 2379–2389, Sep. 1995.

[126] L. Sorenson, P. Shao, and F. Ayazi, "Bulk and Surface Thermoelastic Dissipation in Micro-Hemispherical Shell Resonators," *J. Microelectromechanical Syst.*, vol. 24, no. 2, pp. 486–502, Apr. 2015.

[127] S. L. Warring, D. A. Beattie, and A. J. McQuillan, "Surficial Siloxane-to-Silanol Interconversion during Room-Temperature Hydration/Dehydration of Amorphous Silica Films Observed by ATR-IR and TIR-Raman Spectroscopy," *Langmuir*, vol. 32, no. 6, pp. 1568–1576, 2016.

[128] E. Izmailov, M. Kolesnik, A. Osipov, and A. Akimov, "Hemispherical Resonator Gyro Technology. Problems and Possible Ways of their Solutions," in *RTO SCI Conference on "ntegrated Navigation Systems*, 1999, pp. 6–1–6–9.

[129] X. Liu, J. F. Vignola, H. J. Simpson, B. R. Lemon, B. H. Houston, and D. M. Photiadis, "A loss mechanism study of a very high Q silicon micromechanical oscillator," *J. Appl. Phys.*, vol. 97, no. 2, 2005.

[130] A. M. Gretarsson, "Effect of optical coating and surface treatments on mechanical loss in fused silica," *AIP Conf. Proc.*, vol. 523, no. 2000, pp. 306–312, 2000.

[131] M. J. Ahamed, D. Senkal, and A. M. Shkel, "Effect of annealing on mechanical quality factor of fused quartz hemispherical resonator," *2014 Int. Symp. Inert. Sensors Syst.*, no. c, pp. 1–4, 2014.